Solar surface flows during active region emergence

Dissertation

zur Erlangung des mathematisch-naturwissenschaftlichen Doktorgrades

"Doctor rerum naturalium"

der Georg-August-Universität Göttingen

im Promotionsstudiengang Physik

der Georg-August University School of Science (GAUSS)

vorgelegt von

Nils Gottschling

aus Bochum, Deutschland

Göttingen, 2021

Betreuungsausschuss

Prof. Dr. Laurent Gizon
Max-Planck-Institut für Sonnensystemforschung, Göttingen, Deutschland und
Institut für Astrophysik, Georg-August-Universität Göttingen, Göttingen, Deutschland

Dr. Aaron Birch
Max-Planck-Institut für Sonnensystemforschung, Göttingen, Deutschland

Prof Dr. Andreas Tilgner
Institut für Geophysik, Georg-August-Universität Göttingen, Göttingen, Deutschland

Mitglieder der Prüfungskommision

Referent: Prof. Dr. Laurent Gizon
Max-Planck-Institut für Sonnensystemforschung, Göttingen, Deutschland und
Institut für Astrophysik, Georg-August-Universität Göttingen, Göttingen, Deutschland

Korreferent: Prof Dr. Andreas Tilgner
Institut für Geophysik, Georg-August-Universität Göttingen, Göttingen, Deutschland

Weitere Mitglieder der Prüfungskommission:

Prof. Dr. Ulrich Christensen
Max-Planck-Institut für Sonnensystemforschung, Göttingen, Deutschland

Prof. Dr. Wolfram Kollatschny
Institut für Astrophysik, Georg-August-Universität Göttingen, Göttingen, Deutschland

Prof. Dr. Hardi Peter
Max-Planck-Institut für Sonnensystemforschung, Göttingen, Deutschland

PD Dr. Olga Shishkina
Max-Planck-Institut für Dynamik und Selbstorganisation, Göttingen, Deutschland

Tag der mündlichen Prüfung: 08.11.2021

Bibliografische Information der Deutschen Nationalbibliothek

Die Deutsche Nationalbibliothek verzeichnet diese Publikation in der Deutschen Nationalbibliografie; detaillierte bibliografische Daten sind im Internet über `http://dnb.d-nb.de` abrufbar.

Printed in Germany

Contents

3 Testing solar surface flux transport models in the first days after active region emergence

4 Discussion

5 Conclusion and Outlook

Bibliography

A Magnetic flux as a function of central meridian distance in SDO data

Scientific contributions

Acknowledgements

List of Figures

Summary

The aim of this thesis is to improve our understanding of the emergence of magnetic flux in the form of active regions (ARs) to the solar surface. Active regions are concentrations of strong magnetic field at the surface of the Sun. Their emergence is not yet fully understood. To help better constrain the underlying principles of flux emergence, and thus better understand the role of ARs in the conversion of toroidal to poloidal field in the context of the solar dynamo, I analyze the surface flows associated with active regions during their emergence phase and assess the impact of these flows on the magnetic flux transport in the first days after emergence.

For the study of the surface flows, I use ten years of data from the Helioseismic and Magnetic Imager (HMI) onboard the Solar Dynamics Observatory (SDO) together with a sample of 182 emerging active regions (EARs). The flows are derived using the method of local correlation tracking (LCT), which in this case measures the motions of the solar convective granulation pattern on the surface of the Sun in continuum intensity images.

In the first part of this thesis, I validate the LCT data by tests with synthetic flow features as well as by cross-correlating them with flows inferred from direct Doppler imaging. I analyze the average temporal evolution of the flows associated with the sample of 182 EARs, relative to the time of emergence and in subsamples with respect to the unsigned magnetic flux and latitude. I find that one day prior to emergence, converging flows towards the AR location form, irrespective of the eventual total unsigned flux of the AR. After emergence, inflows around the ARs form. The time between emergence and the time at which these inflows form increases with the AR magnetic flux, from one to four days after emergence in the sample used here. These inflows are mainly in the latitudinal direction, have velocities on the order of $50\,\mathrm{m\,s^{-1}}$, and extend to about $8°$ from the AR center.

On the solar surface, magnetic flux is transported by the various flows. In the second part of this thesis, I study the evolution of the magnetic field of 17 active regions in a local surface flux transport model (SFTM). The simulation considers diffusion as well as advection by an imposed flow field. For the latter, I use the flow measurements from LCT, as well as parameterized flow fields that model the observed inflows around ARs. The simulations show that the supergranular motions buffet the magnetic field in a way that is consistent with the evolution of the observed field. I find that the SFTM is applicable once the bulk of the AR flux has emerged. The parameterized flows increase the flux loss of the AR due to cancellation, which is balanced by a decrease due to advection.

The twist of magnetic field lines is a property of ARs which in some models is important for forming coherent flux tubes. The vortical flows around EARs can be used as a tracer of twisting motions of AR polarities. Analyzing the vortical flows around a sample of 20 EARs, I find an average opposite sign of vorticity between the two polarities.

Zusammenfassung

Das Ziel dieser Arbeit ist es, zu einem besseren Verständnis davon beizutragen, wie aktive Regionen (AR) entstehen. Aktive Regionen sind Konzentrationen von Magnetfeld auf der Sonnenoberfläche. Es ist noch nicht abschließend verstanden, wie AR aus dem Sonneninneren an die Oberfläche aufsteigen. Um die zugrundeliegenden Eigenschaften dieses Prozesses einzugrenzen, und damit verbunden die Rolle von aktiven Regionen bei der Umwandlung von toroidalem in poloidales Magnetfeld im Kontext des solaren Dynamos besser zu verstehen, analysiere ich die Oberflächenströmungen auf der Sonne, die mit den aktiven Regionen in deren Entstehungsphase zusammenhängen. Ich untersuche außerdem den Einfluss dieser Strömungen auf den Transport des Magnetfeldes innerhalb der ersten Tage nach Entstehung der AR.

Zur Untersuchung der Oberflächenströmungen verwende ich Beobachtungsdaten des Helioseismic and Magnetic Imager (HMI) an Bord des Solar Dynamics Observatory (SDO) aus 10 Jahren zusammen mit 182 enstehenden aktiven Regionen (EAR). Die Strömungen wurden mithilfe von lokalem Korrelationstracking (local correlation tracking, LCT) bestimmt, einer Methode, mit der die Bewegung des Sonnengranulationsmusters auf der Sonnenoberfläche in Kontinuumsbildern gemessen werden kann.

Im ersten Teil dieser Dissertation validiere ich die LCT Daten mithilfe von synthetischen Strömungsdaten sowie einer Kreuzkorrelation zu Strömungskarten von Doppleraufnahmen. Ich analysiere die mittlere zeitliche Entwicklung der Strömungen im Zusammenhang mit den 182 entstehenden aktiven Regionen, relativ zu der Zeit der Entstehung der AR sowie in Untergruppen nach magnetischer Flussstärke und nach Latitude. Es zeigt sich, dass sich einen Tag vor Entstehung der AR konvergierende Ströme in Richtung der AR bilden, unabhängig vom späteren maximalen magnetischen Fluss der AR. Nach der Entstehung der AR bilden sich Einströmungen um die AR. Die Zeit zwischen Entstehung der AR und dem Einsetzen der Einströmungen verlängert sich umso mehr, je stärker der magnetische Fluss der AR ist. Dieser Zeitraum reicht von einem auf bis zu vier Tage nach Entstehung der AR, in der hier betrachteten Auswahl von AR. Die Einströmungen sind hauptsächlich in der latitudinalen Richtung ausgeprägt, haben Geschwindigkeiten in der Größenordnung von $50\,\mathrm{m\,s^{-1}}$ und eine Ausdehnung von etwa $8°$ vom Zentrum der AR.

Magnetischer Fluss wird auf der Sonnenoberfläche von verschiedenen Oberflächenströmungen transportiert. Im zweiten Teil dieser Dissertation betrachte ich, wie sich das Magnetfeld einer Auswahl von 17 aktiven Regionen in einem lokalen Oberflächenflusstransportmodell (local surface flux transport model, SFTM) entwickelt. Die Simulation beinhaltet Diffusion sowie Advektion durch ein äußeres Strömungsfeld. Für die Advektion werden die beobachteten LCT-Oberflächenströmungsdaten verwendet, sowie parametrisierte Strömungen, welche die beobachteten Einströmungen um AR modellieren. Die Simulationen zeigen, dass die supergranularen Strömungen das Magnetfeld auf einer

11

Art und Weise verschieben, die konsistent mit der beobachteten Entwicklung des Magnetfeldes ist. Das Modell kann angewendet werden, sobald die AR einen Großteil ihres maximalen magnetischen Flusses erreicht hat. Die parametrisierten Strömungen verstärken den Verlust von magnetischem Fluss in der AR durch Auslöschung von positivem und negativem Feld, was jedoch durch eine Verringerung des Verlustes von magnetischem Fluss durch Advektion ausgeglichen wird.

Die Verwindung von magnetischen Feldlinien ist eine Eigenschaft von AR, die in einigen Modellen für die Entstehung zusammenhängender Flussröhren notwendig ist. Die Wirbelströmungen um EAR können verwendet werden, um verwindende Bewegungen der AR-Polaritäten zu bestimmen. In meiner Analyse von Wirbelströmungen um eine Auswahl von 20 EAR beobachte ich im Mittel eine gegensätzliche Richtung der Wirbelstärke zwischen den AR-Polaritäten.

1 Introduction

1.1 Solar magnetism

The Sun is our closest star. Solar research therefore serves both to help understand the Sun's (variable) impact on Earth, as well as to provide a detailed context for the studies of other stars. While we know through observations that the Sun has a magnetic field, we do not know the details of how magnetic fields are maintained in the Sun or in other stars.

The magnetic activity of the Sun covers a broad range of temporal and spatial scales. On one end, this includes the recently discovered so-called campfires, which span several hundreds of kilometers and last for only tens of seconds (Berghmans et al. 2021). Active region complexes can cover large parts of the solar disk and last for several months. On the other end, the activity level of the Sun as a whole shows long-term variations over the course of centuries.

1.1.1 Sunspots and active regions

Sunspots are dark features on the solar disk in white light images. They have been observed with the naked eye for millennia (e.g. Vaquero and Vázquez 2009), drawings of sunspots go back to the 12th century (e.g. Arlt and Vaquero 2020). The magnetic nature of sunspots was first identified by George E. Hale in 1908, by observing Zeeman splitting (Hale 1908). This presented the first evidence that the Sun possesses a magnetic field.

Sunspots consist of two components with different magnetic properties: The umbra, where the field is mostly vertical and has peak field strengths on the order of 3500 Gauss, and the penumbra, where the field is inclined to 70–80° to the vertical and has strengths on the order of 700–1000 Gauss. The strong field in a spot suppresses convection and exerts magnetic pressure. To maintain equilibrium with the surroundings, the plasma within the spot is at a lower temperature and therefore appears dark against the surrounding quiet Sun plasma. This temperature difference is about 1000–1900 K for the umbra and 250–400 K for the penumbra (see e.g. the review by Solanki 2003 and references therein).

Sunspots appear in pairs or groups, which are roughly east-west aligned (cf. upper left panel of Fig. 1.1). The leading and the trailing spots in the sense of solar rotation have opposite signs of magnetic field. During one 11-year solar cycle (see Sect. 1.1.3), the leading parts of sunspot groups in one hemisphere share the same sign of magnetic polarity. In the same cycle, the leading polarities in the other hemisphere are of opposite sign. The signs of the polarities are then switched in the following cycle. This is known as Hale's law, and is obeyed by the vast majority of sunspot groups. Also, sunspot groups show a systematic tilt angle: On average, the leading polarity is closer to the equator than
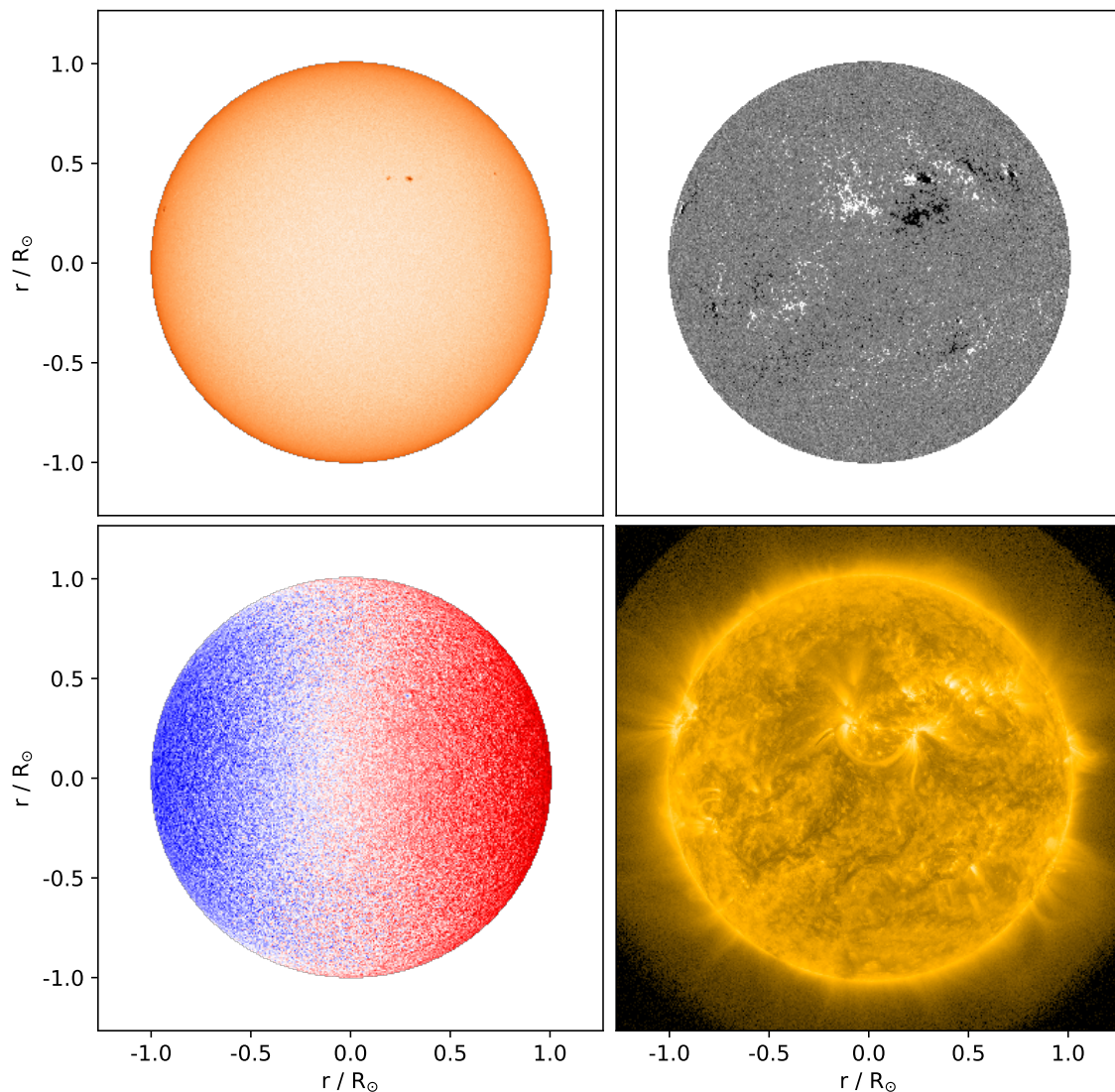
Figure 1.1: SDO full-disk images. All images are from 11 February 2010. Top left: HMI continuum intensity. Top right: HMI line-of-sight magnetic field. Bottom left: HMI Doppler velocity. Bottom right: AIA 171 nm. The data are courtesy of NASA/SDO and the AIA and HMI science teams.

the trailing polarity. This tilt angle increases with latitude, that is, high latitude sunspot groups have larger tilt angles. These relations were first found by Hale et al. (1919) and are called Joy's law, after A.H. Joy, who carried out this study.

Measurements of the magnetic field of the Sun revealed that sunspots are embedded in larger patches of magnetic field, the so-called plage regions (compare the upper left and upper right panels of Fig. 1.1). The strength of the magnetic field in plage regions reaches up to 1800 Gauss. A pair of positive and negative field polarity is called an active region (AR). The leading polarity of an active region is commonly more compact than the trailing polarity (see Bray and Loughhead 1979, Fisher et al. 2000). Hale's polarity law as well as Joy's law of tilt angles hold for active regions as well. A quantification of the tilt angle is however not straightforward: Historically, tilt angles were measured on continuum

images and therefore represented the tilt between the sunspots in an active region, whereas nowadays determining the tilt angle from magnetograms is more common (see the review by van Driel-Gesztelyi and Green 2015 and references therein). This is further complicated by the fact that the separation of the polarities in the latitudinal direction is usually small, so that errors in the position measurements of the polarities lead to large scatter. Also, active region polarities consist of multiple concentrations of flux and change their shape over time, forming for example so-called magnetic tongues.

Another property of active regions is magnetic helicity. This describes the twist, writhe, and linkage of magnetic field lines (for a review, see Pevtsov et al. 2014). Helicity is a conserved quantity in the case of ideal magnetohydrodynamics (MHD), that is, when the electric resistivity can be neglected. This is applicable to the Sun (e.g. Pevtsov et al. 2014). It has been established that magnetic structures on different scales tend to have opposite senses of helicity in the northern (negative helicity) and in the southern hemisphere (positive helicity). This is known as the hemispheric helicity rule (Seehafer 1990, see also the review by Pevtsov et al. 2014 and references therein). It is however an empirical finding, and several studies show that the tendency to obey the hemispheric helicity rule is not strong for all features. For active regions, the rule is only followed by 60–75 % (Liu et al. 2014 and review by Pevtsov et al. 2014). The evolution of twist and writhe during AR emergence is important for understanding how the helicity is generated. Pevtsov et al. (2003) measured a proxy for the twist of six emerging active regions and found that it increases during emergence, which indicates that active regions carry magnetic helicity with them through the emergence. Sangeetha et al. (2020) measured the vorticity during the emergence of one active region with correlation tracking on Doppler images from the Helioseismic and Magnetic Imager (HMI, see Sect. 1.3) to infer the rotation of the two polarities. They found that the polarities rotate in opposite directions. In general, the rotation of polarities is expected to be connected to the twist (Sturrock et al. 2015).

1.1.2 Formation of active regions

For magnetic field to appear at the solar surface in the form of sunspots and active regions, it has to be generated somewhere in the solar interior. It is the prevailing picture that sunspots and active regions are magnetic flux concentrations that emerge from the solar interior and pierce through the solar surface (the photosphere), where the observed magnetic polarities are the footpoints of the flux (Parker 1955). Figure 1.2 shows a sketch of a flux concentration before and after it pierces through the photosphere. It is however not clear yet where and how flux concentrations form. A common theory is that they result from toroidal flux which is generated, amplified, and stored near the bottom of the convection zone, at a depth of about 200 Mm, or 30 % of the solar radius. This flux then rises buoyantly through the convection zone to the surface in a so-called Ω loop, with arches of hot plasma connecting the two footpoints of the loop at the surface, as shown by observations of the solar corona (compare in Fig. 1.1 the active region in the upper right panel and the loop-like structures in the lower right panel). Other scenarios, such as formation in the bulk of the convection zone, or in the near surface shear layer, are also discussed (Nelson et al. 2013; Brandenburg 2005).

A simple description for the rising flux can be given using the thin flux tube approximation (Spruit 1981). This considers a flux tube with a cross section that is smaller than
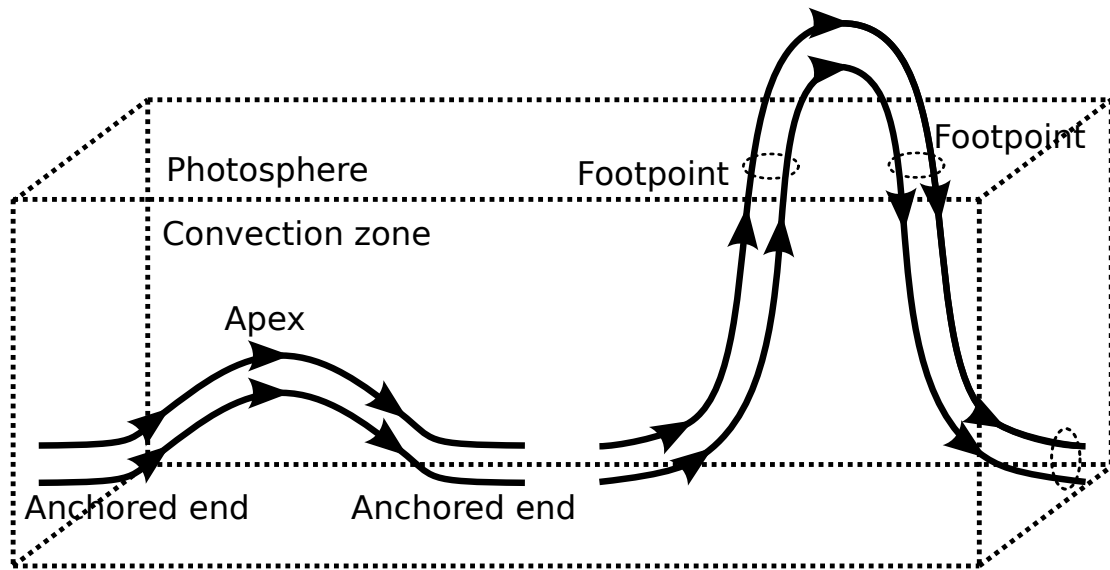
Figure 1.2: Sketch of a flux concentration before (left) and after (right) it has emerged from the convection zone through the photosphere. The arrows indicate the direction of the magnetic field. The footpoints of the emerged loop represent the magnetic polarities of the active region.

all other relevant length scales. In particular, the physical quantities such as velocity, pressure, and magnetic field strength, are averages over the cross section and assumed to vary only along the length of the flux tube. The pressure within the tube is constituted by the plasma pressure and the magnetic pressure (e.g. Fan 2009). If the flux tube and the surroundings are in thermal equilibrium, the plasma density is lower within the tube than in the surroundings. This leads to so-called magnetic buoyancy (Parker 1975), which makes the flux tube rise. Plasma flowing from the apex of the tube to the anchored ends increases the buoyancy of the tube and drives the instability.

Fan et al. (1993) found that in the thin flux tube approximation, the observed asymmetry in the compactness of the leading and the trailing polarity of ARs can result from the Coriolis force driving a retrograde flow in the flux tube. This flow creates a difference in the field strengths of the two legs of the rising Ω loop. The stronger field in the leading leg keeps it more compact and less prone to fragmentation, as observed. They also found that the leading leg has a larger inclination to the vertical than the trailing leg. However, Caligari et al. (1995) found that this is only the case for initial field strengths that are lower than expected from other considerations, for example the latitudes at which the regions emerge (see below). Rempel and Cheung (2014) also found asymmetries between the leading and the trailing polarity, by prescribing a retrograde flow in a rising flux torus. In a different approach, Chen et al. (2017) considered a 3D MHD simulation including convection instead of a uniform rise of a flux tube. This also produced a more compact leading and a more dispersed trailing polarity. They also found that the flux rises to the surface at velocities similar to that of the convection. On the other hand, Hotta and Iijima (2020) found in their MHD simulation a higher rise speed on the order of $250\,\mathrm{m\,s^{-1}}$,

without diverging flows prior to emergence. Such diverging flows had been predicted for rise speeds above $150\,\mathrm{m\,s^{-1}}$ by Birch et al. (2016), and would be inconsistent with observations (Birch et al. 2016, 2019).

Active regions emerge at latitudes below about $40°$. In the thin flux tube approximation, the field strength at the bottom of the convection zone has to be on the order of 10^5 Gauss to reproduce the observed emergence latitudes. If the field were weaker, the Coriolis force acting on the retrograde motion of the rising flux concentration (which is a result of the concentration's tendency to conserve angular momentum), would deflect the flux towards the poles by an amount that is incompatible with observations (Choudhuri 1989; Fan et al. 1993; Caligari et al. 1995).

As mentioned in Sect. 1.1.1, sunspots and ARs show a systematic tilt angle. It is not yet clear where the tilt angle comes from. One possibility is the Coriolis force acting on the rising flux (Schmidt 1968). D'Silva and Choudhuri (1993) and Caligari et al. (1995) considered models of rising thin flux tubes and found that the field strength necessary for tilt angles consistent with observations are on the order of $1 \times 10^5\,\mathrm{G}$, which is the same as that needed for the observed latitudes of emergence. The tilt angle was also reproduced in the MHD simulation by Fan and Fang (2014). However, it has been observed that at the time of emergence, the average tilt angle of ARs is consistent with zero, that is, no tilt (Kosovichev and Stenflo 2008; Schunker et al. 2020). Later on, the scatter in tilt angles is larger for weaker regions, and independent of latitude (e.g. Fisher et al. 1995; Jiang et al. 2014). The scatter in latitudinal separation (rather than the scatter in tilt angle) turns out to be flux-independent (e.g. Jiang et al. 2014; Schunker et al. 2019). Because the amount of flux of an AR correlates with its polarity separation (e.g. Wang and Zirin 1989), the scatter in latitudinal separation results in a smaller scatter of the tilt for higher-flux ARs. A possible explanation is that the scatter originates from buffeting of the flux by the convective motions (Schunker et al. 2019).

In most simulations, flux ropes need to have an initial twist in order to be able to stay buoyant throughout their rise through the convection zone and through the photosphere. Vortical motions fragment the flux tube and prevent it from reaching the surface (e.g. Schuessler 1979; Linton et al. 1996; Fan 2001; Abbett et al. 2001). However, in the recent simulation by Knizhnik et al. (2021) a flux tube emerges without the need for twist, which the authors attribute to the toroidal geometry of their rising flux tube.

The twist of ARs could be a result of accretion of poloidal flux by the flux concentration as it rises through the convection zone. Manek and Brummell (2021) showed that the existence of poloidal field in the convection zone can serve as a selection rule. In their simulation, flux concentrations that have a twist parallel to the poloidal background field in the convection zone are more likely to succeed in rising to the photosphere than flux concentrations with the opposite twist. Or, more directly, the twist could be caused by the Coriolis force inducing writhe in the rising flux, which in turn creates opposite-oriented twist in order to conserve the total helicity in a kink instability (e.g. Fan et al. 1998; Liu et al. 2014). The observation that a large fraction of regions does not follow the hemispheric helicity rule might indicate that the turbulent convective motions, having a helical preference due to solar rotation, play a role in transferring helicity to the rising flux (Longcope et al. 1998).
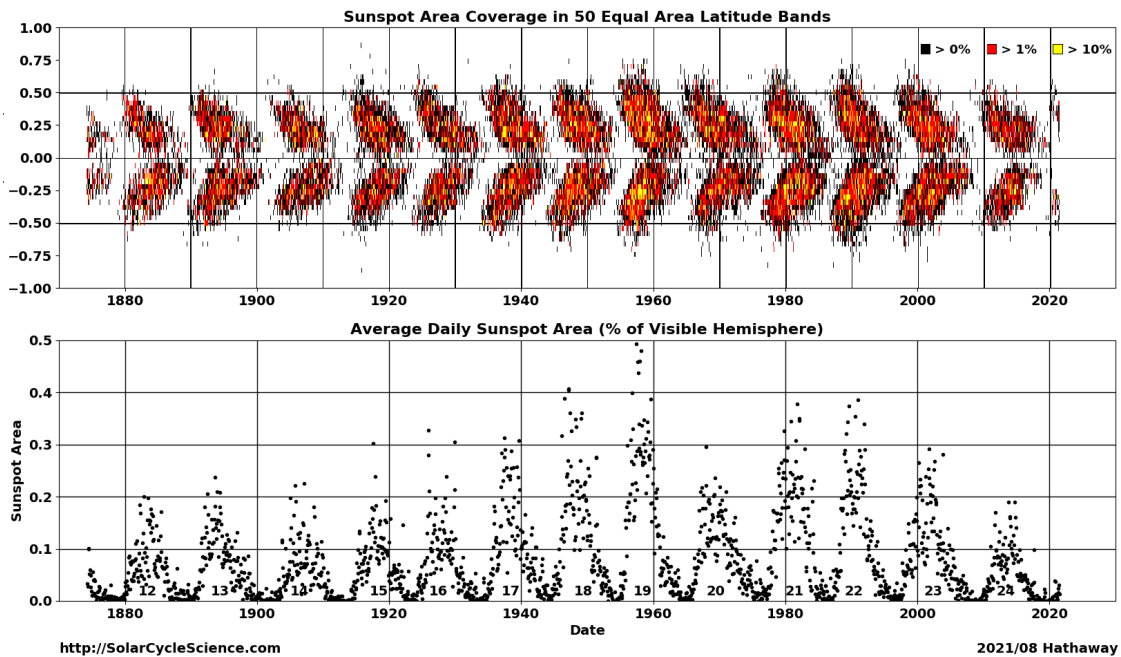
Figure 1.3: Top panel: The butterfly diagram. Sunspot area coverage as a function of latitude, plotted against time. Bottom panel: Total sunspot area coverage plotted against time. From D. H. Hathaway/Stanford, with permission.

1.1.3   Solar cycle

The solar cycle is a cyclic variation in the activity of the Sun, with a period of about 11 years. It is most readily identified by the change in the number of sunspots visible on the solar disk at the same time. The first (scientifically recorded; for more on historic oral tradition, see e.g. Vaquero and Vázquez 2009) observation of the sunspot cycle was by Schwabe (1844), who measured a period of 10 years.

Along with the increase and decrease of the number of sunspots over the solar cycle, it was noticed that the mean latitude at which the spots appear varies as well: At the beginning of one cycle, they tend to lie at about 40° away from the equator. As the cycle progresses, they appear closer and closer to the equator. This is known as Spörers law (e.g. Stix 2002). The corresponding plot of the sunspot coverage against latitude over time is the now-famous butterfly diagram (see top panel of Fig. 1.3).

The occurrence of other solar activity phenomena, such as flares or coronal mass ejections, varies alongside with that of the spots. These are the result of magnetic reconnection processes, and have a strong impact on what is known as space weather, that is, the Sun's impact on the solar system and the bodies therein (see e.g. the reviews by van Driel-Gesztelyi and Green 2015 and Temmer 2021). This has important implications for Earth (as well as air and space travel) because of the interaction with Earth's magnetic field.

The activity level of each cycle, measured for example as the sunspot coverage of the solar disk on each day, varies from cycle to cycle (see bottom panel of Fig. 1.3). Long quiescent phases have been recorded, most prominently the Maunder minimum between

1645 and 1715 (e.g. Eddy 1976). The cycles are counted successively from 1755 onward. The current cycle, cycle 25, has recently begun (in December 2019)[1].

Because of the variation in cycle strengths, efforts have been made to find underlying patterns and to predict the strength (that is, the level of activity) of subsequent cycles. The best predictor for the strength of one cycle is the polar field at the end of the previous one, that is, in the activity minimum (e.g. Cameron and Schüssler 2012; Yeates 2020 and references therein). This is indicative of a surface flux transport dynamo, where the magnetic field at the solar surface is the manifestation of a toroidal field in the solar interior. This field cancels with the poloidal field of the previous cycle and builds builds up the poloidal field of the current cycle, due to transport towards the equator and the poles, for the leading and trailing polarities, respectively (see e.g. the review by Charbonneau 2020 and references therein). As such, predicting the polar field at the end of one cycle from the active region emergences during that cycle is a promising way to extend the advance in predicting the next cycle, and the focus of a lot of research (Cameron et al. 2016; Iijima et al. 2017; Upton and Hathaway 2018). For an extensive recent review on different approaches to solar cycle prediction, see Petrovay (2020).

1.1.4 Solar dynamo models

As mentioned above, a dynamo process must be acting in the Sun in order to maintain a magnetic field that produces the observed magnetic activity. The literature on models of the solar dynamo is extensive. Here, only the basic concepts in connection with active region emergence and the relevant flows are outlined. For in-depth textbooks and reviews, the reader is referred to Ossendrijver (2003), Miesch (2012), Charbonneau (2013), Rincon (2019), and the recent review by Charbonneau (2020). As a basic concept, poloidal magnetic field in the solar interior is transformed into toroidal field by winding up due to the differential rotation. This is known as the Ω-effect. The toroidal field rises to the surface (seen as active regions, cf. the discussion on flux emergence in Sect. 1.1.2). To generate poloidal field from the toroidal field (and thus close the dynamo loop), several scenarios are possible. In the scenario of a flux transport dynamo, the convective motions diffuse the surface field, and the meridional flow advects the field towards the poles, where it cancels with the existing poloidal field, and subsequently builds up poloidal field of opposite polarity. In the solar interior, the return flow of the meridional flow advects the toroidal field towards lower latitudes, which is mirrored by the decreasing emergence latitude of active regions over the solar cycle (Wang et al. 1991; Choudhuri et al. 1995). The flows that act on the magnetic field at the surface play an important role in the solar dynamo, as they directly influence the amount of flux that reaches the polar regions.

Another possibility is the so-called $\alpha\Omega$ dynamo, where the accumulation of small-scale twists to the magnetic field (due to the Coriolis force; this is called the α-effect) creates a net poloidal field (Parker 1955). This results in a dynamo wave which moves from low to high latitudes. In this scenario, the active regions are the byproduct of a dynamo wave, rather than a crucial agent in the buildup of the next cycle's field. Further scenarios have been discussed in the literature, such as the $\alpha^2\Omega$ dynamo.

---

[1] `https://www.weather.gov/news/201509-solar-cycle`
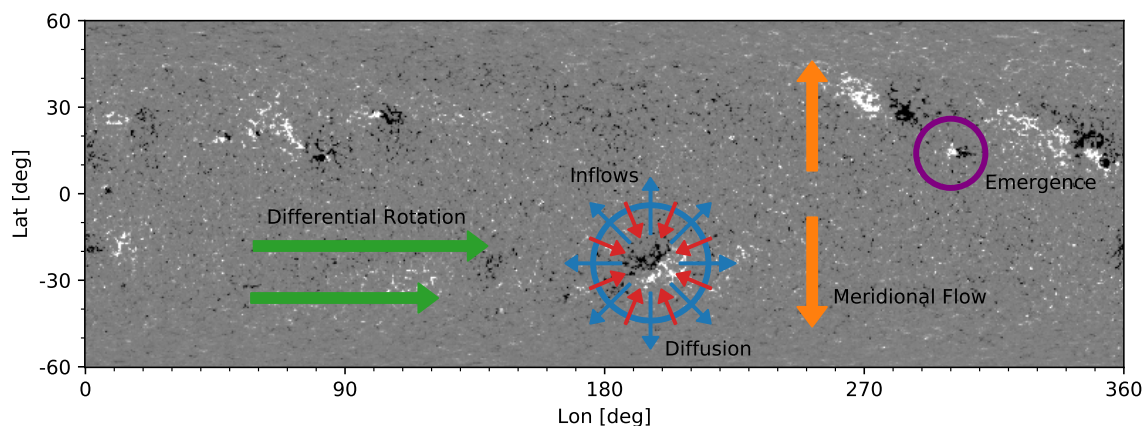
Figure 1.4: Sketch of how solar surface flows act on the magnetic field. The map shows a synoptic magnetogram from HMI line-of-sight data of Carrington rotation 2100. White (black) indicates positive (negative) magnetic field. The color scale saturates at ±50 Gauss. The purple (blue) circle indicates an emerging (evolved) active region. Magnetic field is transported by the differential rotation (green arrows), by the meridional flow (orange arrows), by diffusion of the magnetic field (blue arrows), and the inflows around active regions (red arrows). The data are courtesy of NASA/SDO and the HMI science team.

1.2   Solar surface flows

Over the years, a variety of flows has been identified both on the surface of the Sun as well as in its interior. All of these have distinct impacts on magnetic flux and on the Sun as a whole. In this section, I focus on some of the main flows that stand in close relation to active regions and their flux transport on the solar surface. Figure 1.4 shows a sketch of the main effects in the context of the evolution of AR magnetic flux.

Differential rotation: While the radiative zone rotates as a solid body, the convection zone exhibits differential rotation. On the solar surface, the rotation is fastest at the equator, with a rotation period of about 25 days, and increasingly slower towards the poles. At a latitude of 60°, the rotation period is about 31 days. Richard Carrington coined a mean rotation period of 27.2753 days, on which a list of subsequent solar rotations, the so-called Carrington rotations, is based. Within a Carrington rotation, the Carrington longitude assigned to the central meridian of the Sun starts at 360° and decreases to 0° over the course of 27.2753 days, which is when the next Carrington rotation begins.

Figure 1.5 shows a meridional cut of the differential rotation profile (left) and the radial rotation profiles at different latitudes (right). The latter shows that at the shear layer between the radiation zone and the convection zone, the rotation turns from a solid-body rotation to differential rotation. This is the so-called tachocline. Between $0.95\,R_\odot$ and the surface lies the so-called near-surface shear layer, where the rotation rate changes rapidly with height. In the context of the solar dynamo, differential rotation provides the shear that winds up the poloidal magnetic field in the solar interior to a toroidal field. The cause of the differential rotation is thought to be the turbulent convective motions acting on the angular momentum. Precise modelling is difficult however, because of the different length scales involved (Miesch 2005; Kitchatinov 2013).
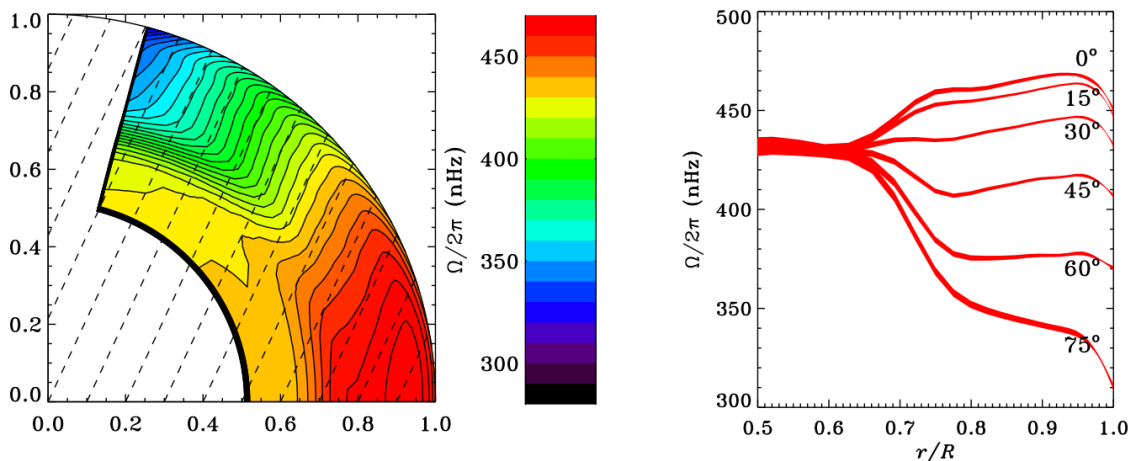
Figure 1.5: The observed solar differential rotation. Left: Meridional cut through the convection zone (the y-axis is aligned with the solar rotation axis). Dotted lines are at 25° to the rotation axis. Right: Radial cuts at different latitudes. From Howe (2009), with permission[2].

Meridional flow: The first tentative observation of the meridional flow was by Duvall (1979), based on measurements of Doppler line shifts. It was later confirmed by other studies (Labonte and Howard 1982; Komm et al. 1993), the latter using tracking of magnetic elements. The meridional flow acts as a 'conveyor belt' flow, with a bulk plasma motion towards the poles at the surface, and towards the equator in the solar interior. At the surface, the meridional flow has a velocity of approximately $15\,\mathrm{m\,s^{-1}}$ (Duvall 1979; Komm et al. 1993; Charbonneau 2013; Liang et al. 2018). Because of the small velocities, identification of the structure of the meridional flow in the solar interior is difficult: Models suggest both single- and double-cell structures (Featherstone and Miesch 2015; Pipin 2018). Recently, Gizon et al. (2020) applied time-distance helioseismology to observations of two solar cycles and inferred a single cell structure. In such a single-cell structure, from mass conservation arguments, the return flow should have a flow velocity of about $2\,\mathrm{m\,s^{-1}}$ at the bottom of the convection zone (Giles 2000). Figure 1.6 shows a sketch of a single-cell meridional flow. The meridional flow is thought to be an important agent in the solar dynamo in the context of surface flux transport dynamo models, as outlined in the previous section. It is a result of the balance of the effects of the centrifugal force on the differential rotation and a temperature difference between polar and equatorial regions (Kitchatinov 2013).

Convective motions: Outside of sunspots, the solar surface is covered by a granular pattern, first observed by Herschel (1801). Unsöld (1930) was the first to identify this so-called granulation as the small-scale structure of the upper end of the turbulent convective motion in the convection zone. The brighter granules are the locations where the hot upflowing plasma cools via radiation. The cooled plasma flows back down in the darker intergranular lanes that separate the granules. Typical sizes of granules are in the range of 1–2 Mm (see e.g. the review by Nordlund et al. 2009). The power spectrum of convective

---
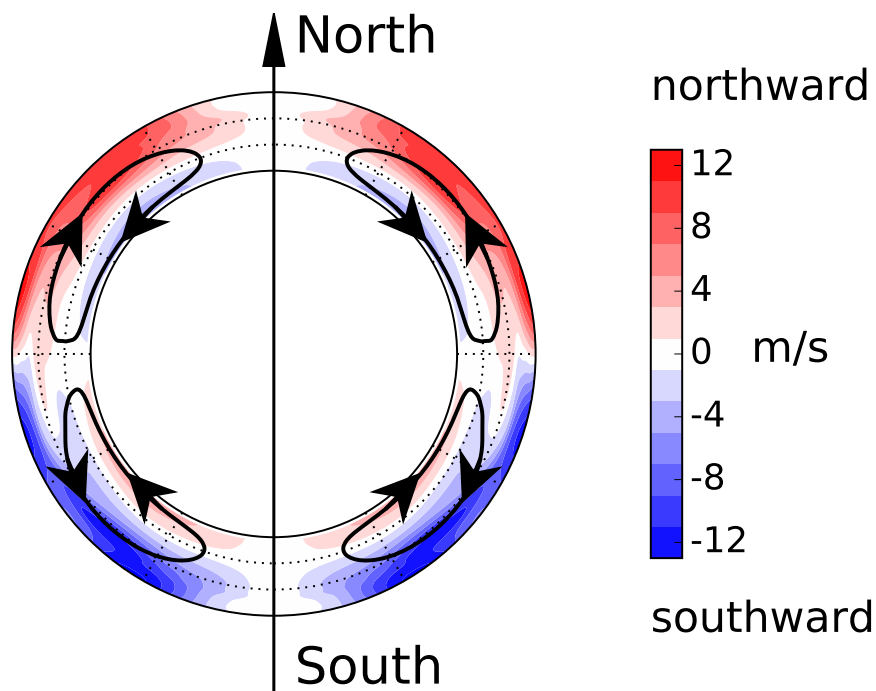
Figure 1.6: Sketch of the meridional flow in the convection zone of the Sun, with a single-cell structure. The inversion results are from Gizon et al. (2020). Image courtesy of Zhi-Chao Liang, with permission.

motions has its highest peak at about $l = 3500$, which corresponds to 1.2 Mm (Hathaway et al. 2015). The lifetime of granules follows an exponential distribution, with typical values between 1 and 5 min and a mean of about 6 min (Hirzberger et al. 1999). Horizontal flow velocities are typically on the order of $2\,\mathrm{km\,s^{-1}}$ (see the review by Nordlund et al. 2009 and recently Oba et al. 2020).

In addition to the peak at $l = 3500$, the power spectrum of the convective motions on the Sun shows a second peak at an angular degree of $l = 120$, which corresponds to approximately 30 Mm (e.g. Hathaway et al. 2000; Hirzberger et al. 2008; Hathaway et al. 2015; see also the review by Rieutord and Rincon 2010). This distinct convective scale has been coined supergranulation by Leighton et al. (1962). The first identification of supergranules is attributed to Hart (1956), who studied direct Doppler images away from disk center (cf. lower left panel of Fig. 1.1). At disk center, correlation tracking methods can be used to identify supergranulation (see Rast 2003 for more references on supergranulation detections). Their lifetimes are on the order of 1 day. Their horizontal velocities are typically on the order of 300–$500\,\mathrm{m\,s^{-1}}$ (see e.g. Wang and Zirin 1989 and references therein), directed radially outward from the center of the supergranule. The vertical velocity of supergranulation at the surface is more difficult to measure because of its low amplitude; estimates of the rms velocity of supergranulation measured on Doppler images at disk center yield velocities in the range of 5–$15\,\mathrm{m\,s^{-1}}$ (Giovanelli 1980;

Hathaway et al. 2002; Duvall and Birch 2010). So far, the origin of supergranulation is not clear. It seems likely that it represents the extension of convection to larger scales (Rincon and Rieutord 2018). Why the convective power spectrum has a peak at supergranulation scales and drops towards larger spatial scales is however not yet understood.

The convective motions of granulation and supergranulation buffet the magnetic field on the solar surface, creating a random walk motion of the field. On sufficiently large scales (larger than the supergranulation), their net effect can be described as a diffusion process (Leighton 1964; Martin-Belda and Cameron 2016). The supergranular flows transport the field into the supergranular downflow lanes, which creates the observed network structure of the quiet-Sun magnetic field (cf. Fig.1.1, top right panel).

The random convective motions excite waves in the Sun. These were first identified by Leighton et al. (1962) and are now famously known as the five-minute oscillations. They are the source for understanding the solar interior with measurements from global and local helioseismology. As the work presented here focuses on surface flow measurements derived from tracking of surface features and direct Doppler imaging, the helioseismic techniques are not covered. For introductions to these, the reader is referred to Christensen-Dalsgaard (2003), Gizon and Birch (2005), and Gizon et al. (2010).

In addition to the above flows, which are present on the Sun on a global scale, there are several flows that are directly linked to the presence of magnetic field on the solar surface. These are outlined below.

Evershed flow: The Evershed flow was first discovered by Evershed (1909). It is a systematic plasma motion within sunspots, directed radially outwards from the edge of the umbra towards the outer edge of the penumbra (the sunspot boundary). It is aligned with the filamentary structure of the penumbra (Bellot Rubio et al. 2003). Average velocities of the Evershed flow are on the order of a few $km\,s^{-1}$, with peak horizontal velocities on the order of $6\,km\,s^{-1}$ (e.g. Shine et al. 1994; Solanki 2003; Bellot Rubio et al. 2003; Siu-Tapia et al. 2018). A first explanation of the Evershed flow was the siphon model by Meyer and Schmidt (1968), in which a flow is driven between two footpoints of different magnetic field strengths. The Evershed flow is now believed to be the horizontal component of overturning convection in an inclined magnetic field (e.g. Scharmer et al. 2008; Siu-Tapia et al. 2018). For more on the theory of the Evershed flow, see the review by Solanki (2003).

Moat flow: In addition to the Evershed flow, there is the moat flow (Sheeley 1972), which lies outside of the spot boundary, and points radially away from the spot. The moat flow spans about $30\,Mm$, which is similar to the supergranulation scale (e.g. Sobotka and Roudier 2007; Verma et al. 2018). It has been suggested that it is in fact an annular supergranule (e.g. Sheeley 1972; Meyer et al. 1974), and that the flux concentration that forms the spot has been pushed towards the upstreaming center of the supergranule. Horizontal velocities are typically on the order of $500–1000\,m\,s^{-1}$ (Sobotka and Roudier 2007; Vargas Domínguez et al. 2008; Löhner-Böttcher and Schlichenmaier 2013; Verma et al. 2018). The spot surroundings in which the moat flow is seen are almost devoid of magnetic field, with the exception of so-called moving magnetic features, which were first observed by Sheeley (1969) and named by Harvey and Harvey (1973). Studies suggest that the formation of the moat flow depends on the existence of a penumbra, e.g. Vargas Domínguez et al. (2008) observed a moat flow only in the direction from the spot where a penumbra had formed.
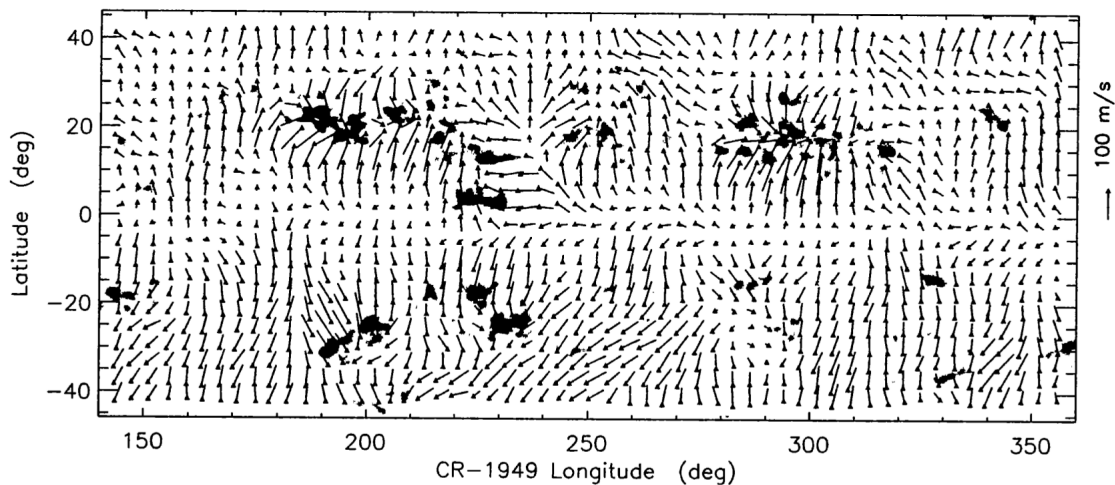
Figure 1.7: Inflows around active regions. The black patches indicate the magnetic field. An example of the inflows around active regions can be seen at the large active region complex at Carrington longitude 300°, Carrington latitude 20°. From Gizon et al. (2001), with permission[3].

Inflows around active regions: Inflows around active regions were first identified by Gizon et al. (2001) and Haber et al. (2001). Figure 1.7 shows the plot from Gizon et al. (2001). They used time-distance helioseismology in the top 2 Mm below the photosphere, with an effective temporal average of 7.5 days, to create synoptic flow maps. In these maps, inflows towards the centers of large, evolved active region complexes are visible. The velocity of these inflows is on the order of $50\,\mathrm{m\,s^{-1}}$, and they were reported to span more than $10°$ away from the center of the AR complexes. In Fig. 1.7, the inflows are slightly more prominent in the latitudinal direction. Haber et al. (2004) did a similar analysis on a large active region complex using ring-diagram analysis at different depths, with a grid scale of $7.5°$. They found inflows with typical velocities of 20–$30\,\mathrm{m\,s^{-1}}$ down to a depth of 7 Mm, and diverging flows at a depth between 9–14 Mm. The same active region was studied by Zhao and Kosovichev (2004) using time-distance helioseismology, with similar results. This was added on to by Hindman et al. (2009), at higher resolution ($2°$). In addition to inflows, these authors measured a cyclonic rotation of about $5\,\mathrm{m\,s^{-1}}$ around the outer edge of ARs, and an anticyclonic rotation of about $10\,\mathrm{m\,s^{-1}}$ around strong-field areas, which they associate with the moat flow around sunspots. They further found that these vortical motions increase towards higher latitudes, and argued that both could be driven by the Coriolis force.

The study of these inflows around evolved ARs stands in close connection to the study of flows around emerging active regions. Komm et al. (2011, 2012) inferred the vertical flows and vorticity in conjunction with the active region inflows, for emerging and decaying ARs. They found upflows of less than $1\,\mathrm{m\,s^{-1}}$ and an increase in the vorticity for emerging flux, and the opposite (downflows and a decrease in the vorticity) for decaying flux. In these works, the authors investigated the flow properties on an extensive sample of regions, rather than individual case studies. This has the advantage that the individual

---

[3] Republished with permission of Springer; permission conveyed through Copyright Clearance Center, Inc.

peculiarities of active regions are taken out of consideration, and instead the statistically average behavior can be studied. Other works applying a larger sample of ARs include a series of papers (Leka et al. 2013; Birch et al. 2013; Barnes et al. 2014), where the authors studied the emergence process of a sample of more than a hundred active regions in comparison to a sample of quiet-Sun control regions of equal size. This approach helps in estimating the noise in the measurements, and in distinguishing whether observed signatures are in fact linked to the presence of magnetic field and its emergence. Birch et al. (2013) found a signature representing a converging flow on the order of $15 \, \mathrm{m \, s^{-1}}$ in the day before emergence. This was later confirmed by Birch et al. (2019).

The above works mostly applied techniques of local helioseismology. A complementary work was carried out by Löptien et al. (2017), who used correlation tracking of solar granulation to infer the flow field on the solar surface. Again, inflows around an individual, large active region were found, with typical velocities of 20–$30 \, \mathrm{m \, s^{-1}}$ and spatial extents of about $10°$ from the center of the region. An average over a large sample of high-flux regions (above $5.9 \times 10^{21} \, \mathrm{Mx}$) showed inflows on the order of $15 \, \mathrm{m \, s^{-1}}$. However, the flows were smoothed with a Gaussian filter of width $\sigma = 4°$, such that, as in other previous studies, the extent of the inflows cannot be resolved at smaller spatial scales.

So far, the inflows were identified either on individual ARs, or on larger samples, with no distinction in active region properties. A first work into the direction of describing a sequence of the inflows in terms of active region properties was done by Braun (2019). They binned a sample of about 5000 observations from more than 300 active regions into five subsamples, with respect to the amount of magnetic flux of the regions. They found that the inflows have similar velocities and spatial extents for the different flux bins. In addition, they reported a retrograde flow of about $10 \, \mathrm{m \, s^{-1}}$ flanking predominantly the poleward side of the average active region. A description of the temporal evolution of the inflows is however missing.

The physical cause of these inflows is still not clear. Spruit (2003) suggested that the magnetic field leads to an increase of the radiative surface cooling, which creates a temperature gradient that drives the inflows. Warnecke et al. (2016) suggested that the negative effective magnetic pressure instability (NEMPI) could explain the converging flows around magnetic flux concentrations. In this mechanism, the turbulent convection in a large-scale magnetic field reduces the effective magnetic pressure, leading to a pressure deficit and inflows (see also Brandenburg et al. 2016 and references therein). It is further not clear whether the converging flows before emergence are driven by the same mechanism as the inflows seen around evolved ARs.

Inflows around ARs potentially play an important role in the transport of magnetic flux, and therefore in the solar dynamo: As they depend on the presence of magnetic field, they could provide a non-linear feedback mechanism required for the dynamo (Cameron and Schüssler 2012). In this scenario, stronger field experiences stronger inflows, which increases flux cancellation and saturates the dynamo. This behavior was found in the surface flux transport simulations by Martin-Belda and Cameron (2016) and Martin-Belda and Cameron (2017b). Other authors have included the inflows around active regions in their surface flux transport models (SFTMs), e.g. De Rosa and Schrijver (2006), Jiang et al. (2010), Cameron and Schüssler (2012), and Yeates (2014). In the work of De Rosa and Schrijver (2006), the parameterized inflows from all directions towards ARs inhibited flux escape and produced long-lived flux clumps, which are inconsistent with observations.

1.3 The Helioseismic and Magnetic Imager

For detailed studies of active regions and the flows that are associated with them, data with both a reasonable spatial resolution and a good temporal coverage are vital. Specifically for this work, where the surface flows are inferred from correlation tracking of solar granulation, the resolution of the instrument needs to be high enough for granulation to be discernible. This is achieved with the Helioseismic and Magnetic Imager (HMI, Schou et al. 2012) onboard the Solar Dynamics Observatory (SDO, Pesnell et al. 2012). SDO was launched into a geosynchronous orbit on 11 February 2010; normal science operations began in May 2010. Besides HMI, SDO carries the Atmospheric Imaging Assembly (AIA) and the Extreme Ultraviolet Variability Experiment (EVE). SDO and HMI are still operational, more than six years after the end of the prime mission.

HMI takes full-disk images of the solar disk in the four Stokes polarization parameters, sampling the profile of the 6173 Å FeI line with six narrow-band filtergrams. From these, several data products are derived: continuum intensity images (ic), line-of-sight as well as full vector magnetic field maps (B_{los} and $\boldsymbol{B}$, Hoeksema et al. 2014), and maps of the Doppler velocity (v). The images have a size of 4096 x 4096 pixel. The pixel scale of $0.505''$ (Schou et al. 2012) corresponds to a spatial resolution at disk center of about 700 km, which is smaller than the typical granule. The standard data products have cadences of 45 and 720 s; the vector magnetic field data are only available with a cadence of 720 s. A number of secondary data products are provided, such as the space weather active region patches (SHARP, Bobra et al. 2014) or flow data from the ring-diagram analysis pipeline (Bogart et al. 2011a,b).

1.4 Local correlation tracking

Local correlation tracking (LCT) is a method to infer motions of small-scale features between two images. It was first used in the solar context by November and Simon (1988). Figure 1.8 shows a sketch of the method: The two images have the same field of view and are taken at different times t and $t + \Delta t$, with a time interval Δt between them. From both images, a small subimage is extracted. The motion of structures from the first to the second subimage is inferred by shifting features in the subimage taken at $t + \Delta t$, such as to maximize the correlation between the pair of subimages. This is done for subimages centered on all pixels of the original images, to retrieve a flow map of the whole field of view. When both Δt and the physical distance between grid elements (that is, pixels) in the images are known, the velocities in the map can be translated into units of $\mathrm{m\,s^{-1}}$. For a consistent result, the time interval Δt needs to be sufficiently small so that the evolution of the tracked small-scale features is not important, that is, they retain their shape.

In the context of this work, solar granulation in HMI continuum intensity images serves as the small-scale feature. While individual granules have significant proper motions, the average motion over many granules is a tracer of the large-scale flow fields. The time interval Δt that is used here in this work is the 45 s cadence of HMI (see above), which is well below the average lifetime of granules (see Sect. 1.2).

The principle of LCT is also used on other observations, such as extreme ultraviolet images (Verma et al. 2018), magnetograms (e.g. Chae et al. 2004; as well as the DAVE
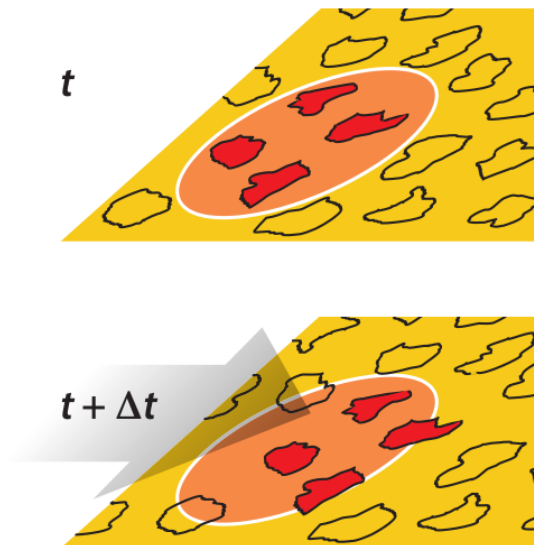
Figure 1.8: Sketch of the method of local correlation tracking. The two images, taken at times t and $t + \Delta t$, contain small-scale features. The motions of these features are inferred by maximizing the correlation between the two images. From Hanasoge et al. (2016), with permission[4].

code, Verma et al. 2018) and Doppler images (e.g. Sangeetha et al. 2020). Similar to local correlation tracking is the method of coherent structure tracking (CST, Roudier et al. 2013), where individual granules are tracked over their lifetime. Other methods to infer velocities on (or close to) the solar surface include measurements from direct Doppler imaging, and the various local helioseismic techniques (ring-diagram analysis, time-distance helioseismology, and helioseismic holography, see e.g. the review by Gizon and Birch 2005).

This work uses the data processing of Löptien et al. (2017). They applied LCT with the FLCT code (Welsch et al. 2004; Fisher and Welsch 2008) on six years of HMI continuum intensity data. This processing includes corrections for systematic errors, which in part are inherent to LCT, and in part stem from the motion of SDO around the Earth and the motion of SDO/Earth around the Sun. For the present work, the LCT processing was improved, in order to account for additional issues that were found. The details for these are given in Sects. 2.2.2 and 2.3.

1.5   Motivation and thesis outline

The previous sections outline how the emergence process of active regions involves many different aspects: The depth at which the magnetic field is generated, the rise speed, the twist and tilt of the flux together with its interaction with the convective motions, as well as flow features. Once the field has emerged, advection by the various surface flows

---

plays an important role, which has implications on the amount and the distribution of flux. This in turn has an effect on the contribution of the emerged field to the solar dynamo. Understanding the role of the flows associated with flux emergence can therefore help constrain the conditions of flux emergence. This has become possible with the availability of high-cadence, full-disk data at a resolution sufficient to discern granulation, with which solar surface flows can be inferred.

The main focus of this work is to analyze the evolution of the surface flows associated with the emergence of active regions. Building on this, in the second part I aim to assess the influence of these flows on the evolution of the magnetic field in the first days after emergence.

In Chapter 2, I study the evolution of the flows around emerging active regions. For this, I use surface flow measurements from local correlation tracking on a sample of 182 emerging active regions. The flow data are corrected for various systematic effects and validated with synthetic data as well as measurements from direct Doppler imaging. To assess the presence of moat flows in the data, I carry out a quantitative classification of the sunspots in each active region. This identifies spots with clear penumbra, which host a moat flow, in about half of the ARs in the sample. I find that in the day prior to emergence, a converging flow towards the center of the emergence location forms. This is irrespective of the flux of the active regions. After the emergence, inflows form, predominantly in the latitudinal direction. The onset time of these inflows depends on the flux of the active region: They form between one and four days after emergence, at increasingly later times for ARs with higher flux.

In Chapter 3, I investigate the effect of the inflows around active regions and the supergranular motions (as the main component of the LCT flow maps) on the evolution of the magnetic field in a local surface flux transport model. For this, I use parametrizations of the inflows from the literature as well as the surface flow measurements from LCT from Chapter 2. The simulations are carried out on 17 active regions, which are selected by excluding ARs with a clear sunspot with penumbra, because the moat flow around such spots would disrupt the magnetic field in the flux transport simulation. For a direct comparison between the simulation output and the observations, the regions are also required to remain on the visible disk for more than five days after the bulk of the flux has emerged. I find that the inflows around active regions do not play an important role during emergence, as the increase in flux cancellation caused by the converging flows is balanced by the decrease in diffusion of flux away from the AR. On the other hand, the supergranular flows are effective in buffeting the active region polarities, which is consistent with a diffusion process. With the sample size and the constraint to only a few days over which comparisons to the observations are possible, I cannot constrain the corresponding diffusivity beyond the range of about 250–$720 \, \mathrm{km}^2 \, \mathrm{s}^{-1}$.

In Chapter 4, I study the average vertical vorticity around active region polarities on a sample of 20 emerging active regions. The vorticity is inferred from the same LCT measurements used in Chapter 2. I find that during the first twelve hours after emergence, the two polarities are on average associated with vortical flows of opposite signs.

Chapter 5 discusses the main conclusions of this work and presents perspectives for future work.

2 Evolution of solar surface inflows around emerging active regions*

Abstract

Context. Solar active regions are associated with Evershed outflows in sunspot penumbrae, moat outflows surrounding sunspots, and extended inflows surrounding active regions. Extended inflows have been identified around established active regions with various methods. The evolution of these inflows and their dependence on active region properties as well as their effect on the global magnetic field are not yet understood.

Aims. We aim to understand the evolution of the average inflows around emerging active regions and to derive an empirical model for these inflows. We expect that this can be used to better understand how the inflows act on the diffusion of the magnetic field in active regions.

Methods. We analyzed horizontal flows at the surface of the Sun using local correlation tracking of solar granules observed in continuum images of the Helioseismic and Magnetic Imager (HMI) on board the Solar Dynamics Observatory (SDO). We measured average flows of a sample of 182 isolated active regions up to seven days before and after their emergence onto the solar surface with a cadence of 12 hours. About half of the active regions in the sample developed sunspots with moat flows in addition to the surrounding inflows. We investigated the average inflow properties with respect to active region characteristics of total flux and latitude. We fit a model to these observed inflows for a quantitative analysis.

Results. We find that converging flows of about 20–$30 \, \mathrm{m \, s^{-1}}$ are first visible one day prior to emergence, in agreement with recent results. These converging flows are present regardless of the active region properties of latitude or flux. We confirm a recently found prograde flow of about $40 \, \mathrm{m \, s^{-1}}$ at the leading polarity during emergence. We find that the time after emergence when the latitudinal inflows increase in amplitude depends on the flux of the active region, ranging from one to four days after emergence and increasing with flux. The largest extent of the inflows is up to about $7 \pm 1°$ away from the center of the active region within the first six days after emergence. The inflow velocities have

amplitudes of about $50\,\mathrm{m\,s^{-1}}$.

2.1   Introduction

Active regions (hereafter ARs) are patches of magnetic field at the surface of the Sun. They are host to sunspots that are visible in white-light images (van Driel-Gesztelyi and Green 2015) and the site of a large variety of phenomena, such as flares and coronal mass ejections. Theories of active region formation include a buoyant rise of magnetic flux tubes from the bottom of the convection zone (see the review by Fan 2009), as well as a formation in the bulk of the convection zone (Nelson et al. 2013) or in the near-surface layers (Brandenburg 2005).

At the surface, active regions are advected on large spatial scales by differential rotation (Snodgrass 1983) and the meridional flow (Duvall 1979). On smaller scales, the magnetic field is diffused by the turbulent convective motions of granulation and supergranulation (Leighton 1964). Methods for inferring the large-scale flows include tracking the motions of small-scale convective or magnetic features, which are displaced by the larger-scale motions, as well as a variety of tools for the analysis of solar oscillations, which are known as local helioseismology (see the review by Gizon and Birch 2005).

In addition, Gizon et al. (2001) found that evolved active regions are surrounded by horizontal converging flows. The authors used time-distance helioseismology (Duvall et al. 1993) to study flows near the surface of the Sun. These surface inflows typically extend to about $10°$ from the active region and have horizontal velocities of up to $50\,\mathrm{m\,s^{-1}}$ (Gizon et al. 2001; Haber et al. 2004; Zhao and Kosovichev 2004; Hindman et al. 2009; Löptien et al. 2018; Braun 2019). It is an interesting question to determine what drives these inflows. Enhanced emission of radiation in the magnetic field structures might lead to a horizontal temperature gradient that could drive the flows (Spruit 2003).

The inflows toward active regions are important as they affect the advection and flux cancellation of ARs, and may counteract diffusion (De Rosa and Schrijver 2006). De Rosa and Schrijver (2006) and Martin-Belda and Cameron (2017a,b) included models of the inflows into surface flux transport simulations, showing that they can provide a feedback mechanism that saturates the amplitude of the global magnetic field. This could explain observed variations in solar cycle strengths.

Several studies have applied local helioseismic techniques to investigate different aspects of the properties of these flows. Haber et al. (2004) studied their depth dependence, identifying a transition to outflows in deeper layers for some ARs. Komm et al. (2011, 2012) studied vertical flows and vorticity, finding that emerging flux is associated with weak upflows of less than $1\,\mathrm{m\,s^{-1}}$ and increasing strength of vorticity, and that decaying flux is associated with downflows and decreasing strength of vorticity.

Recently, Braun (2019), using helioseismic holography (Lindsey and Braun 2000), investigated a sample of 336 ARs and derived flow patterns for subgroups of increasing magnetic flux. This work showed that the amplitude of the flows increases with magnetic flux, and reported a retrograde flow component mainly at the poleward side and, less distinct, the equatorward side of the AR.

Löptien et al. (2017) used local correlation tracking (LCT, November and Simon 1988) of the convective granulation pattern on the solar surface to measure inflows around an

average high-flux AR. The regions in their sample have fluxes higher than 5.9×10^{21} Mx. Their work confirms inflows of about 20–30 m s^{-1} that extend about 10° from the AR.

Birch et al. (2019) found a compact (less than 2°) converging flow of about 40 m s^{-1} in the day before active region emergence, using both LCT and helioseismic holography as independent methods for flow inferences on the surface. Comparisons of flows derived with LCT and local helioseismology showed that the two methods agree well (Švanda et al. 2013; Birch et al. 2016).

In this study, we aim to measure the evolution and structure of the inflows around active regions at the solar surface during the early stages of the active region evolution, that is, before, throughout, and in the days after emergence. We also investigate potential differences in the inflows related to the total unsigned flux and the latitude of the active regions.

We performed a statistical study by averaging over a large sample of ARs. For this, we made use of the SDO helioseismic emerging active regions (SDO/HEAR) survey (Schunker et al. 2016). By using this sample rather than performing a case study, we decrease background noise as well as peculiarities of individual emerging active regions (EARs), which can have a dominating effect on the flow structure.

The paper is structured as follows: In Sect. 2.2 we describe the sample of emerging active regions as well as the flow measurements. Section 2.3 illustrates the data processing that we applied to derive the evolution of flows around ensemble averages of ARs. Section 2.4 presents our results, followed by a discussion (Sect. 2.5).

2.2   Data

2.2.1   Sample of emerging active regions

Schunker et al. (2016) described the HEAR survey in detail. We summarize the main aspects below.

The HEAR survey comprises 182 emerging active regions during the time from 2010 to 2014. They were selected from the National Oceanic and Atmospheric Administration (NOAA) solar region reports on the basis of several criteria, requiring that the AR (a) reaches a total sunspot area of at least 10 micro hemispheres (μH; 1 μH $\approx$ 3 Mm^2), (b) is first recorded by NOAA within 50° of the central meridian, and (c) emerges into the quiet Sun, without preexisting large-scale flux within a radius of 18°. These criteria were chosen to minimize contamination by preexisting magnetic field and to reduce projection effects. The emergence time of each active region is defined as the time at which the region has reached 10 % of the maximum unsigned flux within the first 36 h after the active region is first recorded by NOAA. The survey also provides the Carrington longitude and latitude, as well as the start and end times of the observations for each region.

In addition to the emerging active regions, the survey includes one quiet-Sun control region for each EAR. These control regions match their corresponding EARs in latitude and distance from the central meridian at a mock-emergence time, at which there are no numbered SHARP regions within a radius of 18° of the control region. These control regions are important as a comparison against which any measurement on the EARs can be tested.

2.2.2 Flows inferred from local correlation tracking

We used an updated version of the flow maps generated by Löptien et al. (2017), who described their processing procedure in detail. We summarize the important aspects below.

Löptien et al. (2017) applied LCT on full-disk continuum intensity images from SDO/HMI (Schou et al. 2012). Specifically, they ran the FLCT code (Welsch et al. 2004; Fisher and Welsch 2008) on hmi.ic_45s series data, starting on 24 April 2010 and ending on 27 April 2016. In order to reduce computation time, only one flow measurement every 30 min was calculated by cross-correlating pairs of images that are 45 s apart. Each measurement consists of a map of velocities v_x in x-direction and a map of velocities v_y in y-direction (with x and y in CCD coordinates).

Local correlation tracking is known to underestimate flow velocities (see, e.g., Löptien et al. 2016a; Verma et al. 2013; Švanda et al. 2007 and references therein). This was addressed by generating calibration data with which the flow velocities were then corrected (see Sect. 2.1 of Löptien et al. 2017).

The noise in LCT calculations increases to the limb due to projection effects. Therefore the flow maps were cropped at $60°$ from disk center. The maps show systematic effects, such as the orbital motion of HMI and the shrinking-Sun effect (Lisle and Toomre 2004; Löptien et al. 2016b), a systematic converging flow toward disk center. This was addressed by representing the background signal of the flow maps as a sum of low-order Zernike polynomials (up to radial degree $n = 7$). The time series of the Zernike polynomial coefficients were then transformed into Fourier space, where frequencies corresponding to known periods of systematic effects were isolated. These are the 24-hour period of the satellite orbit and its 23 observed harmonics, and the 365-day period of the Earth orbit and its first 16 harmonics (down to a period of 22.8 days), which show significant power. The filtered, backtransformed background estimate was then subtracted from the observations.

An exception was made for the time series of Zernike polynomials $Z_1^{-1} = y$ for the v_x maps and $Z_1^1 = x$ for the v_y maps, which are correlated to each other and were therefore not treated in the way outlined above. For these, the first element of a principle component analysis of the two components was subtracted (as described in Appendix B of Löptien et al. 2017). However, this retained a systematic variation for these terms on the order of several m s^{-1} with a period of 24 hours and its harmonics, which corresponds to large-scale gradients in the flow maps. To correct for this, we repeated the data processing of Löptien et al. (2017), subtracting for the Zernike polynomials $Z_1^{-1} = y$ for v_x and $Z_1^1 = x$ for v_y the same harmonics as for the other components. In this rerun, the data coverage was increased to 6 March 2020.

As a last step, we remapped the velocity maps from the CCD coordinate system to Plate Carree projection (Carrington longitude, latitude), with a total size of 3600 x 1200 grid points and a grid spacing of $0.1°$. In this projection, averaging over regions at different latitudes and longitudes can be done in a straightforward manner. In the same step, the velocities were transformed from v_x, v_y into the longitudinal and latitudinal velocities v_{lon}, v_{lat}. We then applied a Gaussian filter with a width of $0.4°$ and subsampled to the grid spacing of $0.4°$ used by Löptien et al. (2017). This processing step differs from Löptien et al. (2017) so that aliasing is removed from the data.

2.3   Data reduction

2.3.1   Processing and validation of the flow data

In the flow maps, individual pixels occasionally show unrealistically high values. This affects about 10 pixels per map, mostly close to the limb. We speculate that these arise from the decreased contrast at the limb in combination with the evolution of the granules. To mitigate their effect, we replace outlier pixels that are outside five standard deviations of the mean of the velocity distribution by the mean value of pixels surrounding them in a box of 5 pixel × 5 pixel.

In addition to the systematic effects described above (the orbital motion of SDO and the shrinking-Sun effect), the LCT data exhibit another long-term, large-scale modulation: At the beginning of the time series in 2010, the longitudinal flow component v_{lon} has a bias toward prograde (retrograde) velocities in the eastern (western) half of the disk, and the latitudinal flow component v_{lat} has a bias toward southward (northward) velocities in the northern (southern) half of the disk, mostly at latitudes above 30°. Over the years, this modulation changes, such that the hemispheric biases of the two flow components reverse sign in about 2014. The amplitude of this modulation is about $10\,\text{m s}^{-1}$ in a half-year average. The reason for this modulation is not fully understood. Its timescale does not correspond to any known periodic effects, such as the B angle or the orbital motion of HMI.

To correct for this large-scale modulation, we translated all velocity maps from Carrington longitude into Stonyhurst longitude, created running time averages over half a year of data each, centered ten days apart, and subtracted these from every individual map from five days before until five days after the central time of the average. The corrected maps were then mapped back to Carrington longitude. We chose an averaging time of half a year because a shorter timescale might subtract real flows. The spacing of ten days was chosen to avoid drastic changes between two blocks of subtraction. The average maps were smoothed with a Gaussian of $\sigma = 0.8°$ to reduce small-scale effects.

The above processing was necessary to address the various systematic errors, namely the orbital motion of HMI, the shrinking-Sun effect, and the long-term modulation. The velocities that we measure throughout our analysis are therefore relative to velocities $v_{\text{lon}} = 0$, $v_{\text{lat}} = 0$, which are the half-year time averages at each location in Stonyhurst longitude and latitude.

As a test of this processing, we wished to be sure that the Zernike subtraction outlined by Löptien et al. (2017) did not subract the types of flows we wished to study together with the systematic effects. To evaluate by how much this procedure alters the inflows, we created one Carrington rotation of synthetic flow data with inflow features and applied the same filtering on them as on the actual data. Appendix 2.6.1 describes this test. We find that the extent and amplitude of the synthetic flows is well preserved, with changes of less than $5\,\text{m s}^{-1}$ for model inflows with an amplitude of $50\,\text{m s}^{-1}$. Small deviations are introduced to the data, with amplitudes of less than $5\,\text{m s}^{-1}$.

As another test of the LCT flows used in this study, we carried out a control run against an independent data set. In this test, we projected the LCT flows onto the line-of-sight component and compared them to flow measurements obtained from direct Doppler images from SDO/HMI. Appendix 2.6.2 describes this test. The Dopplergrams only provide one

velocity component and are therefore not suitable as the main flow measurement of this study. We find that the two methods agree well in general, with correlations exceeding 0.8, except for in close proximity (2°) to sunspots. This might be due to the different depths at which the two measurements are taken, and also to different sensitivities in the presence of strong magnetic field.

To use the LCT flow data on the sample of emerging active regions and control regions, for each region we extracted data cubes of the two flow components v_{lon}, v_{lat}, which are centered at the position of the region in Carrington longitude and latitude given in the HEAR survey, and span $\pm 30°$ in both longitude and latitude. The cubes start (end) at the full or half hour before (after) the first (last) observation time given in the HEAR survey. This is because the HEAR survey defined the emergence time from the HARP vector magnetogram observations that have a cadence of 12 min, whereas the LCT data have a cadence of 30 min, with data at full and half hours. For the same reason, we define the time of emergence as the first full or half hour after the time of emergence t_0 in the HEAR survey. We chose this to ensure that the emergence had consistently occurred for all regions.

The typical observation period of an individual region is about nine days (450 frames). The maximum difference between the start (end) of the observations and the time of emergence is seven days (343 frames) before (after) emergence (leaving about two days of observations after (before) emergence). The averaging over ensembles of active regions was done relative to the time of emergence (see Sect. 2.4). The total duration of observations is therefore 14 days, with a varying number of active regions at each time relative to the time of emergence. The parts of each frame that are off the visible disk were not included in any averaging.

To further analyze the characteristics of the EARs, we generated magnetogram and continuum intensity data cubes for each region, matching the setup of the flow data described above. We used the same observation start and end times, with the same 30-minute cadence as for the flow maps (described above) on the continuum intensity series hmi.ic_45s to create the intensity data cubes. The data were remapped to Plate Carree projection, with a grid spacing of 0.1°. This is four times higher than that of the flow maps and was chosen for both continuum and magnetogram data to preserve small-scale information. We corrected for limb darkening and normalized the continuum data cubes by convolving each frame with a Gaussian of $\sigma = 5°$ to retrieve the large-scale variation in the frame (the limb-darkening profile) and then divided the frame by this background. For the magnetograms, we extracted the full-vector magnetic field from hmi.b_720s. From the vector field components, we calculated the radial field B_z using the transformation given by Gary and Hagyard (1990). For pixels in which the field azimuth was not calculated with the minimum-energy algorithm, we used the random field disambiguation (Hoeksema et al. 2014). We then averaged the five frames of the 720 s radial field B_z data together within one hour.

The data of each EAR thus consist of three-dimensional data cubes (time, longitude, and latitude) for the flow components in longitudinal and latitudinal direction, the radial magnetic field, and the continuum intensity. Each cube has frame sizes of $60° \times 60°$ in longitude and latitude, centered at the Carrington longitude and latitude of the AR given in the HEAR survey, and covers about 14 days, centered on the time of emergence, with data coverage of the visible disk for about nine days. The cubes of the velocity maps and the

continuum intensity have a cadence of 30 min. The cubes of the radial magnetic field have a cadence of one hour.

2.3.2   Measuring the location of the magnetic polarities

Over time, the regions move relative to the position given in the HEAR survey. To perform a sensible ensemble average of the active regions relative to their center or their leading or trailing polarity, we measured the positions of the leading and trailing polarities in longitude and latitude in each one-hour radial magnetic field average. To reduce sensitivity to small-scale structure within the AR, we smoothed the magnetograms with a Gaussian of $\sigma = 0.4°$ for this measurement.

For each of the 182 AR we estimate the position of the polarities at one day after emergence by eye as an initial guess. At this time, all regions show a clear bipolar structure. The procedure for each time frame in each of the 182 data cubes is described below.

We estimated the fluctuation in the radial magnetic field as the standard deviation in a box of $12° \times 12°$ around the position in Carrington longitude and latitude from the HEAR survey. The magnetic field of the AR is part of the estimate. The size of the box was chosen to exclude other AR from the field of view; they would bias the estimate.

We then identified regions as neighboring positive (negative) valued grid points (for brevity, called pixels in this context) above (below) a threshold value, taken as 1.5 times the standard deviation. We used this adaptive threshold because the levels of magnetic activity in the vicinity of the individual ARs differ. The factor of 1.5 was applied to further reduce detection noise and is a result of trial and error. The negative and positive polarities were considered separately. Depending on the AR, the positive (negative) field corresponds to the leading (trailing) polarity, or vice versa.

Regions that are only one pixel in size were excluded. These were considered to be too small for a reliable polarity position estimate. We also excluded regions whose flux-weighted center is farther away from the initial (or first-guess, see below) position than $\pm 2°$ to avoid selecting unrelated surrounding magnetic field. This is important especially during emergence, when the field of the AR is still weak.

Of the remaining regions, we identified the region that has the highest absolute sum in B_z. We defined the position of the active region polarity as the longitude and latitude of its flux-weighted center.

This method was iterated forward and backward in time, starting from the frame one day after emergence, when we identified a first-guess position by eye. For each frame, the position from the previous frame was used as first guess.

With this procedure, we determined the positions in longitude and latitude of each polarity for each EAR at each time step. Before emergence, there is only very little magnetic flux of the active region present by definition, which makes a position measurement unreliable, with the risk of identifying surrounding small-scale field. For consistency, we therefore set the positions in all frames before emergence to the values at emergence. We point out that other choices could be made, for example, extrapolating the post-emergence motion to the times before emergence. This would require additional assumptions on the proportionality of the motion over a certain (flux dependent) time interval, however, and was therefore not attempted here.

In some cases, the inferred positions in a single frame differ largely from those before and after, for example, when a connection between two regions is established by pixels that have magnetic field strengths just above the threshold in the particular frame, and below in the previous and the following frame. These artifacts will be present for any choice of threshold. To mitigate this, we smoothed the time series of positions with a Gaussian of width $\sigma = 3\,\mathrm{h}$. We defined the position of the center as half the distance between the leading and trailing polarity positions. The total motion of an AR over the course of the observations is typically a few degrees. The largest displacements are about $6°$ for ARs at high latitudes, at which the difference between Carrington rotation rate and solar rotation rate at the surface is largest.

Other methods for inferring the position of AR polarities are possible. To estimate the difference that this might make for our analysis, we applied the method of Schunker et al. (2019). Their algorithm iteratively calculates the field strengths in the surroundings of all grid points and selects the patch as the polarity that lies closest to the patch in the previous frame. Because our method instead selects the strongest patch, this can lead to differences between the two methods because the dominant patch of magnetic field of one polarity in some ARs is later replaced by another patch. Appendix 2.6.3 compares the two methods. We applied the positions of both methods to ensemble averages of the flow data (see the following sections) and found a standard deviation of the difference of the methods of below $2\,\mathrm{m\,s^{-1}}$ close to emergence, and no systematic difference with respect to the inflows we wished to investigate.

2.3.3   Weight maps for ensemble averages

When ensemble averaging is performed, we have to take into account that at a given time relative to the time of emergence, the active regions have different disk positions and therefore different background noise levels because the noise increases toward the limb. We accounted for this with weighted ensemble averages. For this, we created data cubes of weight maps for all EARs and control regions as described below.

First, we mapped the full-disk velocity field v_{lon}, v_{lat} from the Plate Carree grid with 900 x 300 grid points and a grid spacing of $0.4°$ (see Sect. 2.2.2), from Carrington coordinates into heliocentric Cartesian coordinates (Thompson 2006), centered on the Carrington longitude and latitude at disk center. Transforming into this system accounts for the B angle and the P angle. We mapped with a linear interpolation onto a fixed grid with 300 x 300 grid points and a grid spacing of 0.006 solar radii ($R_{\odot}$) (corresponding to about $4.2\,\mathrm{Mm}$ at disk center). The frame size was $1.8\,R_{\odot}$, which is slightly larger than the LCT data coverage (the $60°$ from disk center of the LCT data corresponds to $2\sin{\pi/3} = 1.73\,R_{\odot}$).

We did this for the whole ten years of LCT data. We calculated the average flows $\langle v_{\mathrm{lon}} \rangle$ and $\langle v_{\mathrm{lat}} \rangle$, and a map of the standard deviation of each flow component (see Fig. 2.1) on the fixed grid in heliocentric Cartesian coordinates. The velocities in the average maps are about $10\,\mathrm{m\,s^{-1}}$, which is far lower than the velocities in an individual map (about $1000\,\mathrm{m\,s^{-1}}$). The reason is that the velocities are equally distributed around zero, with the dominant noise from granulation and supergranulation.

For the longitudinal component, the standard deviation increases mainly toward the east and west limbs. For the latitudinal component, the northern and southern polar regions show the largest standard deviation.
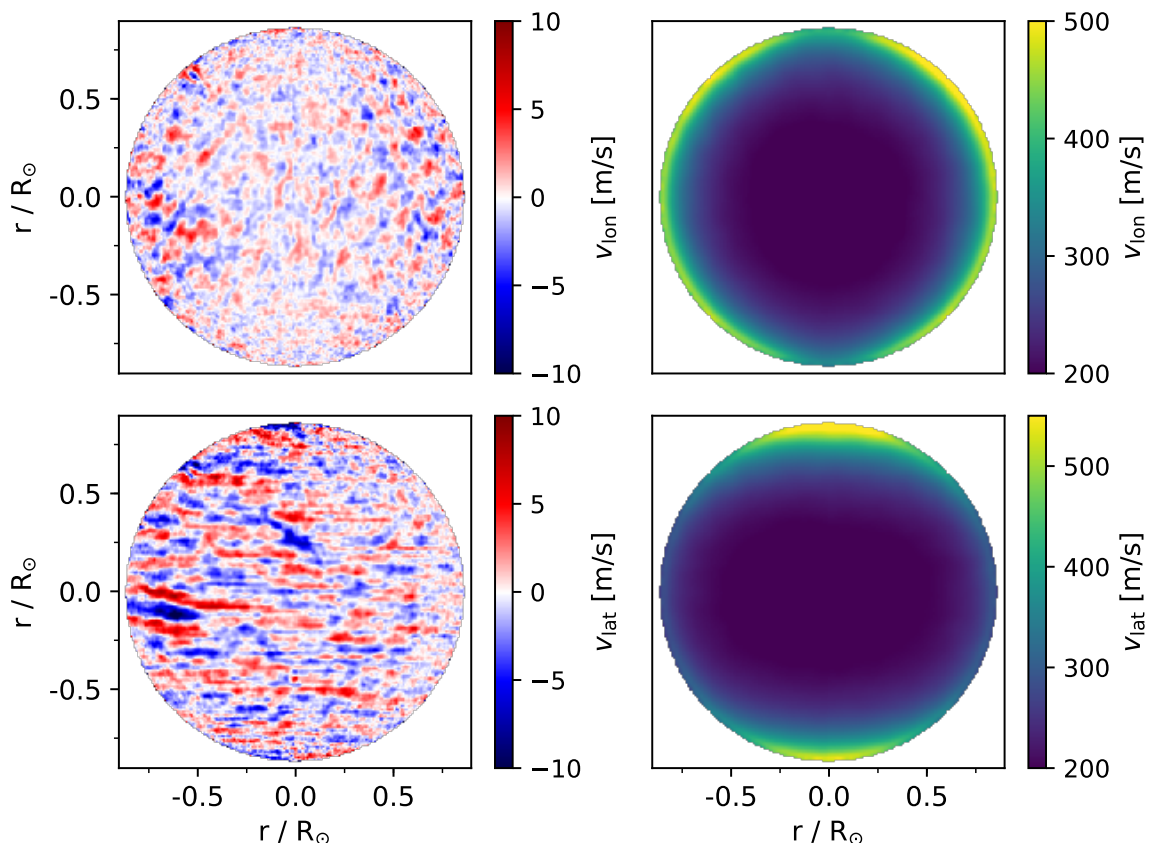
Figure 2.1: Temporal averages (*left panels*) and standard deviations (*right panels*) over the full-disk flow maps from 24 April 2010 to 6 March 2020. The *top and bottom rows* show the longitudinal and latitudinal flow component, respectively.

We generated full-disk weight maps by mapping the standard deviation σ of v_{lon} and v_{lat} back onto the Plate Carree projection in Carrington coordinates. From these, we created data cubes of the weight maps as $1/\sigma^2$ for each of the 182 EARs and control regions in the same way as for the data cubes of the velocity maps (see Sect. 2.3).

2.3.4   Exclusion of magnetic pixels

Local correlation tracking of solar granules is known to be unreliable within regions of strong magnetic field, where the granulation is attenuated. This is the case for sunspots or plage regions, which appear darker or brighter than the quiet Sun in continuum images. The motion that LCT tracks in these regions is therefore a combination of the motion of the granules and the motion of these features. In Appendix 2.6.2, we find that in regions within 2° of sunspots, the LCT flows are weaker than the direct SDO/HMI Doppler velocity measurements. This difference can be attributed to physical causes as well, however, that is, the difference in the height of the two measurements.

To ensure that our measurements are not susceptible to this unreliability, we created additional data cubes of normalized continuum intensity for each AR by binning to the same grid spacing as the flow maps (0.4°). We identified pixels with values lower than 0.95 (pores, sunspots) and higher than 1.05 (plage), where the mean value of the quiet Sun

is 1. In the flow maps, we excluded these pixels if they were connected to at least one other to avoid excluding random high-valued pixels. The numbers are the result of trial and error and represent a compromise between excluding pixels in the quiet Sun that are above or below the thresholds and not excluding pixels that are systematically lower or higher, for example, near the edge of a sunspot.

2.3.5   Ensemble averages

To carry out ensemble averages, we first investigated the dependence of the noise in the flow maps on spatial smoothing, temporal averaging, and the number of ARs in the ensemble average to identify parameters that yield appropriate noise levels for our analysis. Previous studies have reported active region inflows with velocities of about several tens of m s^{-1}. We therefore required the noise to be well below $10\,\mathrm{m\,s^{-1}}$ while still being able to investigate flows on small spatial scales and without loosing much temporal resolution.

For this, we used the sample of control regions of the HEAR survey, where no systematic flows are present. The data cubes of these were prepared in the same way as those of the EARs, with the center of the $60° \times 60°$ maps on the coordinate given in the HEAR survey throughout the observations. For this test, we cropped the frames to the inner $40° \times 40°$, which yielded a more representative value because the errors increase toward the limb and fewer control regions contribute to the average. Like the active regions, the quiet-Sun regions have different disk positions at a given time relative to the assigned 'time of emergence'. For a representative estimate, we started at one day before the time of emergence, where the frames from the control regions are close to disk center on average, and computed the average of N subsequent frames in the range of $N = 1$ (no time average, 30 min resolution) to $N = 96$ (2 days average). They were additionally smoothed by Gaussians of $\sigma = 0.4, 0.8, 1.2, 1.6, 2.0$, and $4.0°$. We calculated the median of the standard error over all individual control regions. Second, we carried out the same calculation at a fixed Gaussian smoothing of $0.8°$ while varying the number of control regions in the average. Figure 2.2 shows the results for the latitudinal flow component. The results for the longitudinal component are very similar.

The top panel of Fig. 2.2 shows that an ensemble average over all 182 ARs requires a spatial smoothing of $0.8°$ to obtain a noise level of about $5\,\mathrm{m\,s^{-1}}$. A time average of 6 or 12 h is sensible because of the timescale on which the flows change. The top panel also shows a least-squares fit of $1/\sqrt{N}$ to the case of Gaussian smoothing of $\sigma = 1.6°$. The noise decreases more slowly than the fit because subsequent maps are correlated due to the lifetime of supergranules. This holds for all cases. The bottom panel of Fig. 2.2 shows that for an ensemble average of fewer than 45 regions, temporal averaging of more than 2 days is necessary at this level of spatial smoothing. For an ensemble average of 45 regions, a time average of 12 h is acceptable.

We used these values for spatial smoothing and temporal averaging for the ensemble averages in our analysis. The temporal averaging was aligned relative to the time of emergence, such that the frame of emergence is the first frame in the first time step after emergence. For the ensemble averaging, Hale's law and Joy's law are taken care of by reversing the latitudinal direction of all data cubes (magnetic field, continuum intensity, and the v_{lon} and v_{lat} flow components) as well as the sign of the magnetogram and the v_{lat} flow component for regions in the southern hemisphere.
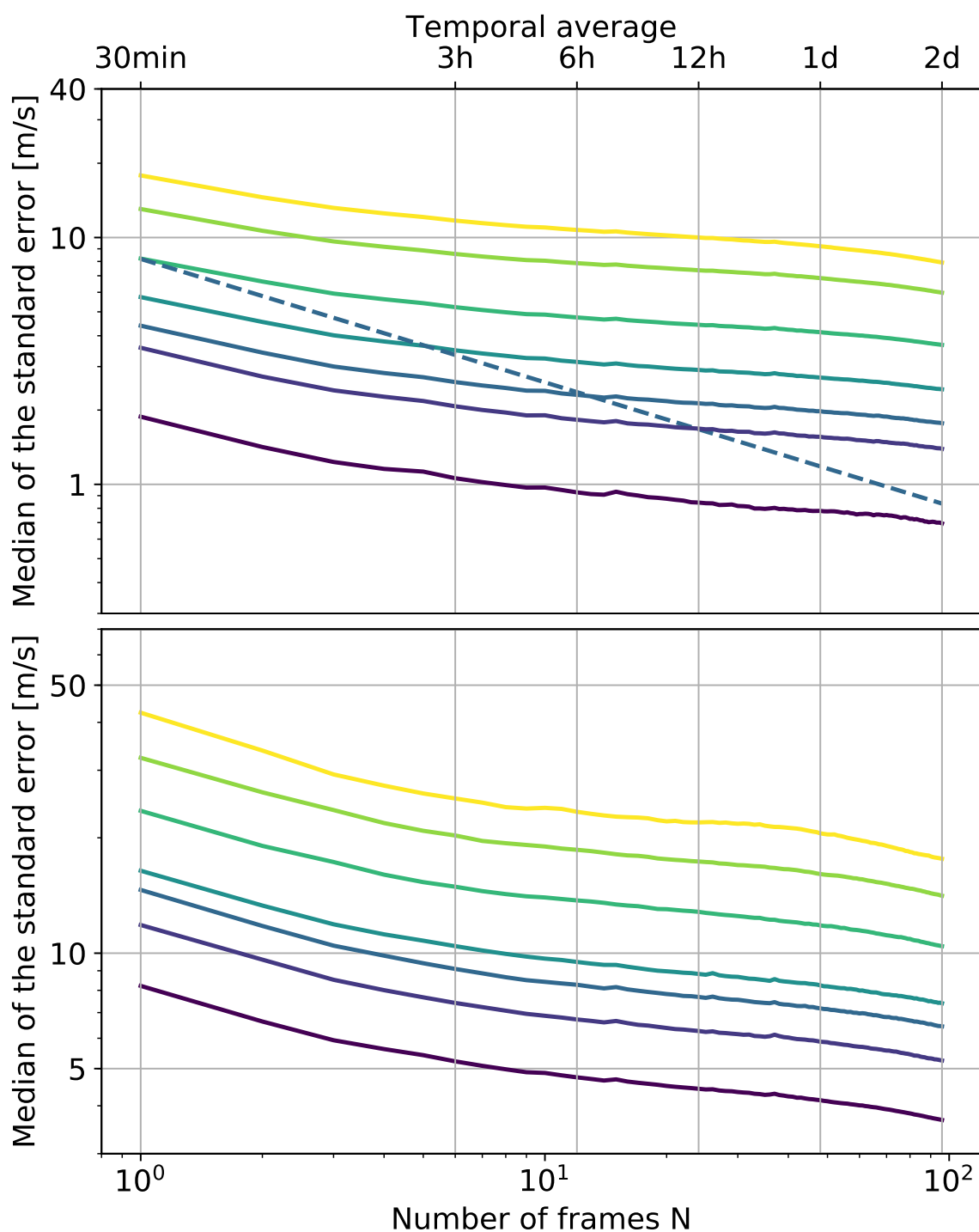
Figure 2.2: Median of the standard error against averaging time. The lines in the *top panel* show the cases of no smoothing (yellow) and of Gaussian smoothing of 0.4, 0.8, 1.2, 1.6, 2.0, and $4.0°$ (green to purple). All lines are from an ensemble average over all 182 ARs. The dotted line shows the $1/\sqrt{N}$ least-squares fit to the case of Gaussian smoothing of $\sigma = 1.6°$. *Bottom*: Same as in the top panel for averages over 5, 10, 20, 45, 60, 91, and 182 control regions (yellow to purple). All lines are with a Gaussian smoothing of $\sigma = 0.8°$. Both panels show the case of the latitudinal flow component. The scale of the y-axis is different in the two panels.

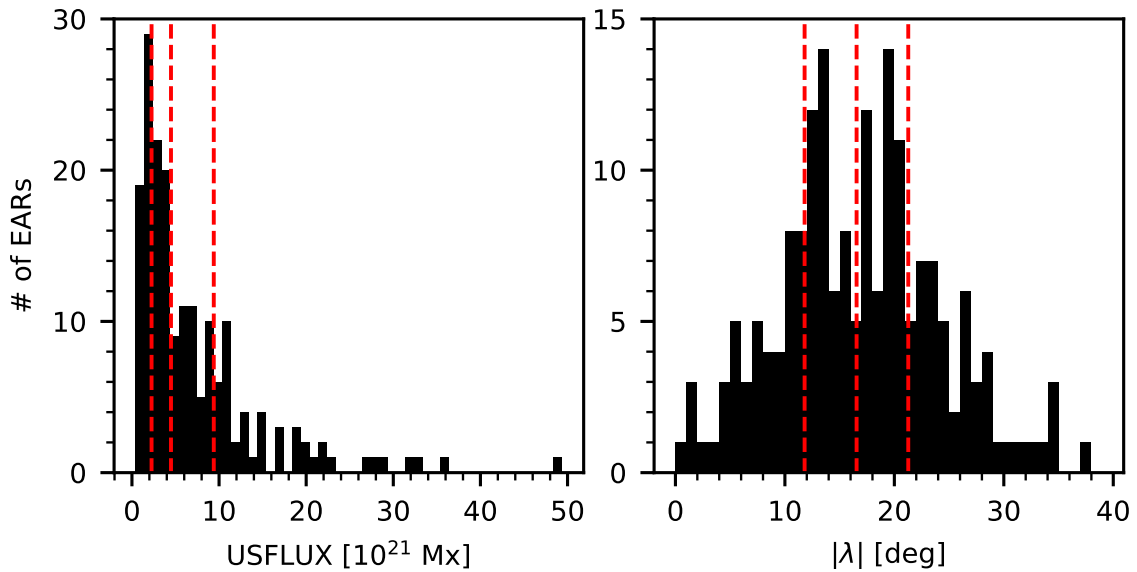Figure 2.3: Distributions of the sample of EARs with respect to the unsigned magnetic flux (USFLUX, *left panel*) and the unsigned latitude $|\lambda|$ (*right panel*). The dotted red lines in the two panels separate the distributions into four subsamples, each containing 45 or 46 active regions, sorted by USFLUX and by $|\lambda|$, respectively.

In addition to the flows around active regions, the flow maps exhibit signatures from the moat flow because sunspots are present in the sample (Sheeley 1972). To better understand their effect on the flow maps, we performed ensemble averages centered on the leading polarity (where we expect the strongest moat flow), in subsamples of the active regions, using a classification scheme to identify whether a sunspot with a clear penumbra is present in an AR at that time. Appendix 2.6.4 describes this test. We find that a moat flow is present in our flow data for regions with a clear sunspot, with typical velocities of about $150 \, \mathrm{m \, s^{-1}}$. The moat flow is not symmetric in this early phase of the active region as the sunspots still grow, in agreement with Vargas Domínguez et al. (2008).

2.4   Results

2.4.1   Flows as a function of time and magnetic flux

We investigated the evolution of the flows around active regions of different maximum values of magnetic flux. For each of the 182 ARs, we retrieved the maximum total unsigned flux from the hmi.sharp_720s series keyword USFLUX in the period covered by the HEAR survey. USFLUX records $\Sigma |B_z| \mathrm{d}A$, with B_z the radial magnetic field component and A the area of the SHARP region (Bobra et al. 2014). From this, we divided the sample into four subsamples, sorted by the maximum unsigned magnetix flux, with two subsamples containing 45 and two subsamples containing 46 EARs.

The left panel of Fig. 2.3 shows the distribution of maximum USFLUX values of all ARs, together with dotted red lines that indicate the boundaries between the four subsamples. The subsamples have mean total unsigned magnetic flux values of 1.5×10^{21} Mx, 3.1×10^{21} Mx, 7.0×10^{21} Mx, and 1.5×10^{22} Mx, respectively.

Figure 2.4 shows several 12-hour time steps for all four subsamples. The first row shows the time step of the flows at -18 h (between 24 and 12 h before emergence). At this time, all subsamples exhibit a converging flow toward the center of the AR. The velocities are about 20–30 m s^{-1}. The noise level is about 10 m s^{-1}, as discussed in Sect. 2.3.5. This converging flow is consistent with that reported by Birch et al. (2019). For the two higher-flux subsamples, the converging flow is spatially more extended than for the lower-flux ones. Shortly after emergence, the lowest-flux subsample still shows small-scale inflows, whereas they have ceased for the other subsamples. The three subsamples with higher flux show a prograde flow with velocities of about 40 m s^{-1} at the position of the leading polarity, similar to the findings by Birch et al. (2019). This feature is not present in the lowest-flux subsample. About two days after emergence (third row in Fig. 2.4), inflows toward the second-lowest flux subsample set in. For the third subsample, they are clearly visible after about three days, while the highest-flux subsample still shows mostly a strong moat flow at this time. For the highest-flux subsample, the inflows only set in at about four days after emergence. From this, we conclude that the inflows take longer to form for large active regions.

After six days, the EARs of the lowest-flux subsample have already mostly decayed. For these small AR, inflows are seen throughout their lifetime, and they decay along with the magnetic field. Over its lifetime, the lowest-flux subsample never exhibits diverging flows, neither moat flows (due to the lack of sunspots with clear penumbra), nor a prograde flow at the leading polarity of the type observed by Birch et al. (2019).

2.4.2   Flows as a function of time and latitude

We examined whether the flows associated with the EARs depend on the latitude at which the EARs emerges. To do this, we divided the sample of 182 ARs into four subsamples of 45 or 46 EARs each, sorted by their unsigned latitude $|\lambda|$ (as provided by the HEAR survey). Each subsample in $|\lambda|$ therefore contains regions with a variety of maximum total unsigned flux values. The right panel of Fig. 2.3 shows the distribution of unsigned latitudes of all EARs together with lines indicating the boundaries between the four subsamples.

Figure 2.5 shows two 12-hour time steps for all four subsamples, one at six hours after emergence, and the other at 4 d and 18 h after emergence. The converging flow toward the center of the active region as well as the prograde flow at the position of the leading polarity around the time of emergence are both present in all four subsamples. Joy's law is clearly visible after emergence, consistent with Schunker et al. (2020), who showed that active regions on average emerge east-west aligned, and that Joy's law becomes evident two days after emergence. The tilt angle increases toward the higher-latitude subsamples and in time. There appears to be no striking systematic change in the inflows as a function of latitude.
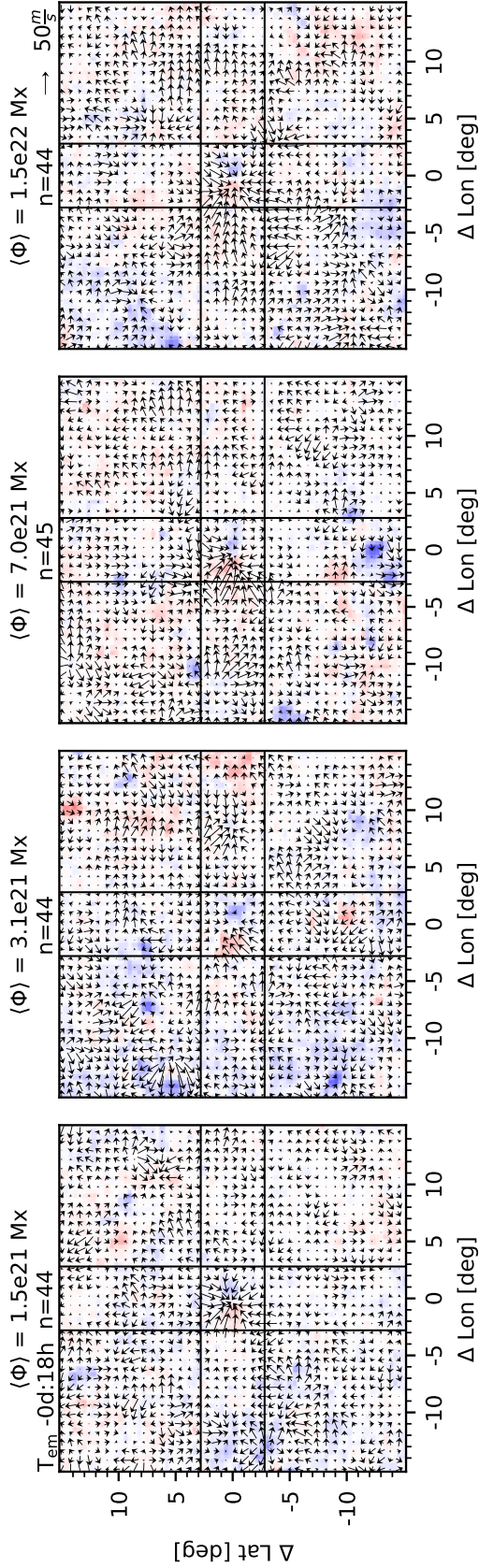
Figure 2.4: Evolution (*from top to bottom*) of the averaged active region magnetic field and flows for the four subsample averages of total unsigned flux (with flux increasing *from left to right*, cf. the left panel of Fig. 2.3). Each time step is an average over 12 h, centered on the labeled time. The axis labels are relative to the center of the AR, as defined in Sect. 2.3.2. For each panel, the total number of active regions that contribute to the average is given at the top. Red (blue) indicates positive (negative) radial magnetic field, saturated at ±150 Gauss. The green circles highlight the time after emergence at which the inflows are first visible in the time steps shown here. The arrows indicate the flows. A reference arrow representing a velocity of 50 m s^{-1} is given in the upper right corner. The black lines mark the averaging range that was used for the model fit (cf. text and Fig. 2.6). A moat flow is apparent in the rightmost column at 3 d and 6 h, for instance.
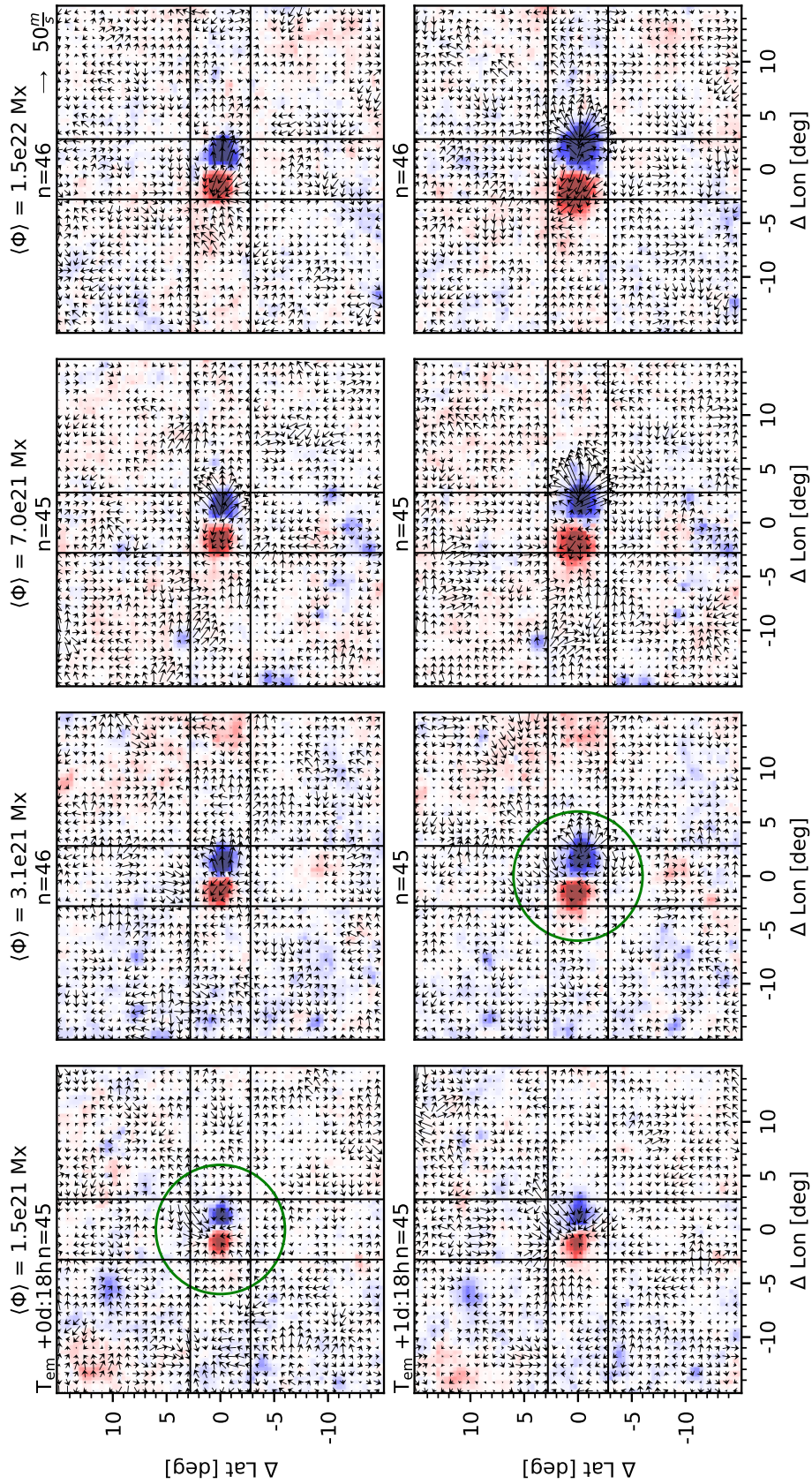
Figure 2.4: (continued)
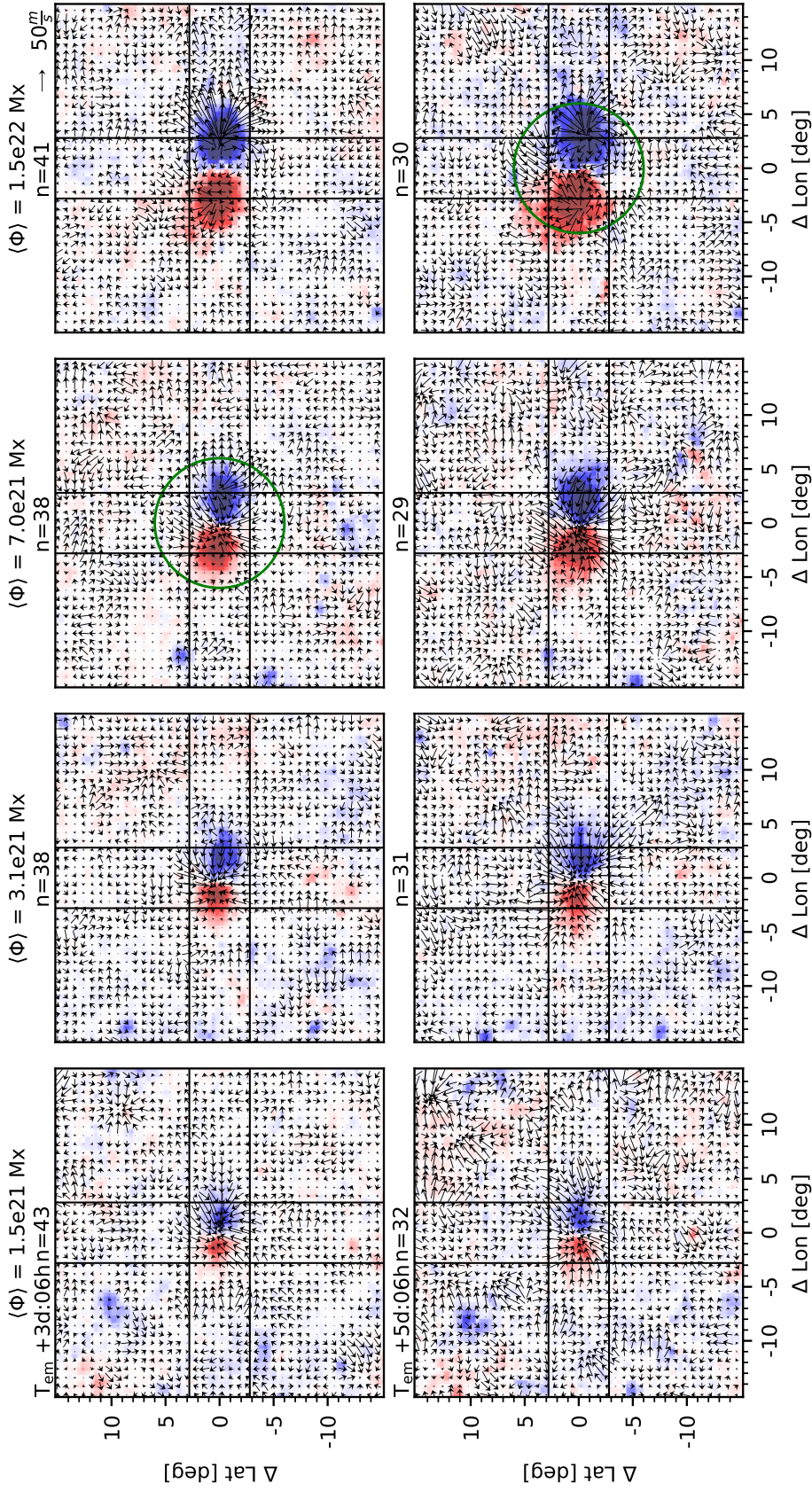
Figure 2.4: (continued)
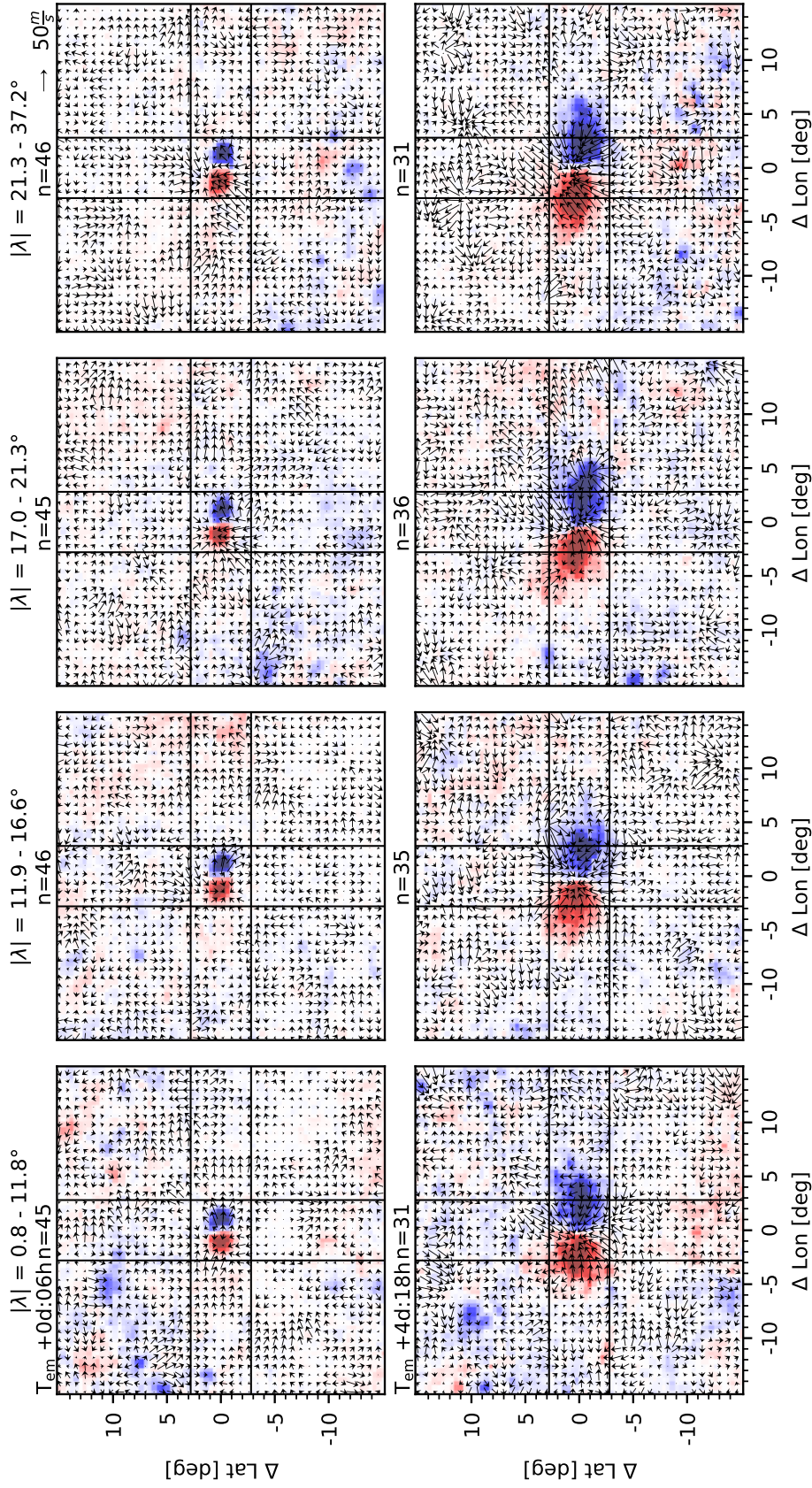
Figure 2.5: Evolution (*from top to bottom*) of the averaged active region magnetic field and flows for the four subsample averages of unsigned latitude |λ| (with |λ| increasing *from left to right*, cf. right panel of Fig. 2.3). The labels, color scales, and arrow scales are the same as in Fig. 2.4. The diverging flow in the bottom row of the third subsample is due to a strong moat flow in AR 11158, which is the largest AR in this subsample at this time.

2.4.3   Flows averaged over the full sample as a function of time

While the sections above outline the evolution of the flows in subsamples of active regions with respect to flux and latitude, we wish to set this into the context of the average EAR over the whole sample. Appendix 2.6.5 provides additional plots of the average flows around the time of emergence as well as averages in longitude covering the leading and trailing polarity separately. Overall, the full ensemble average again exhibits converging flows starting one day prior to emergence. The inflows have a maximum extent of about 7° from the center of the AR, in the time between emergence and seven days after emergence, and amplitudes of about $50\,\mathrm{m\,s^{-1}}$ at a noise level of about $5\,\mathrm{m\,s^{-1}}$.

2.4.4   Quantitative model of the inflows as a function of time and magnetic flux

We wish to describe the inflows around active regions quantitatively and to evaluate the differences found in the flux-binned subsamples (Sect. 2.4.1). To do this, we fit a model to the flows. The main contribution of the inflows is along the latitudinal axis. We therefore averaged the latitudinal flows over the central 5.6° in longitude for each time step and each subsample. This range was chosen to cover a large part of the AR but excludes most of the moat flow signature that is present in the high-flux subsamples. We did not attempt to fit a separate model to the moat flow because the sunspots and with them the moat flow in the individual active regions form at different times relative to the time of emergence, and in some cases break up before the end of the observations (cf. the lower panels for the second-highest flux subsample in Fig. 2.4).

The model we applied consists of the sum of up to two 1D Gaussians with positive or negative amplitude A, position μ, and width σ. As an estimate of the background noise, we computed the standard deviation over the same 5.6° in longitude for subsamples of the control regions corresponding to the AR subsamples. If the amplitude of a fitted Gaussian was smaller than 1.3 times the noise, it was discarded. The converging flows before emergence tend to be less spatially extended than the inflows after emergence. We therefore confined the region of the fits before emergence to about 2° in latitude to avoid fitting large supergranules.

To estimate realistic errors on the fit parameters, we added the model fit to the control region frames and reran the model fitting on these frames. The control region flow maps have the same properties (spatial scale, amplitude) as the active region flow maps and provide a background noise that is uncorrelated with the background in the active region maps. Averaging over all realizations of this procedure and taking the standard deviation of each parameter from these realizations yields an error estimate for the model parameters. Of the 30 time steps of the control region subsamples, the first and last five were not used because of their proximity to the limb, which would artificially increase the noise. Thus, for each model fit, there are $4 \times 20 = 80$ realizations that contribute to the error estimate. Figure 2.6 shows an example of the model fit. The calculated errors (dashed blue lines) are on the same order as the noise in the data (gray shaded region).

Figure 2.7 shows the fit parameters A, μ and σ of v_{lat} averaged over longitudes for the four flux-binned subsamples in the time range between one day before and six days after emergence (the last time step is left out because the signal-to-noise ratio is low). For the
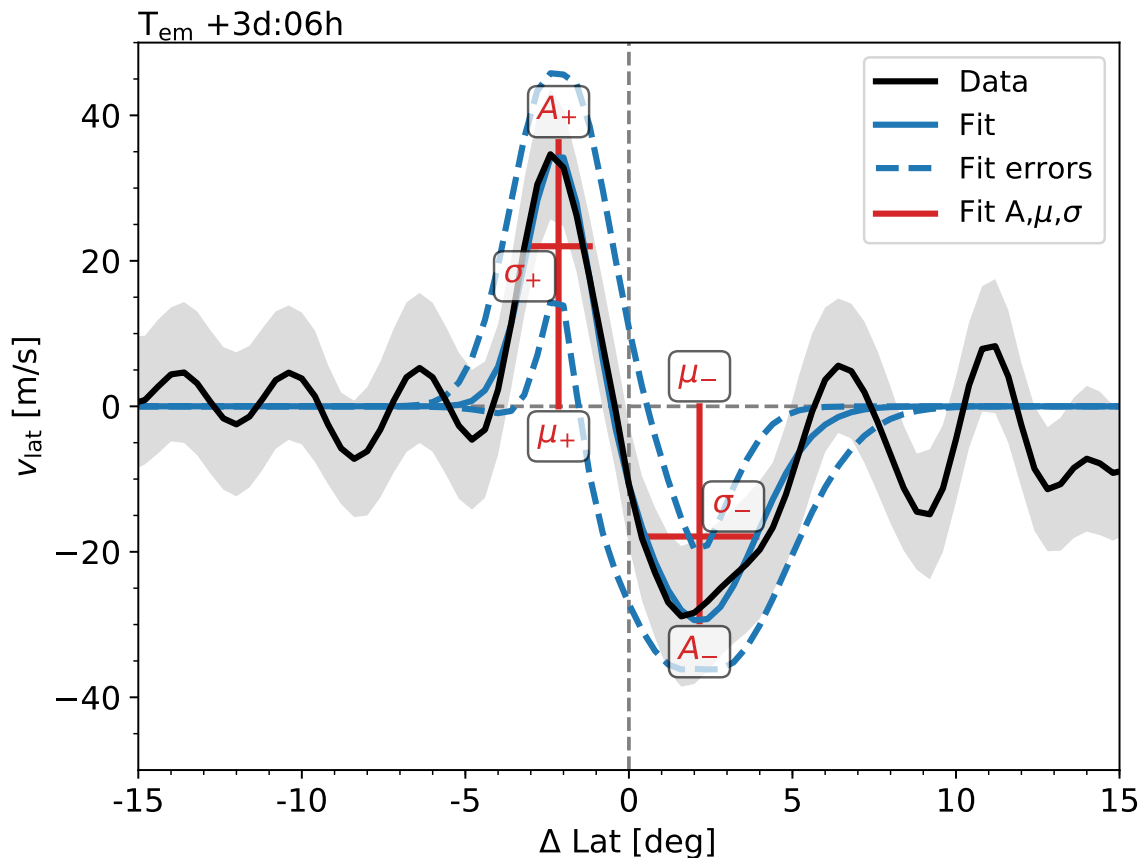
Figure 2.6: Data and model fit of a time step of the second-highest flux subsample ($\langle\Phi\rangle = 7.0 \times 10^{21}$ Mx). The black line shows the latitudinal flow, averaged over longitudes in the range indicated in Fig. 2.4. The solid blue line shows the model fit of two Gaussians with opposite polarity (see text for details). The dashed blue lines show the 1σ error estimates of the fit. The red markings indicate the fit parameters of the amplitude A (in m s^{-1}), the peak position μ (relative to the center of the active region along latitude, Δ Lat), and the standard deviation σ (in degree) of the two Gaussians. The gray shaded region indicates the rms of the flow data. The fit parameters of the two Gaussians slightly deviate from the fitted curve due to superposition; this is small compared to the error, however.

three higher-flux subsamples, the converging flows of the pre-emergence phase vanish shortly after emergence, such that there is no successful fit. After some days, the inflows set in. We defined the onset time of the inflows as the time when the model fits start to be continuously successful. The amplitudes increase from this time on, starting from less than 20 m s^{-1} and reaching maximum velocities of 50–60 m s^{-1} in all cases. In the case of the lowest-flux subsample, where there is no gap in the model fits, we defined the onset time as the time when the amplitude of the fits starts to increase, similar to the other subsamples.

To verify that the moat flow does not affect these measurements, we performed the same analysis again, excluding those pixels from the fit that lie within the area of the moat flow for more than half of the ARs in the respective subsample. We approximated the moat flow area as regions of 2° surrounding positions with reduced continuum intensity (see Sect. 2.3.4 and Appendix 2.6.2). This procedure leaves the model fits and onset times unaffected, except for the positive-value Gaussian in the highest-flux subsample, where
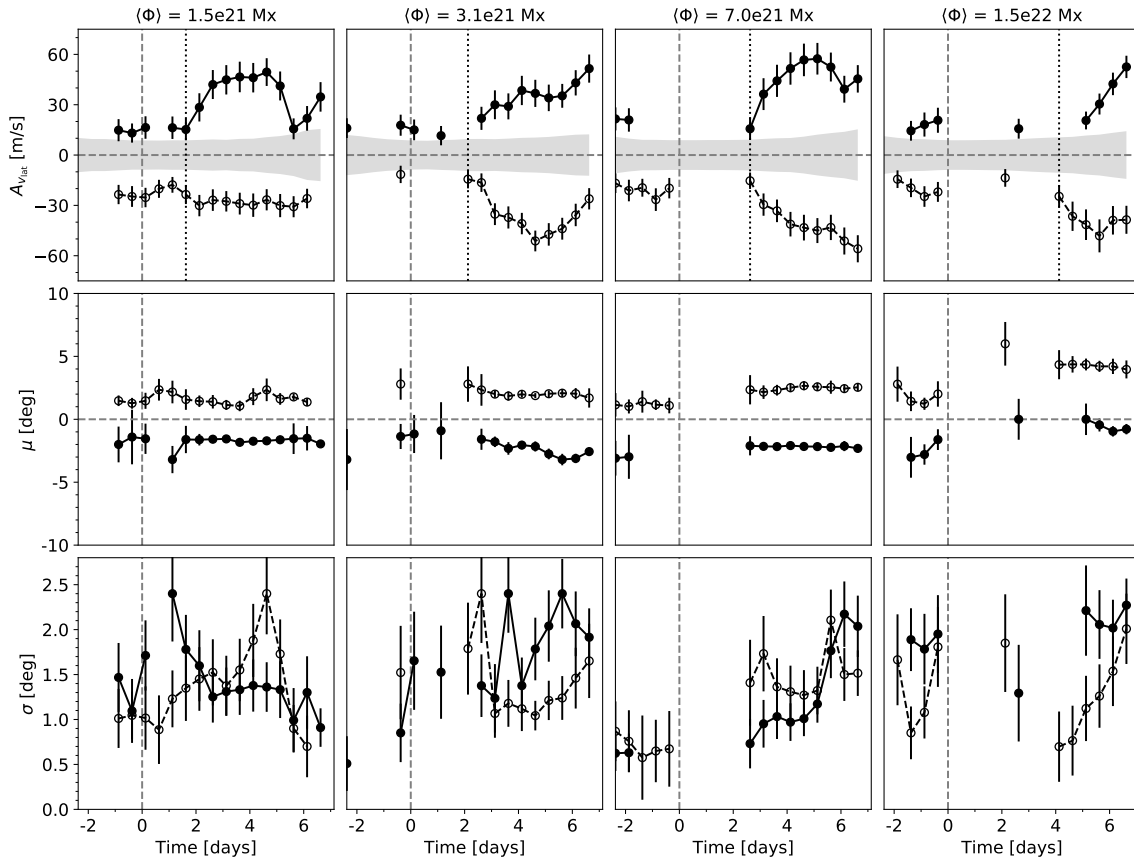
Figure 2.7: Parameters of the best-fit Gaussians to the longitudinally averaged latitudinal flow (see Fig. 2.6). The *top row* shows the amplitudes A_+ and A_-, the *middle row* shows the peak positions μ_+ and μ_-, and the *bottom row* shows the standard deviations σ_+ and σ_- of the model fits (cf. Fig. 2.6). The four columns show the averages over different ranges of flux, with flux increasing from left to right. The error bars are Monte Carlo estimates using quiet-Sun control regions as background noise. No model was fit when there were no inflow signatures above the noise level (see text). The filled dots (circles) and solid (dashed) lines indicate poleward (equatorward) velocity. The dotted black lines indicate the onset time of the latitudinal flow for each subsample. The gray shaded region indicates the rms in the quiet-Sun control regions.

Figure 2.8: Flow onset times in relation to mean flux. The gray boxes indicate the flux ranges of the subsamples. The plot is truncated at 2×10^{22} Mx; the range for the highest-flux subsample continues to 4.8×10^{22} Mx.
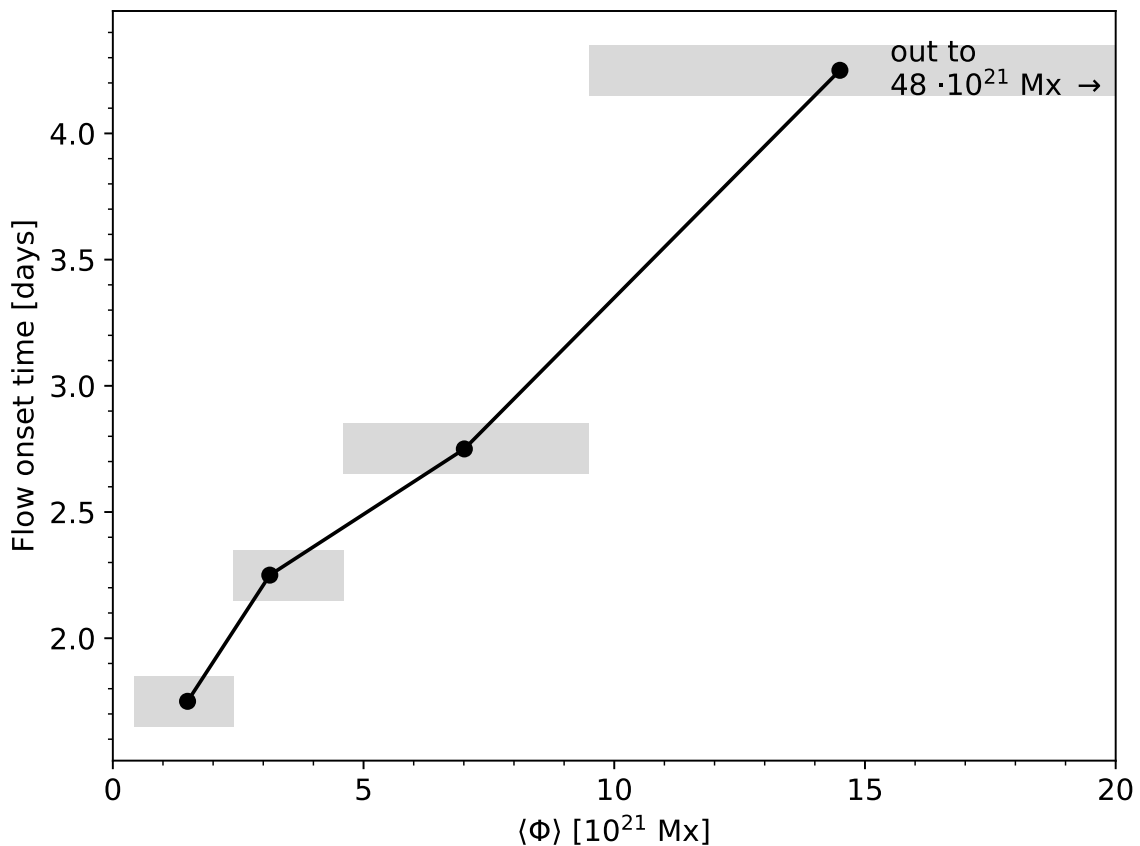
only that part of the inflow that lies outside of the central region was fit, resulting in reduced amplitude and width of the fit.

The onset times illustrate what we discussed qualitatively in Sect. 2.4.1: The inflows towards the center of the active region set in at increasingly later times for an increasing amount of flux of the AR, in the range between one and four days after emergence. Figure 2.8 shows the onset time against the mean flux of each subsample. We point out that the subsamples differ substantially in flux range (cf. left panel of Fig. 2.4).

We measured the extent of the inflows from the models as the peak position μ added to the half-width at half-maximum (HWHM) of the fit. With this, we find inflow extents of about 5–7° with an error of about 1°. After five days, the inflows around the lowest-flux subsample decrease in width and amplitude. For the other subsamples, the fits illustrate that the flows have not reached steady state at the end of the observed time period, especially for the highest-flux subsample, where the inflows after emergence only formed two days before the end of the observational period.

2.5 Discussion

We investigated the evolution of surface flows associated with active regions before, during, and up to six days after their emergence to the surface, using LCT of granulation on the HEAR survey of 182 emerging active regions. We tested the processing of the flow measurements with synthetic input data and by cross-correlation with independent measurements from direct Doppler images.

About half of the active regions in the sample develop a sunspot with a clear penumbra in the observed period. These regions show moat flow structures with velocities on the order of $150 \, \mathrm{m \, s^{-1}}$ in the prograde and equator- and poleward direction.

To study the evolution of the inflows around active regions, we carried out ensemble averages in subsamples ordered by total unsigned magnetic flux and unsigned latitude of the active regions as well as an average over all regions. We then fit a model to the latitudinal flow component in the subsamples ordered by flux.

We find that AR emergence is preceded by converging flows of around 20–$30 \, \mathrm{m \, s^{-1}}$, beginning one day before emergence. This agrees with results reported by Birch et al. (2019), and holds for all ARs in our sample, that is, it is independent of the maximum flux or the latitude of the AR. However, the extent of these early inflows is larger for stronger ARs.

We find that these pre-emergence converging flows cease shortly after emergence. Larger-scale latitudinal inflows form in the days following emergence. The time at which they form depends on the flux of the AR, between about one and four days, and increases with flux. There are several possibilities for the cause of this effect: It could be related to the separation speed of the polarities. Schunker et al. (2019) identified different phases of emergence with respect to the separation speed, finding that on average over all ARs in the HEAR sample, the separation stops increasing at $2.5 - 3$ days after emergence. However, the distinction they made between regions with flux higher or lower than the median value indicates that this time also depends on the flux. It is therefore possible that the onset of the inflow coincides with the end of the separation increase. Another possibility is that it could depend on the relative amount of emerged flux, such that the inflows set in at a certain time relative to the peak flux. It could also depend on the ratio of flux within sunspots versus flux within plage because the proposed mechanism for driving the inflows depends on the plage (Spruit 2003). Further investigation is necessary to clarify this.

Our ensemble averages show a maximum extent of the inflows of around $7°$, which is somewhat smaller than the $10°$ reported recently by Braun (2019). Typical velocities during the later stages are about $50 \, \mathrm{m \, s^{-1}}$, which is at the high end of previously reported velocities (Gizon et al. 2001; Haber et al. 2004; Löptien et al. 2017; Braun 2019). This is in part attributable to differences in spatial resolution; with lower resolution (e.g., by spatial smoothing with a broader Gaussian), the inflows would have lower amplitudes and larger extents. Moreover, our sample consists of emerging active regions, whereas previous studies analyzed well-established, long-lived active regions.

Our measurements of the flows show that they are still evolving at the end of the observed time frame. Observations covering the transition to steady state are needed to shed more light on the physical context of the flows. Because the observation of the emergence is necessary for an accurate age determination of an active region, the limitation to seven days before and after emergence is a constraint that at present is difficult to

circumvent. One possibility is to add observations from different heliographic longitudes, from the recently launched Solar Orbiter, for example, which increases the time that an active region can be tracked continuously. Another option is to track the ARs from the HEAR sample to the next rotation. This is limited to the very long lived regions, however, and leaves an observational gap of more than two weeks.

Acknowledgements

2.6   Appendix

2.6.1   Test of the effect of Zernike subtraction on the flow features

We wished to test the effect that the processing applied to the data (Sect. 2.3.1), specifically the subtraction of the fitted Zernike polynomials Z_n^m, has on flows resembling the inflows toward active regions that we investigate. To do this, we constructed synthetic flow maps, fit the Zernike polynomials to these maps, and subtracted the Fourier-filtered components of the fitted Zernike time series. This was done in the same way as for the actual LCT data. We created one Carrington rotation of synthetic data, with frames set 30 min apart, by rotating the grid 0.272 degrees from one time step to the next. This corresponds to a rotation period of 27.5735 days.

To create the data, we imposed synthetic flows on a Plate Carree coordinate grid (longitude, latitude) of size 450 x 450 with a grid spacing of 0.4°. B angle B_0 and P angle Φ_0 were assumed to be zero for the sake of simplicity. As a model for the flows, we used 2D Gaussian derivatives in the longitudinal direction (for the longitudinal flow component) and in the latitudinal direction (for the latitudinal flow component). We created two different setups, a periodic case and a random case. In the periodic case, the flows were equally distributed on a grid along the equator and the central meridian. In the random case, the flows were distributed randomly within ±45° latitude. The peak velocity of the flow features was $50\,\mathrm{m\,s^{-1}}$ in all cases. We ran two different cases for the periodic and the random setup, with widths of the flow features of approximately 8 and 12° (which is where the velocities drop below $20\,\mathrm{m\,s^{-1}}$). In addition, we ran the same tests with additional moat flows imposed on the synthetic inflows, which are realized as Gaussians with widths of

1.2° and peak velocities of $500\,\mathrm{m\,s^{-1}}$. This was done to test whether the small-scale moat flow introduces additional deviations or leaking into the inflows.

First, we transformed the velocities of the flow maps from $\mathrm{m\,s^{-1}}$ to $\mathrm{pixel\,s^{-1}}$. This was done by inverting the equations given in the Appendix C of Löptien et al. (2017),

$$v_n = \frac{c_{11}v_\theta - c_{21}v_\phi}{c_{11}c_{22} - c_{12}c_{21}}, \tag{2.1}$$

$$v_m = \frac{c_{12}v_\theta - c_{22}v_\phi}{-c_{11}c_{22} + c_{12}c_{21}}, \tag{2.2}$$

where we followed the definitions and nomenclature of Löptien et al. (2017). We then mapped the Plate Carree coordinate grid (longitude, latitude) to a CCD coordinate grid (x, y) of size 1024 x 1024 grid points, which is the effective size that the processing pipeline uses for the HMI data. The projection was made using the transformation specified by *sphere2img()* from the Stanford ring-diagram pipeline (Bogart et al. 2011a).

We fit the Zernike polynomials, Fourier-filtered them, and subtracted them from the data. Then, we remapped from the CCD back to the Plate Carree projection. This was done using the transformation specified by *img2sphere()* from the Stanford ring-diagram pipeline (Bogart et al. 2011a). The last step was to retransform the velocities from $\mathrm{pixel\,s^{-1}}$ to $\mathrm{m\,s^{-1}}$ by applying the equations from Löptien et al. (2017).

Figure 2.9 shows the first time step of the random test case with inflow extents of about 12° before and after subtraction. The lower panels show cuts through the maps for v_{lon} and v_{lat}. Toward the observation limb at 60°, deviations from the synthetic data are noticeable, with velocities below $5\,\mathrm{m\,s^{-1}}$. The shape and extent of the flows are unaltered by the processing. The peak velocities are changed by less than 10 %. The tests including moat flows showed no artifacts in addition to this.

2.6.2   Comparison to flows from direct Doppler images

We compared the velocities obtained by LCT with those of direct Doppler images on an example active region. Comparisons of flows from helioseismic measurements to Doppler data were carried out by Gizon et al. (2000), Jackiewicz et al. (2008), and Švanda et al. (2013), for example. For the comparison, we transformed the LCT flow maps from $(v_{\mathrm{lon}}, v_{\mathrm{lat}})$ to the line-of-sight (LOS) component. Roudier et al. (2013) applied similar transformations to calculate the spherical components from x-, y-, and Doppler components. We point out that the conventions used in our derivation below differ from those used by Roudier et al. (2013).

2.6.2.1   Projection of LCT to the line of sight

We used a right-handed system in which x points toward the observer and z toward solar north. In this system, latitude λ is defined between $[-90 : 90]$ and longitude φ is defined between $[0 : 360)$. Disk center is thus at $\lambda = 0°, \varphi = 0°$ (when the B angle $B_0 = 0°$). The basis vectors of this system are

$$\boldsymbol{e_r} = \begin{pmatrix} \cos(\lambda)\cos(\varphi) \\ \cos(\lambda)\sin(\varphi) \\ \sin(\lambda) \end{pmatrix}, \boldsymbol{e_\lambda} = \begin{pmatrix} -\sin(\lambda)\cos(\varphi) \\ -\sin(\lambda)\sin(\varphi) \\ \cos(\lambda) \end{pmatrix}, \boldsymbol{e_\varphi} = \begin{pmatrix} -\sin(\varphi) \\ \cos(\varphi) \\ 0 \end{pmatrix}. \tag{2.3}$$
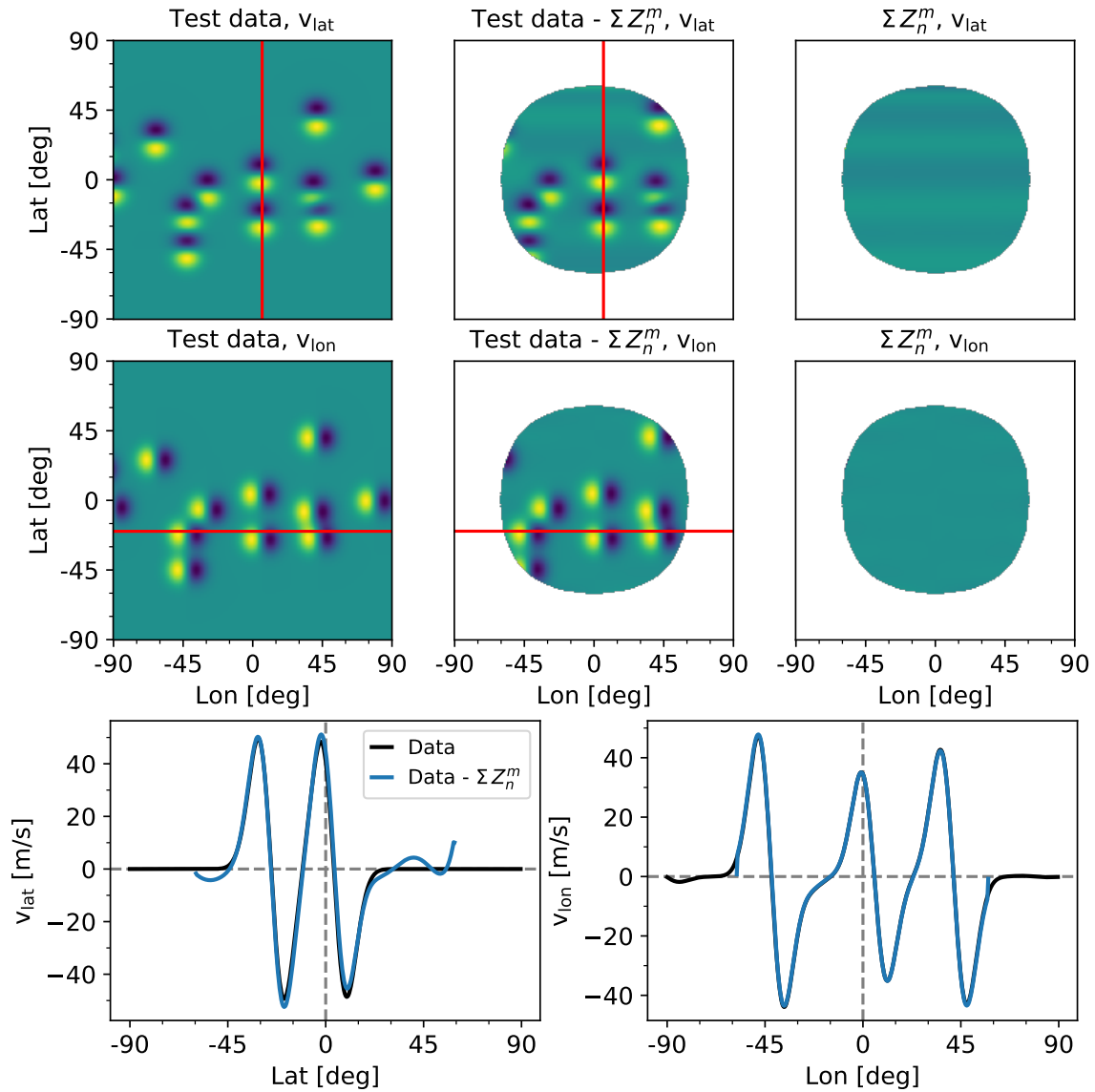
Figure 2.9: Example time step of the test with synthetic data. *Top panel, left column*: synthetic flow map in Plate Carree coordinates for v_{lat} (*top*) and v_{lon} (*bottom*). *Middle*: after subtracting the Zernike fits Z_n^m and limiting the field of view to 60° from disk center. *Right*: sum over the Zernike fits. The red lines indicate the positions of the line plots in the bottom panel. *Bottom panel*: line plots showing the synthetic data before (black) and after (blue) subtraction of the Zernike fits for v_{lat}(*left*) and v_{lon}(*right*).

The transformation between Cartesian and spherical coordinates follows as

$$
\begin{pmatrix} e_x \\ e_y \\ e_z \end{pmatrix} = \begin{pmatrix} \cos(\lambda)\cos(\varphi) & -\sin(\lambda)\cos(\varphi) & -\sin(\varphi) \\ \cos(\lambda)\sin(\varphi) & -\sin(\lambda)\sin(\varphi) & \cos(\varphi) \\ \sin(\lambda) & \cos(\lambda) & 0 \end{pmatrix} \begin{pmatrix} e_r \\ e_\lambda \\ e_\varphi \end{pmatrix}. \tag{2.4}
$$

In addition, the rotation due to the changing B angle B_0 has to be corrected for. This is a rotation around the y-axis. Thus

$$
\begin{pmatrix} e_x \\ e_y \\ e_z \end{pmatrix} = \begin{pmatrix} \cos(B_0) & 0 & \sin(B_0) \\ 0 & 1 & 0 \\ -\sin(B_0) & 0 & \cos(B_0) \end{pmatrix}
$$
$$
\times \begin{pmatrix} \cos(\lambda)\cos(\varphi) & -\sin(\lambda)\cos(\varphi) & -\sin(\varphi) \\ \cos(\lambda)\sin(\varphi) & -\sin(\lambda)\sin(\varphi) & \cos(\varphi) \\ \sin(\lambda) & \cos(\lambda) & 0 \end{pmatrix} \begin{pmatrix} e_r \\ e_\lambda \\ e_\varphi \end{pmatrix}. \tag{2.5}
$$

With LCT, we only have information on e_λ and e_φ, and the radial component e_r is assumed to be zero. Thus, projecting the LCT velocity vectors onto the line of sight e_x follows the expression

$$
e_x = (-\sin(\lambda)\cos(\varphi)\cos(B_0) + \cos(\lambda)\sin(B_0))\, e_\lambda
$$
$$
+ (-\sin(\varphi)\cos(B_0))\, e_\varphi. \tag{2.6}
$$

2.6.2.2   Data reduction of Doppler and line-of-sight data

To compare the Doppler images to the line-of-sight projected LCT velocity images, large-scale systematics depending on disk position need to be removed. In addition, the data sets need to share a common frame of reference as well as temporal and spatial resolution.

First, we applied the same mapping procedure as was used for the magnetograms and the intensity maps to the full-disk Dopplergrams from hmi.v_720s. This creates a Plate Carree mapped cube for each EAR, with frames of $60° \times 60°$ and a grid spacing of $0.1°$. The cubes were centered on the coordinate specified in Schunker et al. (2016) and cover the time period between the start and end time provided in the HEAR survey. In this step, we also subtracted the background signal that stems from solar rotation, which was taken from averages over one-third of a Carrington rotation (hmi.v_avg120). Each image was subtracted by the first average frame whose central time as specified by the MidTime keyword lies after the observation time as specified by the T_REC keyword.

In addition to solar rotation, the observer motion in radial direction has to be corrected for. This was done by subtracting the velocity specified by the frame OBS_VR keyword for each frame.

Next, we averaged in time over one day relative to the time of emergence and applied Gaussian smoothing of $\sigma = 0.4°$. We then resampled the grid spacing of the map from $0.1°$ to the $0.4°$ of the LCT velocity maps.

The convention for the sign of the HMI Dopplergrams is positive for movement away from the observer (redshift) and negative for movement toward the observer (blueshift). This is opposite to the convention used in the transformation in Sect. 2.6.2.1, where the x-axis points toward the observer. The sign of the Dopplergrams is therefore flipped for the further analysis.
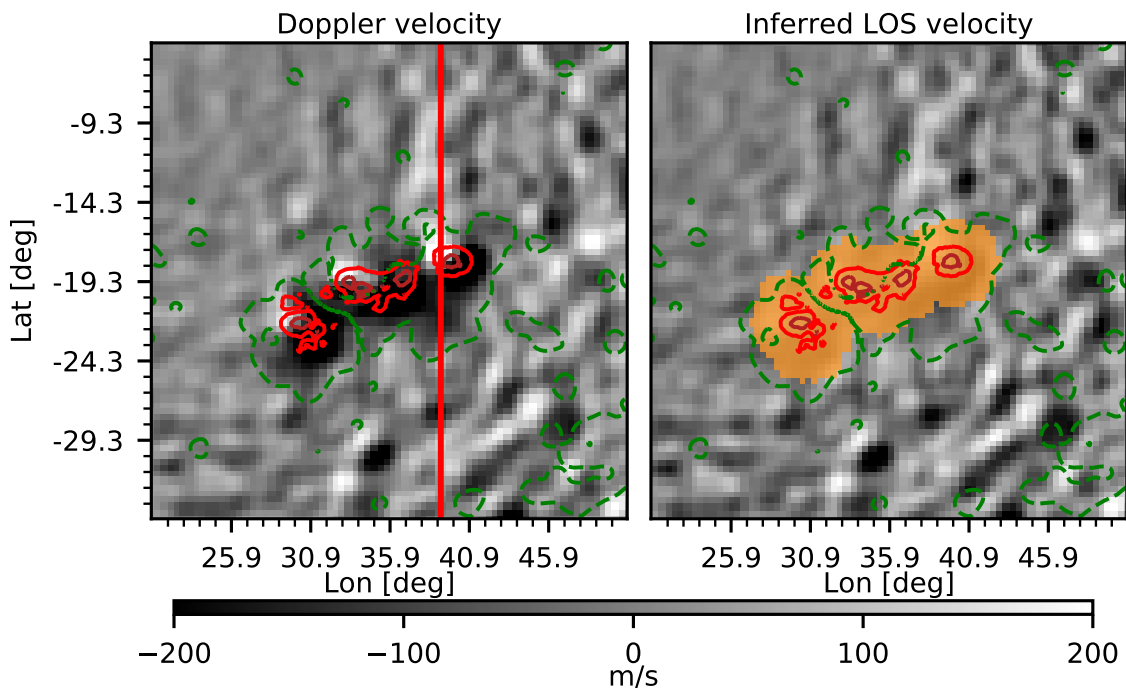
Figure 2.10: Comparison of Doppler velocity (*left panel*) and line-of-sight projected LCT velocity (*right panel*). The green contours outline the absolute radial magnetic field at 10 Gauss. The dark and bright red contours indicate the umbral and penumbral boundary, respectively. The orange shaded region in the right panel indicates the region that is excluded in the following (see text for details). The red line in the left panel indicates the position of the line plot in Fig. 2.11. The axis labels are in Carrington coordinates. The center of the maps is approximately 23° from disk center, which is in the direction toward the upper left corner.

2.6.2.3   Results

Figure 2.10 shows the comparison of a Doppler map and the corresponding line-of-sight projected LCT map for AR 11158. The maps are averages over 24 h, starting four days after the time of emergence.

Figure 2.11 shows a cut along the red line in Fig. 2.10. Figure 2.12 shows a density plot of the two velocities. We fit a line through the data for the relation between the Doppler and the LOS data. Because both are subject to error, we performed the fit with orthogonal distance regression (ODR), with the standard error of the 24-hour time averages as errors. The errors close to disk center are about $15 \, \mathrm{m \, s^{-1}}$ for the Doppler frames and $5 \, \mathrm{m \, s^{-1}}$ for the LOS frames, and they increase outward to $40 \, \mathrm{m \, s^{-1}}$ and $60 \, \mathrm{m \, s^{-1}}$, respectively. These are rough estimates because the individual frames are correlated. We also computed the correlation between the two flow measurements.

The comparison (Figs. 2.10, 2.12, and 2.11) illustrates that the Doppler velocity and the LOS velocity inferred from LCT agree well, except in the presence of a strong magnetic field. Here, velocities from LCT are lower than the Doppler velocities. This has several reasons: LCT is known to underestimate velocities at a strong magnetic field (Fisher and Welsch 2008; Löptien et al. 2017). A strong magnetic field suppresses convective blueshift,
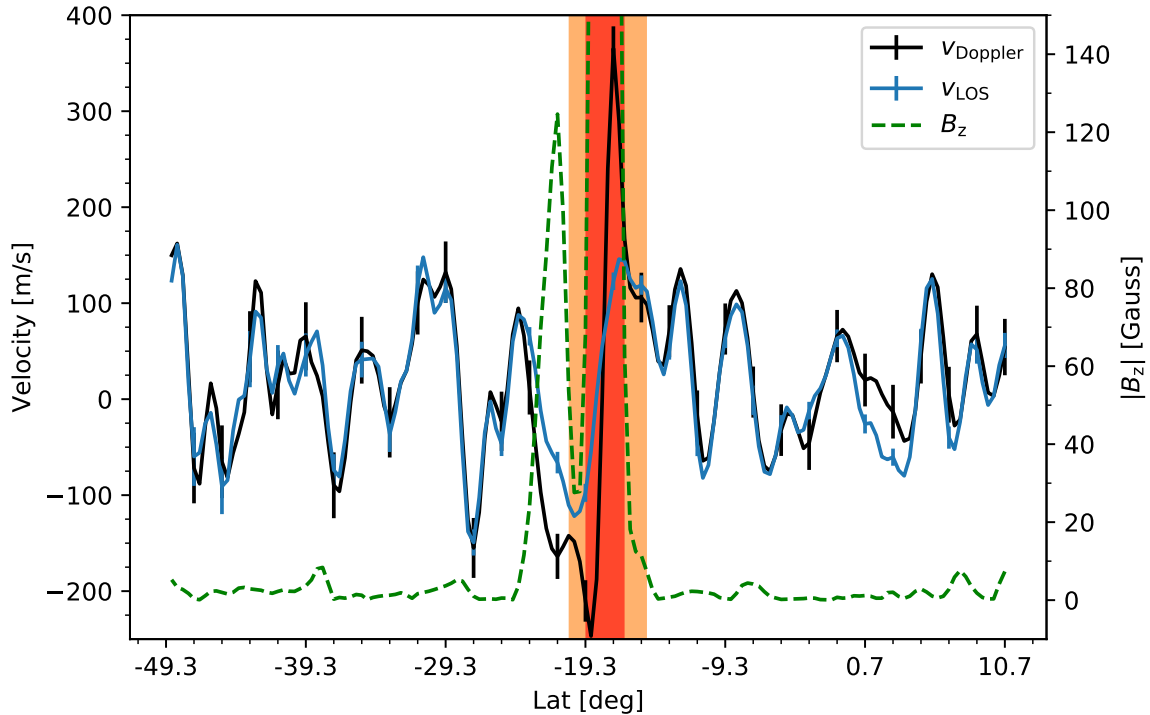
Figure 2.11: Plot along the red line indicated in Fig. 2.10. The black and blue lines indicate the velocity measurements from Doppler and line of sight, respectively. The error bars indicate the standard error of the average. The dashed green line indicates the radial magnetic field strength. The red and orange shaded regions correspond to the red and orange regions in Fig. 2.10.

which results in a redshift signature in the Doppler maps (Stix 2002). Furthermore, the two measurements are taken at different depths (Jackiewicz et al. 2008).

When regions of 2° are excluded around positions where the LCT flows are excluded due to reduced or increased continuum intensity (see Sect. 2.3.4), the systematic outliers are ruled out and the slope of the fit between the Doppler and the inferred line-of-sight velocities is closer to 1 (cf. Fig. 2.12). The correlations between the Doppler and the LOS velocities are between 0.7 and 0.9 for all observed one-day averages.

The intercept of the fit is in the range of -11 to $-16\,\mathrm{m\,s^{-1}}$ for all one-day averages, meaning that the line-of-sight velocities are systematically lower than the Doppler velocities (i.e., the Doppler velocities have a preference toward upflows at disk center). Because the projection onto the line of sight only takes into account v_{lon} and v_{lat}, the line-of-sight velocity is necessarily zero at disk center, whereas the Doppler velocity is sensitive to any motion along the line of sight, including radial motions. Several studies have investigated the rms velocity of Doppler images at disk center and the radial velocity of supergranulation, and reported velocities between $5\,\mathrm{m\,s^{-1}}$ and $15\,\mathrm{m\,s^{-1}}$ (Giovanelli 1980; Hathaway et al. 2002; Duvall and Birch 2010). Our findings are in accordance with this.
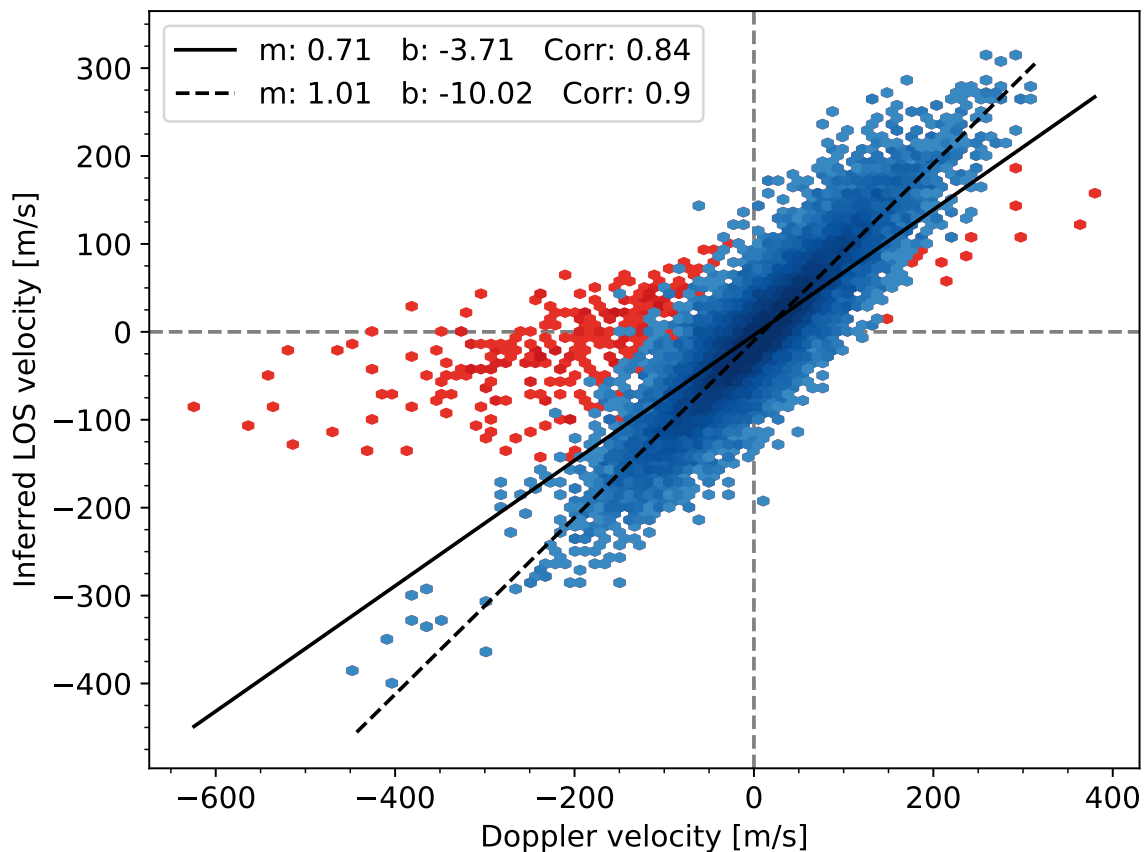
Figure 2.12: Density plot of the velocity data in Fig. 2.10. The red shaded dots indicate all pixels, the blue shaded dots only those outside of the orange shaded region in Fig. 2.10. The continuous (dashed) line indicates the fit to the full (magnetic-field-filtered) sample, respectively. The legend provides the fit parameters for both fits as well as the correlations between the measurements.

2.6.3 Comparison of methods for measuring the positions of the AR

We compared the two different methods that were used to measure the positions of the polarities of the active regions (cf. Sect. 2.3.2). Figure 2.13 shows two example active regions.

2.6.4 Effect of moat flows

We wished to identify the presence of moat flows in the flow data on our sample of active regions. To do this, we classified time series of six-hour averages of each active region in the sample according to the presence of a sunspot with a clear penumbra, which would potentially host a moat flow. We then performed an ensemble average on the resulting subsamples to identify the moat flow signature. The classification was made with the procedure described below.

We cropped the normalized continuum intensity frames and the magnetograms to the inner $12° \times 12°$ around the position of the leading polarity. We then created a mask of all pixels where the absolute radial field $|B_z|$ is below $10\,\mathrm{Gauss}$ and applied that mask to
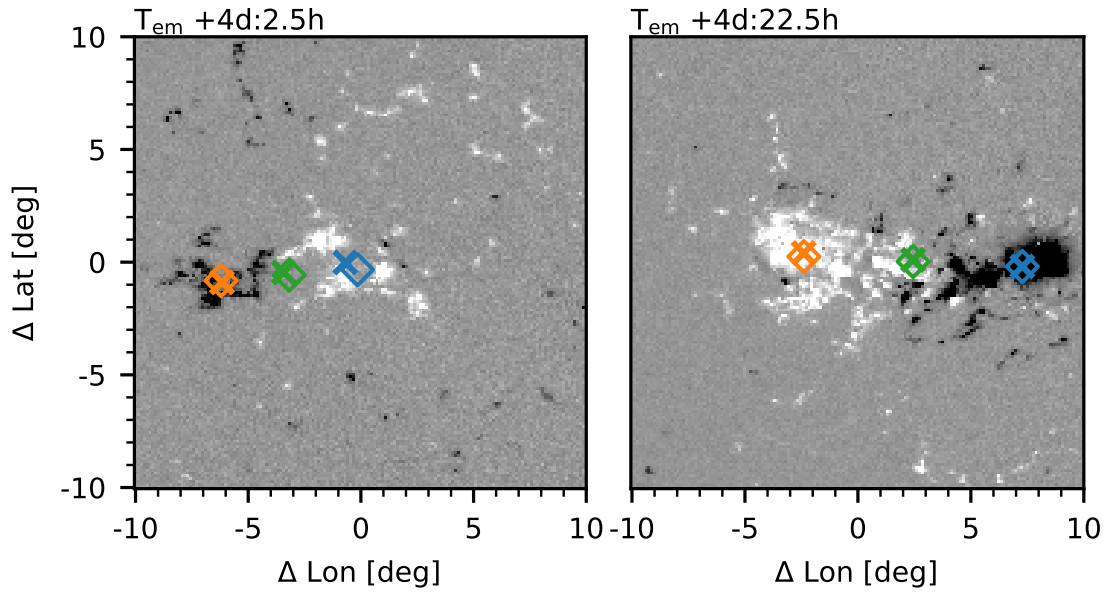
Figure 2.13: Comparisons of the two position-finding methods on AR 11310 (*left*) and AR 11640 (*right*). The blue, orange, and green symbols mark the position of the leading and trailing polarity and the center of the AR, respectively. The crosses and diamonds refer to coordinates derived with the method described in Sect. 2.3.2 and the method described by Schunker et al. (2019), respectively. The axis labels are relative coordinates provided by the HEAR survey. The background images show the radial field B_z. The gray scale saturates at ± 500 Gauss.

the continuum frame. This was used as the total number of pixels corresponding to the active region. We then counted the number of pixels in the masked normalized continuum intensity frame that fall in bins of below 0.6 (corresponding to umbra), between 0.6 and 0.95 (penumbra), and above 0.95 (no intensity darkening). The threshold at 0.95 is the same as was used to exclude pixels in Sect. 2.3.4, the threshold at 0.6 is a result of testing.

Connected regions of pixels with normalized intensity below 0.6 are identified as umbrae. For the largest region, the total pixel count of umbra and the percentage of penumbra in a box of 2.2° around the center of the umbra were calculated. Each time step was then classified into one of five categories with the following scheme:

A classification of 4 *(no intensity darkening)* was assigned if the total number of pixels in the umbra is zero and the total percentage of pixels in the penumbra, relative to the total number of active region pixels, is lower than 1. A classification of 3 *(small pore)* was assigned if the total number of pixels in the umbra is zero and the total percentage of pixels in the penumbra is higher than 1. A classification of 2 *(large pore, no penumbra)* was assigned if the number of pixels in the umbra of the largest spot is lower than 12 and the percentage of penumbra around this umbra is lower than 20. A classification of 1 *(large pore, with some penumbra)* was assigned if either the number of pixels in the umbra of the largest spot is lower than 12 and the percentage of penumbra around this umbra is higher than 20, or if the number of pixels in the umbra of the largest spot is larger than 12 and the percentage of penumbra around this umbra is lower than 20. A classification of 0 *(clear penumbra)* was assigned if the number of pixels in the umbra of the largest spot is larger than 12 and the percentage of penumbra around this umbra is higher than 20.
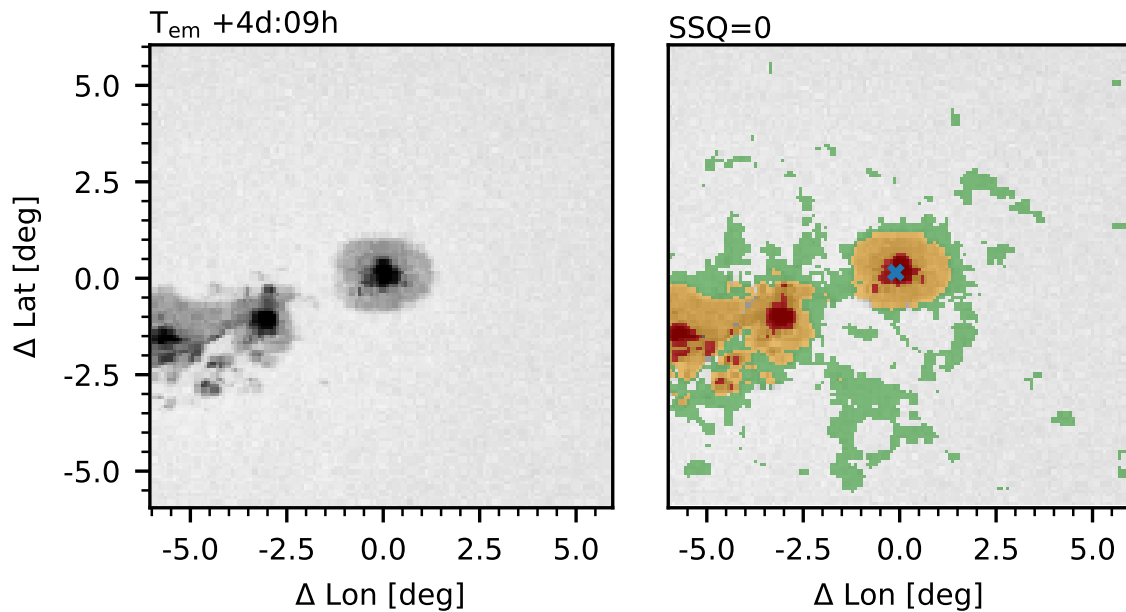
Figure 2.14: Example of the sunspot classification. *Left*: normalized six-hour average continuum map of AR 11158. The axis labels are relative to the center of the leading polarity, as defined in Sect. 2.3.2. *Right*: same as left, with a colored overlay of pixels for which $|B_z|$ is higher than 10 Gauss. Colors indicate no intensity darkening (green), penumbra (yellow), and umbra (red; see text for definition). The blue cross indicates the center of the largest umbral region. The time step shown here has the sunspot classification $SSQ = 0$.

This classification scheme was derived and checked by inspecting several ARs. A table of all time steps between -2 and +7 days for all 182 active regions is available online[1].

Figure 2.14 shows an example of the classification. The colored regions in the right panel indicate pixels with an absolute radial field above 10 Gauss, which we associate in this context with the AR. The small features at large distances from the sunspots do not contribute significantly.

Figure 2.15 shows an example time step for averages over three different sets of data: All 161 active regions for which data are available at this time relative to emergence, only those regions without a sunspot with clear penumbra (classifications of 1,2,3 and 4), and only those regions with a sunspot with clear penumbra (classification of 0). It is apparent that the diverging flow at the leading polarity is connected to the presence of developed sunspots with a clear penumbra, which is consistent with the moat flow. The velocities are about 150 m s^{-1}, which is lower than typical moat flow velocities observed in evolved sunspots. A reason for this could be that the sunspots in our sample are just forming, together with the (in this context) comparatively large grid spacing of 0.4° and additional Gaussian smoothing of $\sigma = 0.8°$ of our flow data, which reduces localized peak velocities.

Furthermore, the moat flow seen here is not symmetric: The westward (i.e., prograde) component is stronger than the eastward (retrograde) component. The components in the north- and southward directions have approximately the same strength as the westward

---

[1] `https://dx.doi.org/10.17617/3.6h`
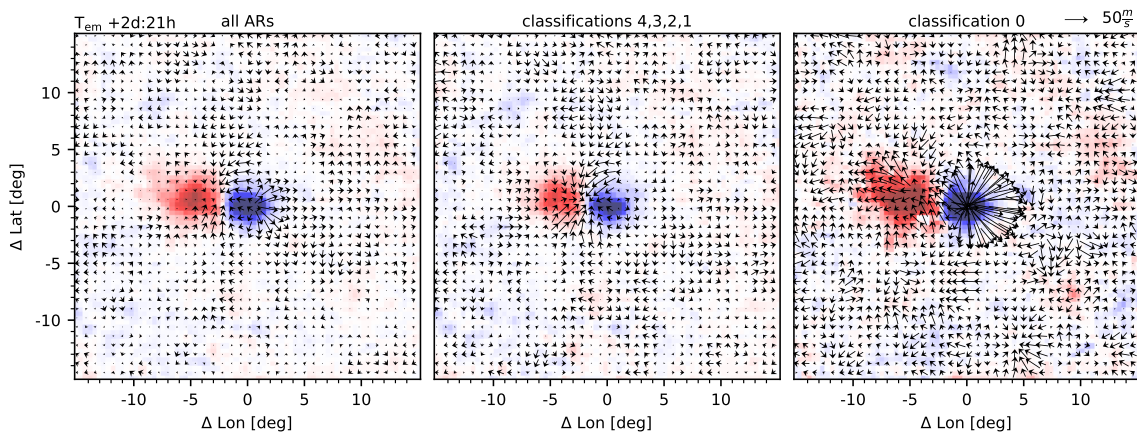
Figure 2.15: Six hour average flow maps, centered at 2 d and 21 h after emergence. The left panel shows the average of 161 active regions, the middle panel shows the average over 119 active regions with no or only partial sunspot presence, and the right panel shows the average over 42 active regions with a sunspot with clear penumbra (corresponding to classification 0, see text). The active regions are averaged relative to the position of their leading polarity. Red (blue) indicates positive (negative) radial magnetic field saturated at ±150 Gauss. The arrows indicate the flows.

component. Švanda et al. (2014) also found an asymmetry between the east- and westward moat flows.

Our findings agree with those of Vargas Domínguez et al. (2008), who showed that moat flows are predominantly present in the directions where there is penumbra. The sunspots in our sample are only just forming, with additional flux joining the sunspot from the emergence site, that is, the retrograde direction. When the accumulation of flux is complete and the penumbra surrounds the umbra in all directions, the moat flows become more symmetric. At later times, however, the number of ARs that host a spot decreases, leading to high background noise.

Figure 2.16: Evolution (from left to right) during the emergence phase of the average active region for the ensemble average over all 182 ARs in the sample. Each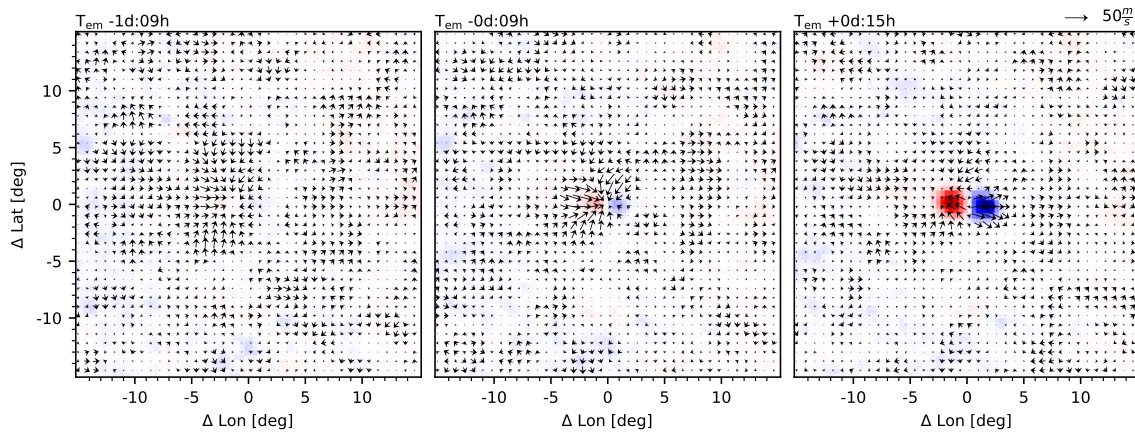 time step is an average over six hours, centered on the labeled time. The flows are smoothed with a Gaussian of $\sigma = 0.8°$. Red (blue) indicates positive (negative) radial magnetic field, saturated at ± 300 Gauss.

2.6.5   Average over all EARs

2.6.5.1   Flows during the time of emergence

We performed an ensemble average over all 182 EARs in the sample to connect to the work of previous studies. In this case, we averaged in time over six hours and applied Gaussian smoothing of $\sigma = 0.8°$ to the flow maps. Figure 2.16 shows the early evolution of flows in several time steps. Starting one day before emergence, a converging flow toward the center of the average EAR is clearly visible, becoming stronger toward the time of emergence. This converging flow is noticeable in all four flux-sorted subsamples (see Sect. 2.4.1) and was found by Birch et al. (2019). During emergence, these flows vanish. At the same time, a prograde flow at the position of the leading polarity forms. This is again consistent with Birch et al. (2019).

2.6.5.2   Flow variation in time, per polarity

Following the method of Braun (2019), we calculated longitudinal averages of the flows. For each polarity, we averaged over 6° from the center of the active region toward east (west) for the trailing (leading) polarity.

Figure 2.17 shows the results for the flows outside of a strong magnetic field. The longitudinal flow components corresponding to time steps from three days onward show the retrograde flow that Braun (2019) detected. For the leading polarity, they span out to a maximum of approximately 7°, with velocities of about $20\,\mathrm{m\,s^{-1}}$. The velocities here are lower than for the flux-binned subsamples in Sec. 2.4.1 because of the different averaging ranges.
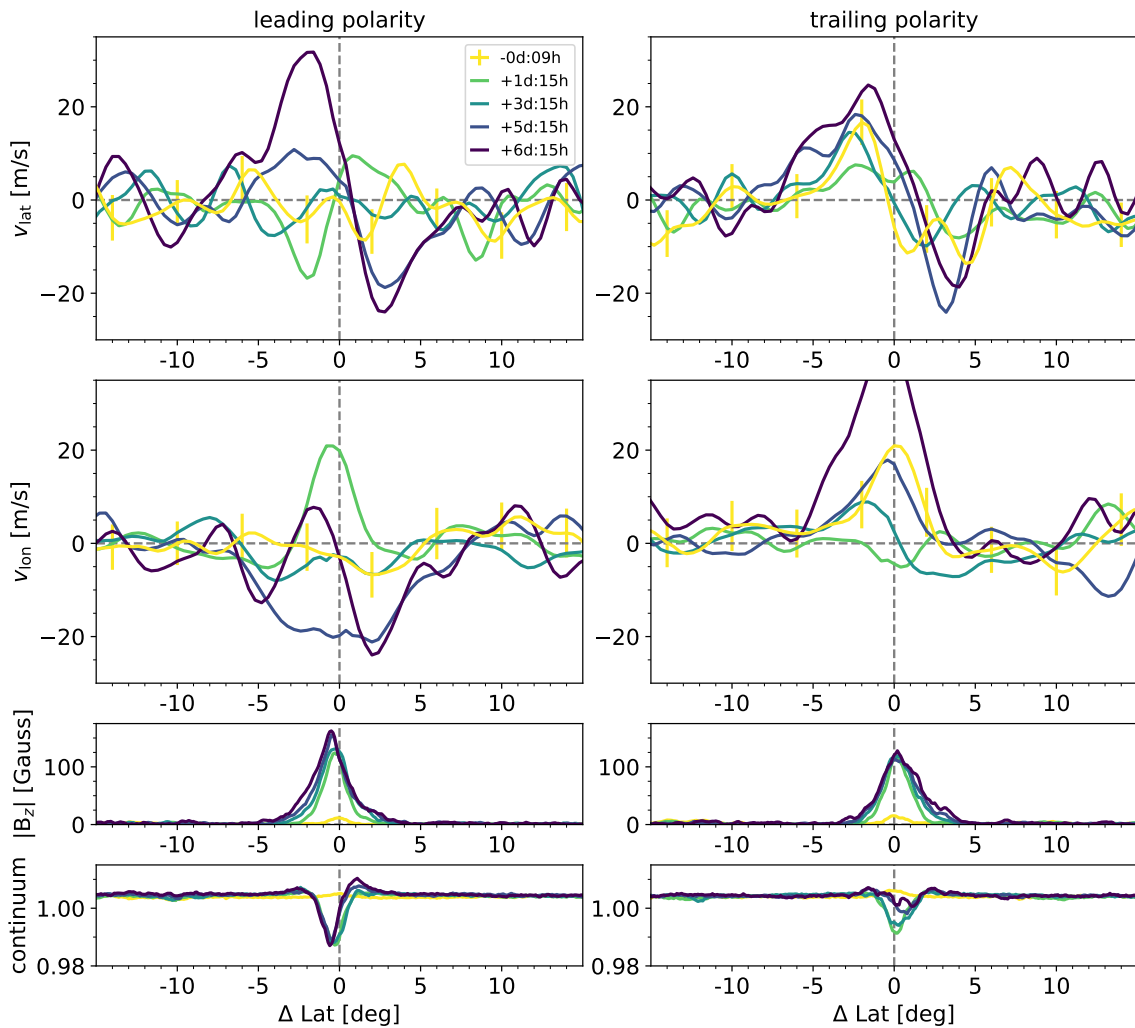
Figure 2.17: Evolution of the flow in a longitudinal band of 6° width for each polarity. *Left (right) column*: leading (trailing) polarity. *first (second) row*: latitudinal (longitudinal) flow component, and the third row shows the absolute value of the radial magnetic field. The fourth row shows the normalized continuum intensity. All data are time-averaged over six hours. The flows are smoothed with a Gaussian of $\sigma = 0.8°$. The curves represent different time steps (see legend).

3 Testing solar surface flux transport models in the first days after active region emergence

Abstract

Context. Active regions (ARs) play an important role in the magnetic dynamics of the Sun. Solar surface flux transport models (SFTMs) are used to describe the evolution of the radial magnetic field at the solar surface. The models are kinematic in the sense that the radial component of the magnetic field behaves as passively advected corks. There is, however, uncertainty about using these models in the early stage of AR evolution, where dynamic effects might be important.

Aims. We aim to test the applicability of SFTMs in the first days after the emergence of ARs by comparing them with observations. The models we employ range from passive evolution to models where the inflows around ARs are included.

Methods. We simulated the evolution of the surface magnetic field of 17 emerging ARs using a local surface flux transport simulation. The regions were selected such that they did not form fully fledged sunspots that exhibit moat flows. The simulation included diffusion and advection by a velocity field, for which we tested different models. For the flow fields, we used observed flows from local correlation tracking of solar granulation, as well as parametrizations of the inflows around ARs based on the gradient of the magnetic field. To evaluate our simulations, we measured the cross correlation between the observed and the simulated magnetic field, as well as the total unsigned flux of the ARs, over time. We also tested the validity of our simulations by varying the starting time relative to the emergence of flux.

Results. We find that the simulations using observed surface flows can reproduce the evolution of the observed magnetic flux. The effect of buffeting the field by supergranulation can be described as a diffusion process. The SFTM is applicable after 90 % of the peak total unsigned flux of the AR has emerged. Diffusivities in the range between $D = 250\text{--}720\,\text{km}^2\,\text{s}^{-1}$ are consistent with the evolution of the AR flux in the first five days after this time. We find that the converging flows around emerging ARs are not important

for the evolution of the total flux of the AR in these first five days; their effect of increasing flux cancellation is balanced by the decrease in flux transport away from the AR.

3.1 Introduction

Active regions (hereafter ARs) are the surface signature of magnetic flux rising from the interior of the Sun. They are the site of eruptive events such as jets and flares, and they play an important role in the solar dynamo.

During the emergence of ARs, their magnetic polarities move apart and develop a tilt angle, with the leading polarity closer to the equator than the trailing polarity (e.g., Schunker et al. 2020, for a review see van Driel-Gesztelyi and Green 2015). This is consistent with the footpoints of the flux being connected to the subsurface field and separating due to the action of magnetic tension and the drag force (Chen et al. 2017; Schunker et al. 2019). Schunker et al. (2019) calculated separation speeds of AR polarities and suggest that during emergence, the magnetic tension and drag force play a stronger role in transporting the magnetic field than diffusion. They also found that the scatter in polarity positions increases with time consistently with buffeting by supergranulation.

Studying the surface magnetic field of ARs helps to understand their evolution and the buildup of the poloidal field in the solar cycle. In addition to the systematic motions from, for example, magnetic tension, the processes on the solar surface that displace magnetic flux are the random motions of convective granulation and supergranulation on smaller scales as well as systematic flows on larger scales, such as differential rotation, the meridional flow, and inflows around ARs. The random convective motions can be treated as a diffusion process (Leighton 1964), which can be implemented in surface flux transport models (SFTMs) as a random walk. Estimates of the diffusion rate D from observations typically indicate $D = 250\,\mathrm{km^2\,s^{-1}}$ (Jafarzadeh et al. 2014), but higher values up to $D = 500\,\mathrm{km^2\,s^{-1}}$ have also been reported (Wang et al. 2002; Yeates 2020).

Inflows on various spatial and temporal scales around evolved ARs have been measured by, for example, Gizon et al. (2001), Haber et al. (2004), Komm et al. (2012), Löptien et al. (2017), and Braun (2019). They span approximately $10°$ from the AR and have velocities of about $50\,\mathrm{m\,s^{-1}}$. It is thought that the inflows may be driven by increased cooling in ARs (Spruit 2003). Cameron and Schüssler (2012) propose these inflows as a possible mechanism for a nonlinearity that regulates the solar cycle strengths in the solar dynamo. Recently, Gottschling et al. (2021) measured the evolution of the flows around emerging ARs from before to up to seven days after emergence, finding that the time between the AR emergence and the time at which inflows set in after the emergence increases with the total magnetic field of the AR. These inflows have velocities of about $50\,\mathrm{m\,s^{-1}}$ as well, but they appear to be smaller in extent than the inflows around evolved ARs. Gottschling et al. (2021) found no strong dependence of the amplitude of these inflows on the field strength of the ARs. The nature of these observed inflows in the first days after emergence is not clear, and their driving mechanism could be different from that of the inflows around evolved ARs. They could be the result of a passive emergence, in which the rising flux is affected by the supergranulation pattern (Birch et al. 2019). Another scenario is that they are driven by the magnetic tension that moves the polarities apart in the first days after emergence, see Cameron et al. (2010) and Schunker et al. (2019). In a three-dimensional

magnetohydrodynamic (MHD) simulation of a rising flux tube in a rotating convection zone, Abbett et al. (2001) also found converging flows.

Several studies have incorporated inflows around ARs in surface flux transport models (De Rosa and Schrijver 2006; Jiang et al. 2010; Cameron and Schüssler 2012; Yeates 2014; Martin-Belda and Cameron 2016, 2017b). Martin-Belda and Cameron (2016) found that the inflows enhance flux cancellation and that they can, in conjunction with differential rotation, produce a net tilt angle. This tilt is, however, too small compared to observed tilt angles. Martin-Belda and Cameron (2017b) investigated the effect on the large-scale field and found that the inflows can lead to a reduction in the axial dipole moment of 30 %. The inclusion of inflows into global SFTMs improves the match to the global dipole for solar cycles 13 to 21 (Cameron and Schüssler 2012), and it can account for the excess strength of the polar field at activity minimum in simulations by effectively reducing the tilt angle of ARs (Cameron et al. 2010; Yeates 2014). However, Yeates (2020) has recently argued that this excess strength can be a result of the bipolar approximation of the ARs. On the other hand, Yeates (2014) found that the incorporation of the inflows (in form of a perturbation of the meridional flow) delays the dipole reversal times for solar cycle 23 with respect to the observed cycle.

The above studies used simple mathematical descriptions as parametrizations of the inflows. They were included either as a perturbation of the meridional flow at active latitudes (Jiang et al. 2010; Cameron and Schüssler 2012; Yeates 2014), or as the gradient of the magnetic field (De Rosa and Schrijver 2006), with a normalization such that the extent and the amplitude of the inflows are similar to the observed values. The latter, however, raised the problem that the flux of an isolated AR got "trapped" by the inflow field due to the inward-directed flows from all sides, such that the flux cannot escape the AR. The flux is pushed into small, long-lived clumps, which are not observed. Part of this effect might however be caused by the flux-dependent diffusion that was used (Martin-Belda and Cameron 2016).

For this study, we used a local surface flux transport model to simulate the evolution of the magnetic field of ARs, and compared it to the observed evolution. For this, we considered a sample of emerging ARs that take several days to cross the visible disk after the bulk of flux has emerged. The simulations include transport by diffusion and by advection due to surface flows. We tested different models for both. For the advection, we used observed flow maps from correlation tracking of solar granules as well as flow parametrizations from the literature, motivated by the resemblance of the observed flows in the first days after emergence with the inflows around ARs.

This paper is structured as follows. In Sect. 3.2, we describe the sample of ARs on which we carried out the flux transport simulation. In Sect. 3.3, we describe the SFTM simulation that we used, as well as the different models of the flow field and the diffusion. Sect. 3.4 presents the results, followed by a discussion in Sect. 3.5.

3.2   Active region sample

We identified ARs that emerge into the quiet Sun and remain on the visible disk for multiple days after their emergence using the Solar Dynamics Observatory Helioseismic Emerging Active Regions (SDO/HEAR) survey (Schunker et al. 2016). The survey consists of

182 emerging ARs that were observed between up to seven days before and after the time of emergence t_0, at which the region reaches 10 % of the maximum total unsigned flux within the first 36 h after first appearance in the NOAA record.

From the 182 ARs in the HEAR survey, we selected those regions that do not develop a fully fledged sunspot with a clear penumbra over the disk passage. Fully fledged spots show moat flow signatures (Sheeley 1972). At the grid scale that we used in our simulation, which is limited by the observed flows (see Sect. 3.3.1), the moat flow spatially overlaps with the magnetic field of the spots. In the simulation, this would lead to a disruption of the spots into ring-like structures, which is inconsistent with observations. The sunspot identification was done with the sunspot quality number from Gottschling et al. (2021), where a sunspot quality of 0 indicates a spot with a clear penumbra. After excluding these regions, 92 ARs are left in the sample.

For a comparison of the observed and the simulated magnetic field, the ARs have to remain on the visible disk for several days after the simulations are initialized. To select suitable ARs, we created data cubes of the line-of-sight magnetic field observed by the Helioseismic and Magnetic Imager onboard the Solar Dynamics Observatory (SDO/HMI, Schou et al. 2012), projected to Plate Carree projection and corrected for the viewing angle μ. The cubes have a field of view of $60° \times 60°$ and a grid spacing of 0.4° in both longitude and latitude, centered on the AR centers as defined in the HEAR survey. The grid spacing is the same as that of the observed flow maps (Sect. 3.3.1). On the temporal axis, the cubes span up to seven days before and after the time of emergence in nonoverlapping twelve-hour averages. We measured the total unsigned flux of each AR as the total unsigned flux in a disk of 5° radius around the center of the AR. From this, we determined the time $t_{90\%}$ at which 90 % of the maximum total unsigned flux of the AR has emerged in the period covered by the HEAR survey. This is in analogy to the definition of the emergence time t_0.

The observed flows have data coverage out to only 60° from disk center, which limits the last last time step t_{last} that can be used in the simulation. We identified t_{last} as the last time step where more than half of the field of view of the observed flow field is within a distance of 60° to the disk center.

For the sample selection, we required that the time between $t_{90\%}$ and t_{last} be at least 5.5 days. This leaves 17 ARs. Appendix 3.6.1 lists all ARs in this sample. Because of the selection criteria (the exclusion of ARs that form fully fledged sunspots, and the requirement of several days of observations after most of the flux has emerged), the selected ARs are relatively weak and short-lived, and they are well into their decaying phase at the end of the observations.

Figure 3.1 shows a few examples of the evolution of the twelve-hour averaged total unsigned flux over time, relative to $t_{90\%}$. In most cases, the peak flux occurs at the time $t_{90\%} + 0.5$ days. The average total unsigned flux over the sample of ARs at that time is 1.65×10^{21} Mx, with a standard deviation of 0.66×10^{21} Mx.

3.3   Cork simulation for local surface flux transport

For the local flux transport simulation, we adapted the cork simulation of Langfellner et al. (2018). The simulation treats the magnetic field from an initial input magnetogram as individual, passive flux elements ("corks") in x, y coordinates corresponding to the
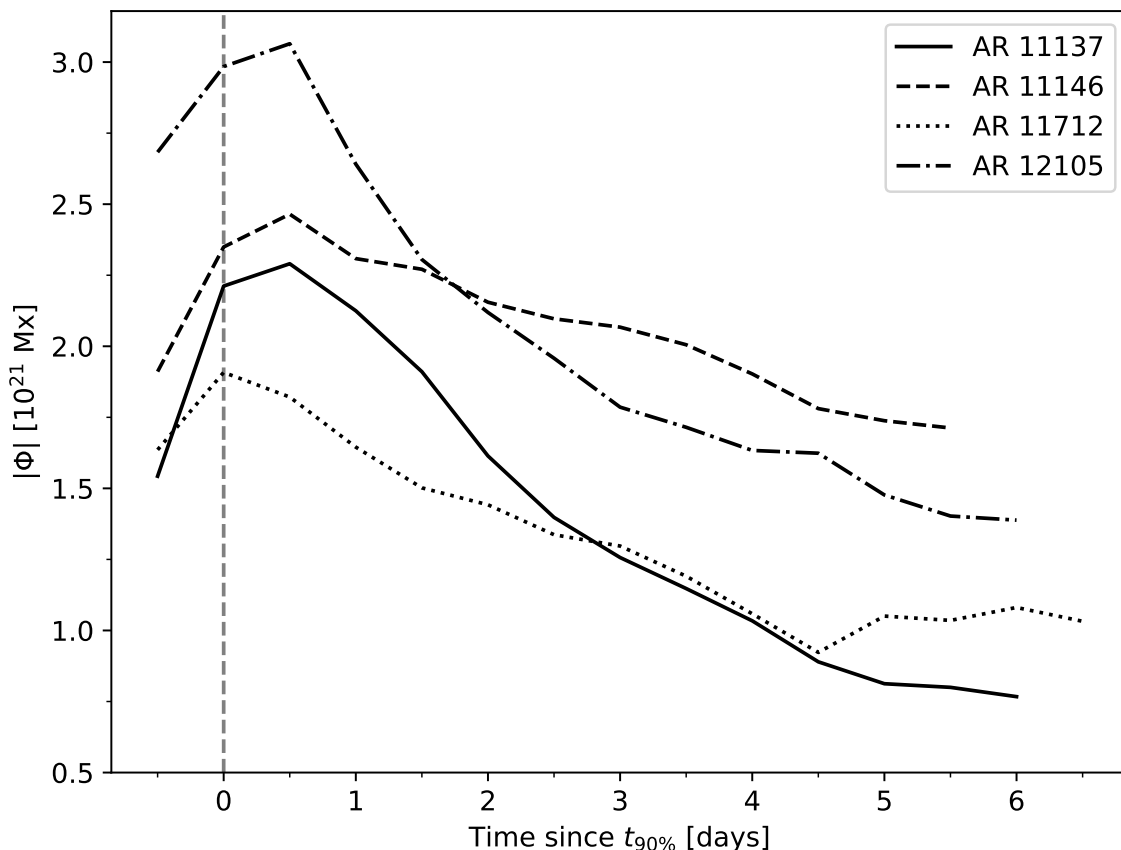
Figure 3.1: Evolution of the total unsigned magnetic flux of four ARs, calculated from twelve-hour averages of the μ-corrected line-of-sight magnetograms. The ARs are aligned in time relative to the time $t_{90\%}$ at which 90 % of the maximum flux has emerged. In one of the shown examples, this coincides with the time of peak flux.

longitudinal and latitudinal axes of the projected input magnetic field map. At each simulation time step Δt, each cork moves a certain distance from its former position. There are two contributions to this motion: a diffusive part, which is realized as a random walk, and an advective part, which is realized as a flow field that moves each cork according to the velocity vector at its position.

Langfellner et al. (2018) considered only unsigned magnetic field, and included spawning of randomly distributed new field as well as the random removal of existing field. We do not include the random spawning and removal, as we are studying the AR polarities, for which the magnetic field is dominated by the emergence. We have expanded the simulation by considering positive and negative field and incorporating flux cancellation between the two. Corks of opposite polarity that move within 1 Mm of each other were removed from the simulation. The distance threshold is the same as that used by Martin-Belda and Cameron (2016).

We initialized the simulations with individual time steps from the magnetogram cubes described in Sect. 3.2, recentered to the center of the AR at time $t_{90\%}$. A magnetic flux density of 1 Gauss in the observations corresponds to one cork in the simulation. The output of the simulations are magnetic field maps for each simulation time step Δt. The (signed) magnetic flux density at each grid element in these maps is the difference between

Table 3.1: Simulation cases.

Flow model u	Diffusion model D
No flows ('$u = 0$')	D_c
No flows ('$u = 0$')	D_f
u_{obs}	No diffusion ('$D=0$')
u_{obs}	D_c
u_{obs}	D_f
$u_{\nabla B}$	D_c
$u_{\nabla B}$	D_f
$u_{\widetilde{\nabla B}}$	D_c
$u_{\widetilde{\nabla B}}$	D_f

Notes. The simulations were run with a flow model (no flows, $u = 0$; observed flows, u_{obs}; parameterized inflows around ARs, $u_{\nabla B}$; or modified parameterized inflows, $u_{\widetilde{\nabla B}}$), and a diffusion model (no diffusion, $D = 0$; constant diffusivity, D_c; or flux-dependent diffusivity, D_f). Figure 3.3 shows snapshots from each simulation for AR 11137.

the number of positive and negative corks that have x, y coordinates within that grid element.

We ran the simulations with a simulation time step Δt of 30 minutes. We averaged the simulation output to the same twelve-hour averages as the observations for direct comparison between simulations and observations. For each AR, we ran 20 realizations of each simulation model and averaged over them to decrease the realization noise from the random-walk diffusion models. The number of realizations was limited by computation time. The results do, however, not differ from those with less (e.g., five) realizations.

3.3.1 Flow models

We use four different flow models in our simulations: no flow field ($u = 0$), flows from observations ($u = u_{obs}$), and two parameterized, gradient-based models ($u = u_{\nabla B}$ and $u = u_{\widetilde{\nabla B}}$). We ran each of these models with two different random-walk diffusion models. In an additional case, we did not add diffusion. Thus, we have nine different simulation setups (see Table 3.1).

No flows ($u = 0$). Here, we did not include a flow field in the simulation. Thus, only diffusion displaces the corks.

Observed flows ($u = u_{obs}$). In this model, we used the flow maps from Gottschling et al. (2021) for the ARs in the sample. The flows stem from local correlation tracking (LCT, November and Simon 1988) of solar continuum intensity images, and they are based on the data processing by Löptien et al. (2017), who used the Fourier local correlation tracking code (Welsch et al. 2004; Fisher and Welsch 2008) on full-disk continuum intensity images from SDO/HMI. Several changes in the data processing were made by Gottschling et al. (2021) in order to correct for additional systematic effects in the data from Löptien et al. (2017). Gottschling et al. (2021) describe these changes in detail. The flow maps are in Plate Carree projection with a grid spacing of 0.4°, with the same centering and twelve-hour time steps as the magnetograms (see Sect. 3.2). In the SFTM, these are Fourier-interpolated
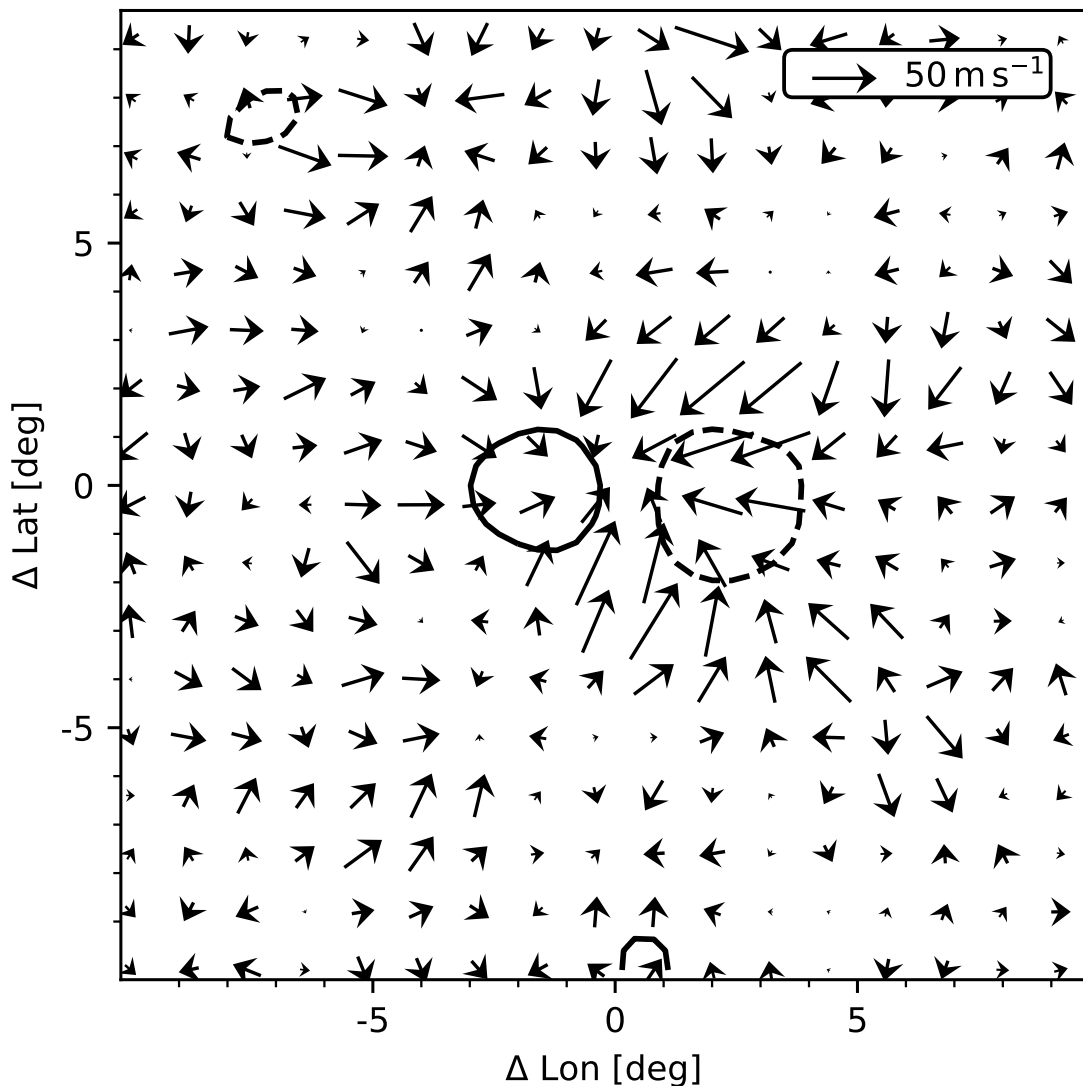
Figure 3.2: Average flows around the sample of ARs, in a twelve-hour average four days after $t_{90\%}$. The flow maps were smoothed with a Gaussian of width $\sigma = 0.8°$. The solid (dashed) contour indicates the magnetic field at $+(-)15$ Gauss.

to the 30 min simulation time step Δt. Figure 3.2 shows the average magnetic field and flows over the sample of ARs at four days after $t_{90\%}$. Converging flows toward the center of the AR are visible, with velocities on the order of $50\,\mathrm{m\,s^{-1}}$. Inflows are more pronounced along the latitudinal axis than along the longitudinal axis.

Parameterized inflows ($\boldsymbol{u} = \boldsymbol{u}_{\nabla B}$). We adopted the parametrization of the inflows around ARs by De Rosa and Schrijver (2006), who used it on the simulation by Schrijver (2001) to study the evolution of the field on large timescales, that is to say multiple rotations. Here, we applied it to the first few days after emergence, motivated by the resemblance of the observed flows to the inflows around ARs (see Fig. 3.2). The parametrization is

$$\boldsymbol{U} = \alpha \nabla \left(|\tilde{B}|^{\beta} \right), \tag{3.1}$$

where $\boldsymbol{U}$ is the flow field ($\boldsymbol{u}_{\mathrm{lon}}, \boldsymbol{u}_{\mathrm{lat}}$), $\tilde{B}$ is the magnetic field, smoothed with a Gaussian with

a full width at half maximum (FWHM) of 15°, and α and β are free parameters. Martin-Belda and Cameron (2017b) used Eq. (3.1) with $\beta = 1$ and normalized it such that the peak inflow velocity around an AR of 10° is $50 \, \mathrm{m \, s^{-1}}$, with $\alpha = 1.8 \times 10^8 \, \mathrm{m^2 \, Gauss^{-1} \, s^{-1}}$. We adopted these choices for our model. The choice of β was further motivated by the observed flux density corresponding to the product of the field strength and the filling factor. If the inflows are driven by excess cooling, as suggested by Spruit (2003), they are proportional to the filling factor, and thus $\beta = 1$. Because we investigated ARs shortly after their emergence, their extent is considerably smaller than 10°. Therefore, the inflows in this model have extents that are too large and amplitudes that are well below $50 \, \mathrm{m \, s^{-1}}$. In previous studies, these parameterized inflows led to flux clumping. In Appendix 3.6.2, we therefore compare the inflows from this parametrization to the flow field that would balance the diffusion of a flux concentration. If the inflows were stronger than this flow field, they would lead to flux clumping. We find that the inflows from this parametrization are too weak to cause flux clumping, as was also motivated above.

Modified parameterized inflows ($\boldsymbol{u} = \boldsymbol{u}_{\widetilde{\nabla B}}$). With this model, we aim for a parametrization of the inflows that more closely resembles the observed flows on our sample of comparatively small (and young) ARs, rather than the evolved large ARs on which the parameters of the above model ($\boldsymbol{u}_{\nabla B}$) are based. In order to capture both the spatial extent of the flows as well as their amplitude, we compared the extent of the magnetic field, smoothed with different levels of spatial smoothing, to the observed flow field. We found that the magnetic field smoothed with a Gaussian of $\sigma = 2°$ has a similar extent as the observed flows. The observed average inflow velocities increase from about $10 \, \mathrm{m \, s^{-1}}$ at $t_{90\%}$ to 40–$50 \, \mathrm{m \, s^{-1}}$ at $t_{90\%} + 5$ days. To capture this evolution, we fit a line between the observed flow velocities and the gradient of the smoothed magnetic field at the same location for each twelve-hour time step. The fit considers the area of $20° \times 20°$ around the center of the AR. We further selected only those pixels that lie within 2° of an absolute magnetic field density above 20 Gauss. We then fit a line to the relation between the flow velocity and the gradient against time. We used the slope and intercept of this fit to calculate the normalization α in Eq. (3.1) for each time step.

3.3.2   Diffusion models

We consider three different diffusion models. In the first case, diffusion is the same for all flux elements (D_c), in the second it is flux-dependent (D_f). In the third case, no diffusion is added ($D = 0$).

Constant diffusivity (D_c). In this model, the step length of the random walk of each cork along each axis is drawn from a normal distribution, with a standard deviation corresponding to a diffusion rate D that is constant for all corks. We ran simulations with diffusivities in the range between $D = 250$ and $722.5 \, \mathrm{km^2 \, s^{-1}}$.

Flux-dependent diffusivity (D_f). This model is based on De Rosa and Schrijver (2006). In their simulation, they treated the magnetic field as flux concentrations that can contain a varying amount of flux and that can merge and break up. The random walk step length Δr

of a flux concentration depends on the amount of flux in the concentration as

$$\Delta r = C(|\Phi|) \sqrt{4D\Delta t} \tag{3.2}$$

$$C(|\Phi|) = 1.7 \exp\left(\frac{-|\Phi|}{3 \times 10^{19} \text{ Mx}}\right), \tag{3.3}$$

where $|\Phi|$ is the absolute flux within a flux concentration and D is the diffusion rate (Schrijver 2001). This treatment of the magnetic field is different from our simulation, where we considered individual corks that have a constant amount of flux and performed individual random walks. To implement a flux-dependent diffusion rate in our simulation comparable to De Rosa and Schrijver (2006), at each simulation time step we calculated the cork density on a grid in longitude and latitude with grid spacing of 0.4°, oversampled it by 4x4 pixels, and smoothed it by 0.1°. For each cork, we then calculated the width Δr of the normal distribution from which the random walk step length is drawn using the cork density at the corks' position, with Eqs. (3.2) and (3.3). As reference diffusivity D in Eq. (3.2), we used $D = 250 \text{ km}^2 \text{ s}^{-1}$.

No diffusion (D = 0). For one simulation using the observed flows, we added no diffusion. In this case, only the flow field displaces the magnetic field.

3.4 Evaluation of the models

We ran simulations using the four different inflow models (Sect. 3.3.1) and the three different diffusion models (Sect. 3.3.2) on the sample of 17 ARs (Sect. 3.2). To evaluate the different simulations in comparison to the observations, for each time step, we measured the total unsigned flux within a disk of the central 5°, as well as the cross correlation between the observations and the simulations. We then studied different simulation start times.

3.4.1 Active region flux as a function of time

In this section, we initialize the simulations of each AR with the observed magnetic field at the time $t_{\text{start}} = t_{90\%} + 0.5$ days. In the simulations that use the observed flow field ($\boldsymbol{u}_{\text{obs}}$), stagnation points at which the velocities are zero have an infinitely small width. The magnetic field therefore tends to accumulate in very confined spaces. To reduce the emphasis on these small-scale features, we smoothed the simulated magnetic field maps with a Gaussian with a width of $\sigma = 0.8°$. A broader smoothing results in higher cross correlations, as the small-scale structures are smeared out.

Figure 3.3 shows the magnetic field from the observations and the different simulations for AR 11137 at the beginning and at the end of the simulations. For reference, Fig. 3.8 shows all time steps for four of the simulations along with the observations. In the observations, the leading polarity moves in the prograde direction and toward the equator over time. The trailing polarity is deformed. Its field disperses and clumps of flux leave the flux concentration. Both polarities lose flux due to flux cancellation between the two polarities as well as advection away from the AR.

In the simulations using the observed flows, the motions of the polarities resemble those in the observations (cf. the green and black contours in the first and second row in Fig. 3.3,
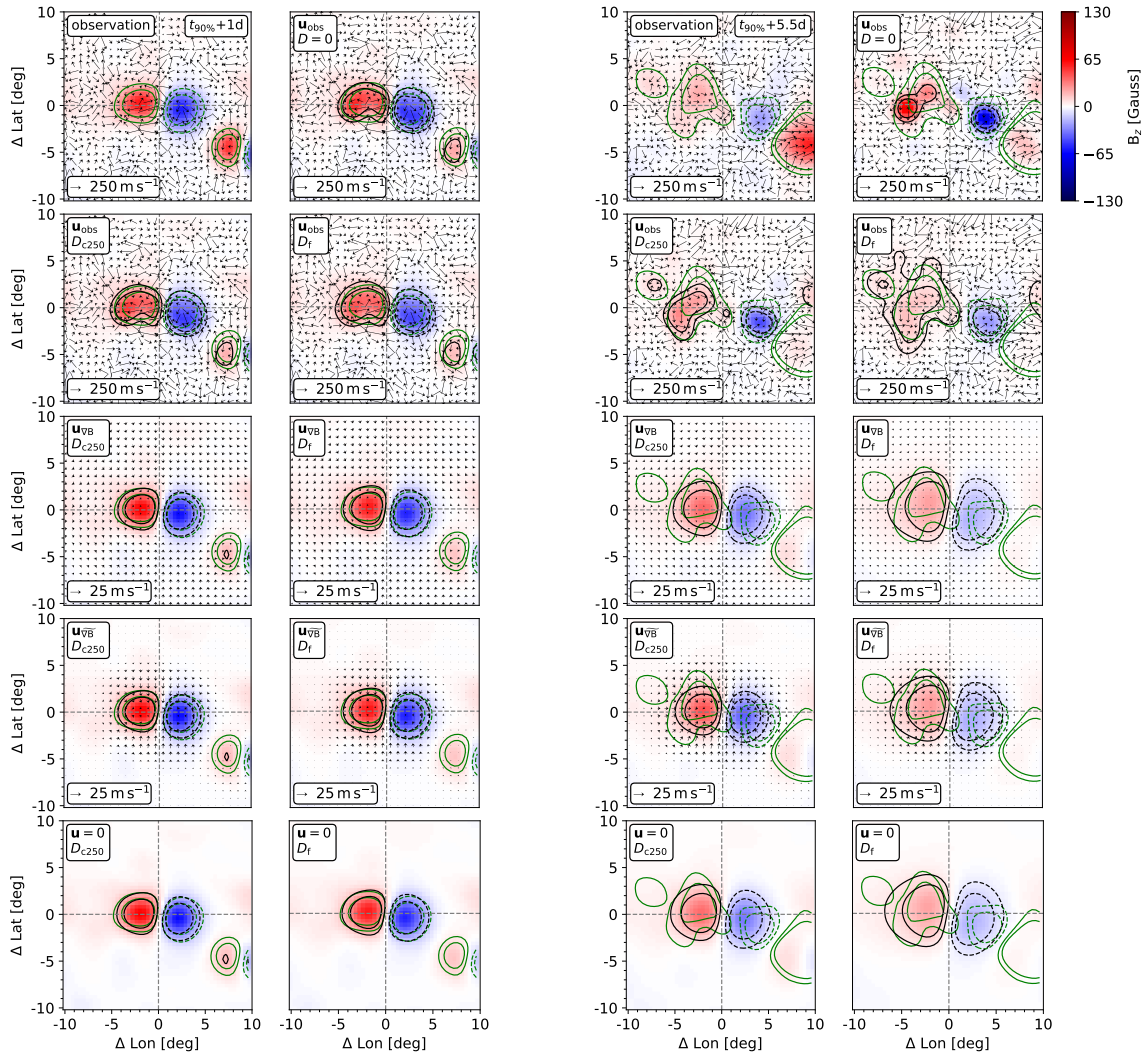
Figure 3.3: Two example time steps of the observations and the simulations for AR 11137. *The two columns on the left* show the first time step after simulation start, that is, 0.5 days after $t_{\text{start}} = t_{90\%} + 0.5$ days. *The two columns on the right* show the time step at the end of the simulations, at $t_{90\%} + 5.5$ days. The times are indicated in the upper right corner of the top left panels. At each of the two time steps, the top row shows the observed magnetic field and flows (*left*) and the simulation using observed flows and no additional diffusion (*right*). For all other rows, the left (right) panels show simulations with constant (flux-dependent) diffusivity D_{c} (D_{f}). From the second row to the bottom: observed flows, flows according to the parameterized inflow model, flows according to the modified parameterized inflow model, and no flows. The diffusion in the cases of constant diffusivity is $250\,\text{km}^2\,\text{s}^{-1}$. The arrows indicate the observed and the parameterized flows for the respective observations and simulations. Reference arrows are given in the lower left corners of each panel. Red (blue) indicates positive (negative) radial magnetic field. All maps have the same saturation at $\pm$ the rounded maximum absolute field strength in the central 10° from all simulation time steps. The green (black) contours indicate levels of half and a quarter of the minimum and maximum magnetic field in the central 10° of the observation (of each simulation) for each time step individually.

and the second row from the top in Fig. 3.8). This indicates that the supergranulation, which is the dominant signal in the flow maps, is effective in buffeting the magnetic field polarities. Figure 3.3 also shows the differences in the flow fields of the different models: The parameterized inflow model, $\boldsymbol{u}_{\nabla B}$, yields extended flows with low velocities on the order of $5\,\mathrm{m\,s^{-1}}$ (up to about $10\,\mathrm{m\,s^{-1}}$ for larger ARs in the sample). The modified parameterized inflow model, $\boldsymbol{u}_{\widetilde{\nabla B}}$, yields more confined flows with higher velocities on the order of $20\,\mathrm{m\,s^{-1}}$ (up to about $40\,\mathrm{m\,s^{-1}}$ for larger ARs in the sample), which is similar to the observed inflows (cf. Fig. 3.2). Figure 3.9 shows the averaged magnetic field and flows from all AR simulations and observations.

The flux-dependent diffusivity D_{f} (cf. Eq. (3.3)) increases the random walk step lengths of the magnetic flux elements (corks) in weaker field concentrations, and decreases it for corks in stronger field concentrations. The ARs considered here have relatively low magnetic field strengths (typically below $100\,\mathrm{Gauss}$). Therefore, the flux-dependent diffusivity increases the diffusivity for most of the flux elements in the simulation, and decreases it only for a small amount of flux at the center of some AR polarities. For comparison, we ran simulations with a range of constant diffusivities, from $D_{\mathrm{c}250} = 250\,\mathrm{km^2\,s^{-1}}$, which corresponds to the reference value of D_{f}, to $D_{\mathrm{c}722.5} = 722.5\,\mathrm{km^2\,s^{-1}}$, in increments of $50\,\mathrm{km^2\,s^{-1}}$. We note that $D_{\mathrm{c}722.5}$ corresponds to each cork experiencing no surrounding magnetic flux in the flux-dependent model D_{f}.

To evaluate how well the simulations reproduce the evolution of AR flux in the observations, for each time step, we calculated the total unsigned flux within a disk of the central $5°$ in the simulations and in the observations. The left panel of Fig. 3.4 shows the average total unsigned flux of some of the simulations as well as the observations as a function of time, calculated from all regions in the sample for $D_{\mathrm{c}450} = 450\,\mathrm{km^2\,s^{-1}}$. Appendix 3.6.5 shows the cases of $D_{\mathrm{c}250}$ and $D_{\mathrm{c}722.5}$. The results for $(\boldsymbol{u}_{\nabla B}, D_{\mathrm{f}})$, $(\boldsymbol{u}_{\widetilde{\nabla B}}, D_{\mathrm{f}})$, $(\boldsymbol{u}_{\nabla B}, D_{\mathrm{c}450})$, and $(\boldsymbol{u}_{\widetilde{\nabla B}}, D_{\mathrm{c}450})$ are very similar to the corresponding cases of $(\boldsymbol{u} = 0, D_{\mathrm{f}})$ and $(\boldsymbol{u} = 0, D_{\mathrm{c}450})$, and they are therefore not shown in the left panel of Fig. 3.4.

Flux loss in ARs is the result of the cancellation of opposite polarity flux as well as advection of flux away from the region. With our simulation, we can measure how much flux is lost in each of these processes separately. The change in total unsigned flux within an area from one time step to the next can be written as follows:

$$\Phi(t + \Delta t) = \Phi(t) + \Phi_{\mathrm{a\_in}} - \Phi_{\mathrm{a\_out}} - \Phi_{\mathrm{c}}, \tag{3.4}$$

where $\Phi(t)$ is the total unsigned flux in the area at time t, Δt is the simulation time step of $30\,\mathrm{min}$, $\Phi_{\mathrm{a\_in}}$ is the flux advected into the area, $\Phi_{\mathrm{a\_out}}$ is the flux advected out of it, and Φ_{c} is the flux lost due to cancellation of opposite-polarity field. In our simulation, this corresponds to counting all corks that move into or out of the AR area or cancel out with an opposite-polarity cork. As the AR area, we use the central disk with a radius of $5°$.

The right panel of Fig. 3.4 shows the total amount of flux lost between the starting time $t_{\mathrm{start}} = t_{90\%} + 0.5$ days and five days later for all nine simulations. The black line indicates the flux loss in the observations over the same period. Appendix 3.6.5 shows the simulations with $D_{\mathrm{c}250}$ and $D_{\mathrm{c}722.5}$, which are within the error consistent with the observations as well. The diffusivities that are consistent with the observed flux loss therefore range from about 250–$720\,\mathrm{km^2\,s^{-1}}$. In Appendix 3.6.6, we derive an analytical solution of the flux loss due to cancellation between two diffusing Gaussian distributions in the case of no flow field and constant diffusion. This is in good agreement with the flux
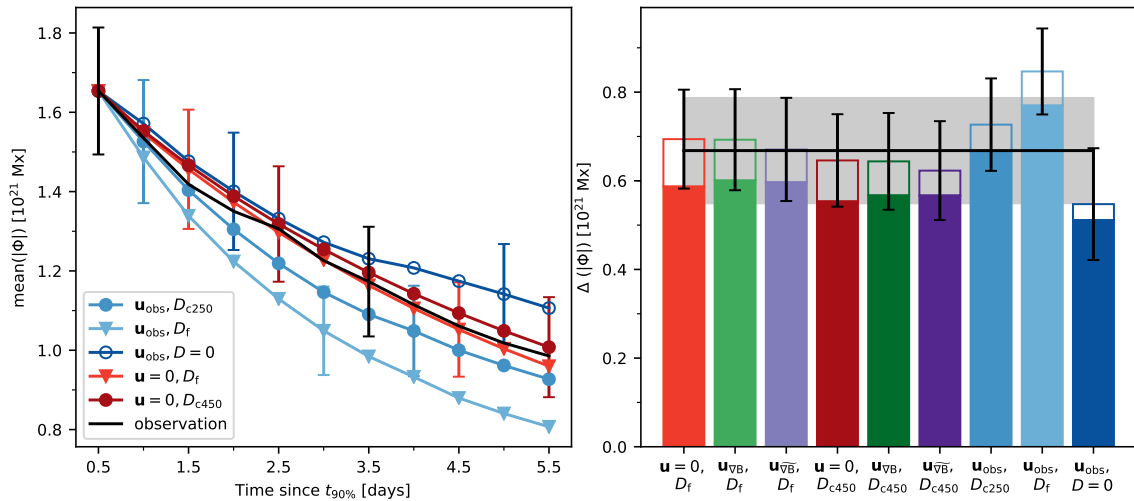
Figure 3.4: *Left*: Evolution of the total unsigned flux over the central disk with a radius of $5°$, averaged over the sample of ARs, for the observations and some of the simulations. The error bars indicate the standard error over the sample. Only every sixth error bar is plotted for readability. The data point at $t_{90\%} + 0.5$ days is the initial condition of the simulations. The diffusion in the simulation with constant diffusivity and no flows is $450 \, \mathrm{km^2 \, s^{-1}}$. *Right*: Amount of flux loss between the last time step of the simulations, at $t_{90\%} + 5.5$ days, and the time when the simulations were initialized, at $t_{90\%} + 0.5$ days. The black line indicates the flux loss in the observations over the same period, and the gray shaded area indicates the standard error. The solid and contoured bars indicate flux loss due to cancellation and advection, respectively.

loss due to cancellation in the corresponding simulation. With this small sample of ARs, and a time period of only 5 days, we cannot constrain the diffusivity further.

Figure 3.4 also shows that the total amount of flux loss is very similar for all models that use the same diffusion model (D_{f} or D_{c}). Increasing the strength of the inflows (no inflows $\boldsymbol{u} = 0$, weak inflows $\boldsymbol{u}_{\nabla \mathrm{B}}$, and stronger inflows $\boldsymbol{u}_{\widetilde{\nabla \mathrm{B}}}$) leads to both more flux loss due to flux cancellation and less flux loss due to advection for both diffusion models. These two effects partially cancel out, such that the net effect of the parameterized inflow models on the evolution of AR flux is small. In conclusion, the inflows are not important in the evolution of the flux budget of the AR in the first five days, but they might play a role in the distribution of the surrounding field.

In all three simulations that use the observed flows, the magnetic flux loss is consistent with that in the observations. The two models that include additional diffusion (blue triangles and filled circles) lose more flux than the simulation that uses the observed flow field and no additional diffusion (blue circles). This is because the additional random walk diffusion adds to the diffusion from the supergranulation and therefore enhances cancellation. We conclude that the bulk transport from supergranulation provides a means by which flux is carried away from the AR, which is consistent with a diffusion process.
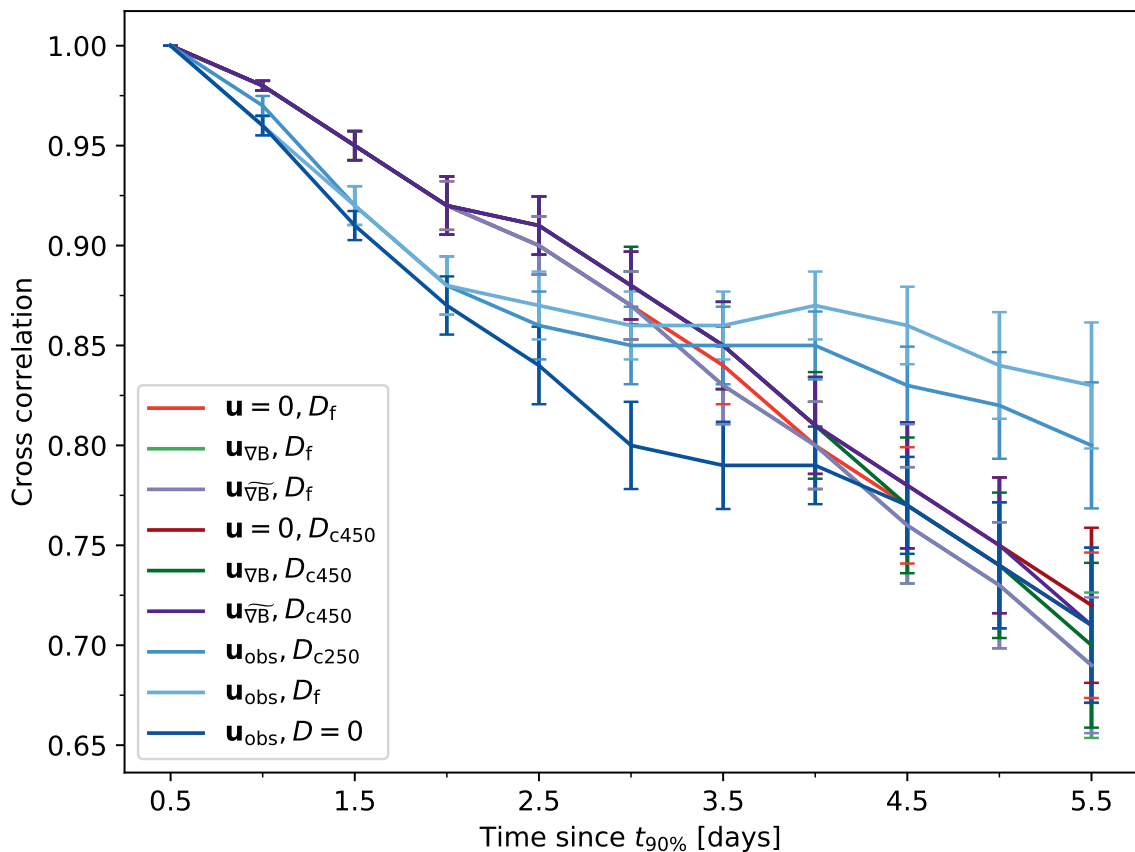
Figure 3.5: Evolution of the average cross correlation between the observed field and the simulations. The error bars indicate the standard error over the sample. The data point at $t_{90\%} + 0.5$ days is the initial condition of the simulations.

3.4.2   Cross correlation as a function of time

As a second evaluation of the simulations, we calculated the cross correlation between the observed and the simulated magnetic field in a window of $10° \times 10°$ around the center of each map for each of the 17 ARs. The window size was chosen to exclude other ARs in the field of view, which emerge at a later time or are significantly larger than the target AR, such that they exhibit moat flows (see for example the lower right corner in the top left panel of Fig. 3.3). As in Sect. 3.4.1, we use the simulations that are initialized at $t_{90\%} + 0.5$ days.

Figure 3.5 shows the average cross correlation of the simulations with the observations as a function of time. The cross correlation decreases monotonically for all simulations that use no or parameterized flows. The differences between the simulations with the same diffusion model and different flow models indicate that the small-scale distribution of the field is different. Comparing the simulations with the same flow model and different diffusion models, the cases with flux-dependent diffusivity D_f have higher cross correlations to the observations than the D_{c450} cases. This is within the error bars, however. The simulation using the observed flow field and no additional diffusion ($\boldsymbol{u}_{obs}, D = 0$) has a lower correlation to the observations than the other models for most of the four days of simulation time, whereas the two simulations using the observed flow field and additional
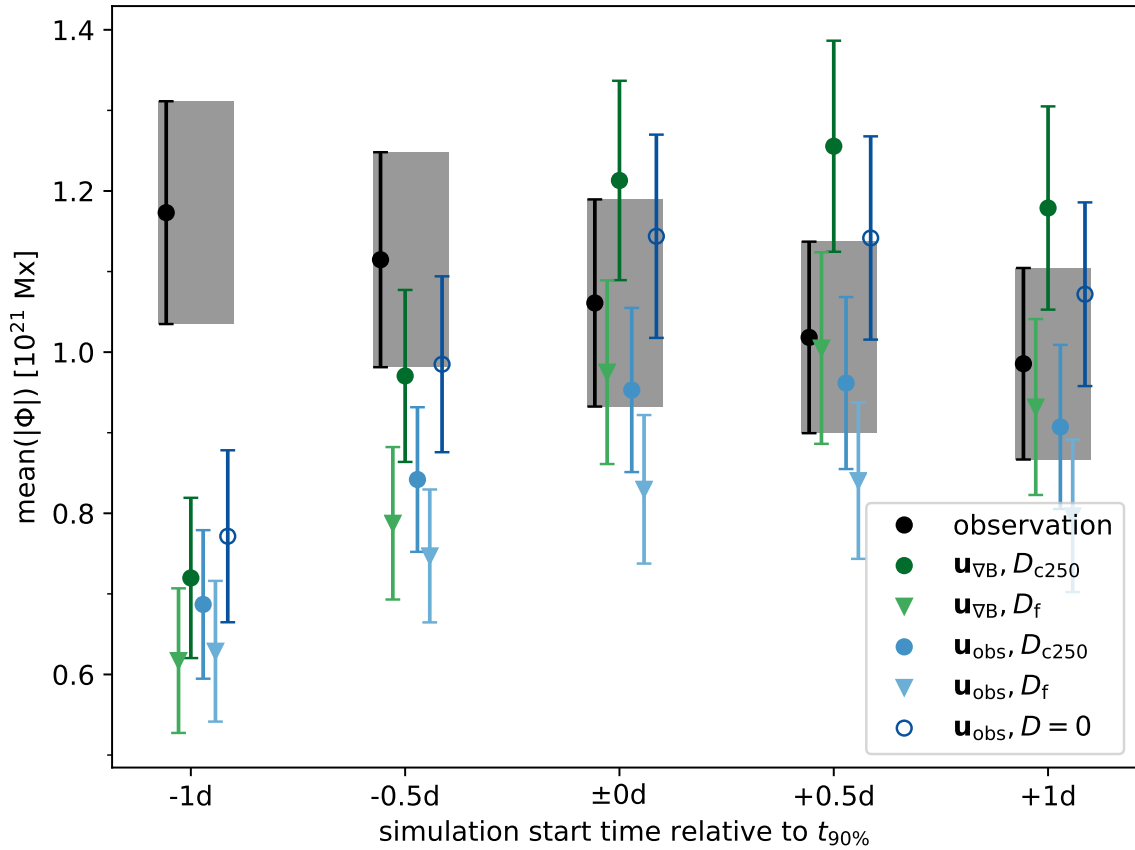
Figure 3.6: Total unsigned flux for different simulation start times relative to $t_{90\%}$ at 4.5 days after each simulation start time. The diffusion in the case of constant diffusivity is $250\,\text{km}^2\,\text{s}^{-1}$.

diffusion remain at a constant cross correlation (within errors) from 2–3 days onward. In the last few time steps, the cross correlation of these is larger than for cases with no or parameterized flows. The low cross correlation in the $\boldsymbol{u}_{\text{obs}}, D = 0$ case is a result of the flux being dragged by the flow into a different supergranular downflow lane in the simulation than in the observation. The additional diffusion in the cases of $(\boldsymbol{u}_{\text{obs}}, D_{\text{c450}})$ and $(\boldsymbol{u}_{\text{obs}}, D_{\text{f}})$ mitigates this and they therefore have a higher cross correlation.

3.4.3 Changing the simulation start time

In Sects. 3.4.1 and 3.4.2, we studied simulations initialized at $t_{90\%} + 0.5$ days. Here, we examine the dependence on the initial condition of the simulation by initializing the simulation with the magnetic field at times $t_{90\%} - 1$ day, $t_{90\%} - 0.5$ days, $t_{90\%}$, and $t_{90\%} + 1$ day.

Figure 3.6 shows the total unsigned flux for the simulations initialized at the five different starting times at 4.5 days after the initial condition of each simulation (that is, the same time has elapsed for all simulations). The simulations starting at $t_{90\%} + 0.5$ days yield the highest fluxes, because this time most often coincides with the time of peak flux of the ARs. Starting at later and earlier times decreases the AR flux in the simulations. In the two cases starting before $t_{90\%}$, the simulated fields differ largely from the observations, as most of the flux has not yet emerged onto the surface.

3.5   Discussion

In this work, we compared the observed evolution of 17 emerging ARs with surface flux transport simulations of these regions. We considered nine types of simulations with different models for diffusion and surface flows. We used models where the diffusion is zero, where it is the same for all flux elements, and where it is flux-dependent. For the surface flows, we used observations from local correlation tracking, parameterized models of the inflows around ARs, as well as no flows. We compared the evolution of the magnetic field in the observations and the simulations by calculating the cross correlation as well as the total unsigned flux of the ARs for all time steps. In addition, we tested the validity of the transport simulation for the study of young ARs by varying the starting time of the simulations relative to the time when the bulk of the AR flux has emerged.

We find that simulations using the observed flows can describe the evolution of the total unsigned flux of the ARs starting from the time when 90 % of the AR flux has emerged. The supergranular motions act as a random walk process in buffeting the magnetic field polarities. This finding from our simulation complements the observations by Schunker et al. (2019), who measured the standard deviation of the positions of AR polarities and draw the same conclusion. However, from our simulation we cannot make a statement as to whether the buffeting is flux-dependent or not. Additional diffusion improves the small-scale structure (measured as the cross correlation). Our findings allow for diffusion rates from the supergranular motions between 250–720 km^2 s^{-1}. The large range is due to the small sample of ARs which was suited for this study, as well as the limitation to about five days for the simulations.

The converging flows around emerging ARs, which we included as parameterized models, increase flux cancellation in the AR in the first five days after 90 % of the AR peak total unsigned flux has emerged. The resulting decrease in total unsigned flux is balanced by the decreased advection away from the AR, such that the evolution of the total flux associated with the AR is similar in the different models.

Acknowledgements

3.6 Appendix

3.6.1 List of active regions used in the simulation

The NOAA numbers of ARs used in the flux transport simulations are the following: 11088, 11137, 11145, 11146, 11167, 11288, 11437, 11547, 11624, 11626, 11712, 11786, 11789, 11811, 11932, 12064, and 12105.

3.6.2 Flow field balancing diffusion

We want to analyze the influence of the model inflows on the evolution of the magnetic field. For this, we calculated the flow field that compensates for the diffusion of a flux distribution, and compared it with the model inflows. For the magnetic field, we considered a 2D Gaussian distribution:

$$B(x, x_0, y, y_0, \sigma) = \frac{1}{2\pi\sigma^2} \exp\left\{ -\left(\frac{(x - x_0)^2}{2\sigma^2} + \frac{(y - y_0)^2}{2\sigma^2} \right) \right\}. \tag{3.5}$$

Its evolution in the presence of advection and diffusion is governed by the advection-diffusion equation (see for example Leighton 1964):

$$\frac{\partial B}{\partial t} + \nabla \cdot (\boldsymbol{u}B) = D\nabla^2 B, \tag{3.6}$$

where B is the radial magnetic field, $\boldsymbol{u}$ is the flow field, and D is the diffusivity. In the situation where the advection and the diffusion balance each other, such that $\frac{\partial B}{\partial t} = 0$, Eq. (3.6) reduces to

$$\nabla \cdot (\boldsymbol{u}B) = D\nabla^2 B. \tag{3.7}$$

Using the vector identity

$$\nabla \cdot (\boldsymbol{u}B) = B(\nabla \cdot \boldsymbol{u}) + (\nabla B) \cdot \boldsymbol{u}, \tag{3.8}$$

Eq. (3.7) then gives

$$B(\nabla \cdot \boldsymbol{u}) + (\nabla B) \cdot \boldsymbol{u} = D\nabla^2 B. \tag{3.9}$$

Using Eq. (3.5) and its derivatives gives

$$\left[\frac{\partial u_x}{\partial x} + \frac{\partial u_y}{\partial y} - \frac{(x - x_0)}{\sigma^2} u_x - \frac{(y - y_0)}{\sigma^2} u_y \right] = \\ \left[\frac{-2D}{\sigma^2} + \frac{D}{\sigma^4} \left((x - x_0)^2 + (y - y_0)^2 \right) \right]. \tag{3.10}$$

From this, we find the solution to be

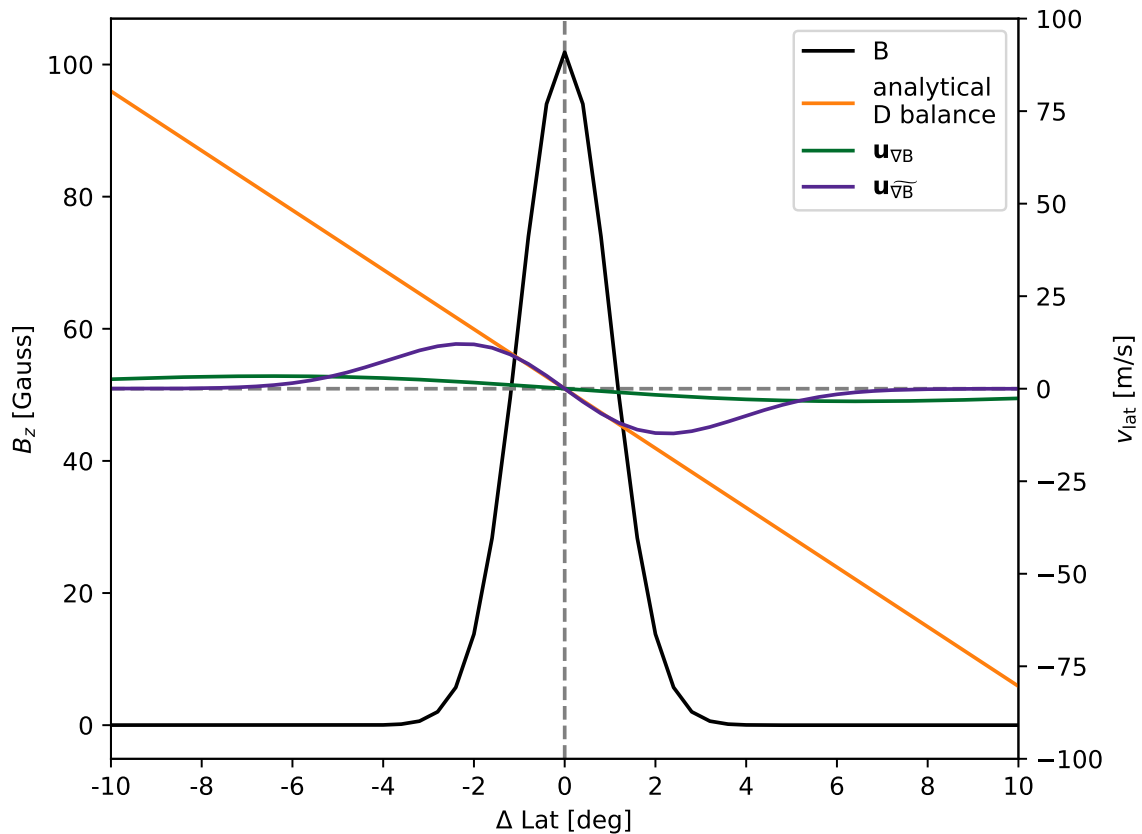$$\boldsymbol{u} = -\frac{D}{\sigma^2} \begin{pmatrix} (x - x_0) \\ (y - y_0) \end{pmatrix}. \tag{3.11}$$

Figure 3.7: Latitudinal cut through artificial data. The black line indicates the magnetic field, modeled as a Gaussian with a FWHM of 2.4°. The green line indicates the inflow model of $\boldsymbol{u}_{\nabla B}$ for the shown magnetic field. The purple line indicates the inflow model of $\boldsymbol{u}_{\widetilde{\nabla B}}$ at 2 days after $t_{90\%}$+0.5 days. The orange line shows the inflow profile that compensates for the diffusion of the magnetic field for a constant diffusivity of $250\,\mathrm{km}^2\,\mathrm{s}^{-1}$.

Figure 3.7 shows a latitudinal cut through the center of a 2D Gaussian with a full width at half maximum of 2.4° and a peak field strength of about 100 Gauss, along with the corresponding parameterized inflow models (green and purple lines) and the flow field which balances the effect of diffusion from Eq. (3.11). The figure shows that the $\boldsymbol{u}_{\nabla B}$ inflow model has velocities that are too low to compensate for the diffusion. The $\boldsymbol{u}_{\widetilde{\nabla B}}$ model is similar to the diffusion within ±2° of the center of the field distribution, and in fact it can overcome the diffusion, leading to flux clumping.

3.6.3   Evolution of observations and example simulations for AR 11137

Figure 3.8 shows all time steps of the observations and a few simulations for the AR 11137. The simulations were initialized at $t_{90\%} + 0.5$ days.
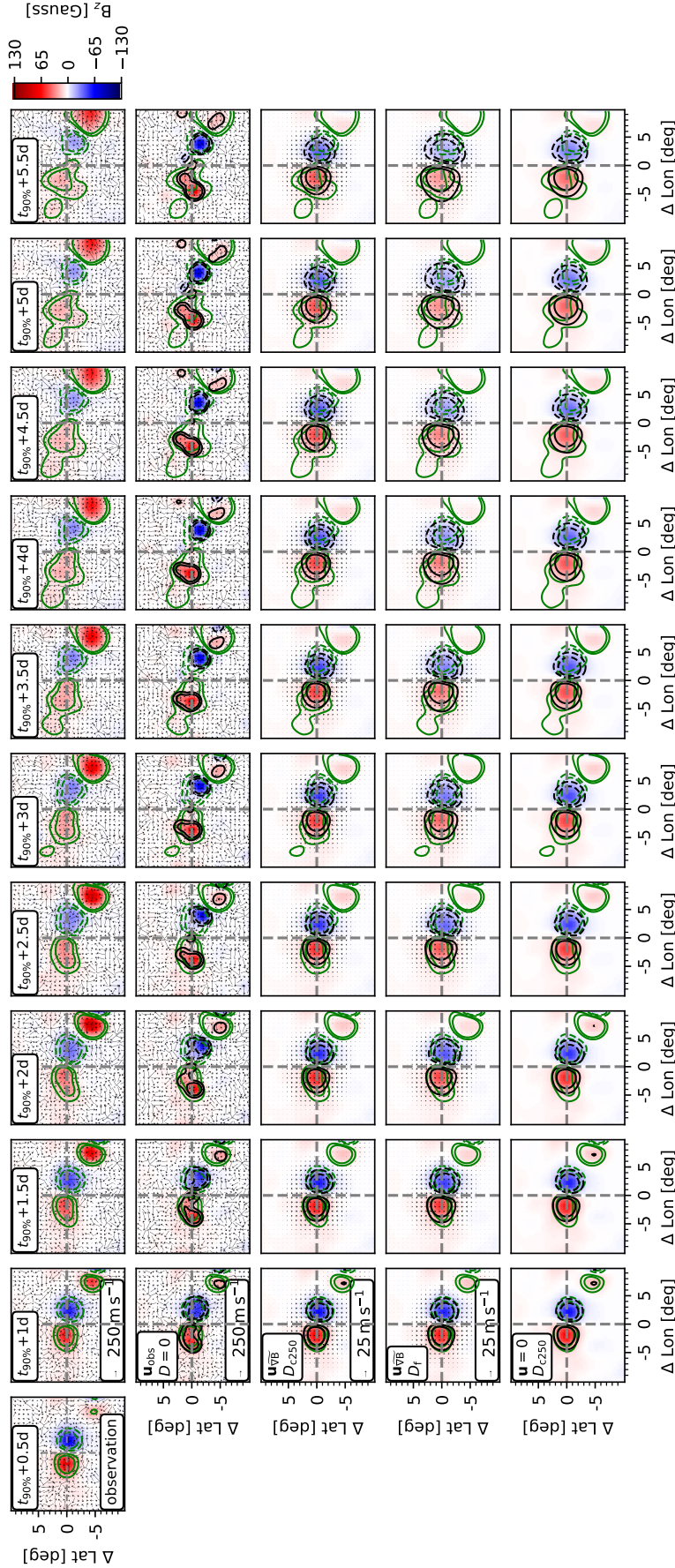
Figure 3.8: Evolution of the magnetic field of AR 11137 in the observations (top row) and four different simulations (second row from top: no flows and constant diffusivity, third row from top: flows according to the inflow parametrization based on the gradient of the magnetic field and constant diffusivity, fourth row from top: observed flows and constant diffusivity, bottom row: observed flows and flux-dependent diffusivity). The simulations are initialized at $t_{90\%} + 0.5$ days. The times are indicated in the upper left corner of the top panels. The diffusion in the cases of constant diffusivity is $250 \, \mathrm{km}^2 \, \mathrm{s}^{-1}$. Reference arrows are given in the lower left corners of the second column. Red (blue) indicates positive (negative) radial magnetic field. All maps have the same saturation, at $\pm$ the rounded maximum absolute field strength in the central $10°$ from all simulation time steps. The green (black) contours indicate levels of half and quarter of the minimum and maximum magnetic field in the central $10°$ of the observation (of each simulation), for each time step individually.

3.6.4   Average simulation

Figure 3.9 shows two time steps of the average over the 17 ARs for each simulation.

3.6.5   Changing the diffusivity

Figures 3.10 and 3.11 show the total unsigned flux over the central disk with a radius of 5° for constant diffusivities of 250 and 722.5 km^2 s^{-1}, respectively. The case D_{c250} corresponds to the diffusivity which serves as a reference for the flux-dependent diffusivity D_f. The case $D_{c722.5}$ corresponds to the flux-dependent model D_f in the case that all corks experience no surrounding magnetic flux.

3.6.6   Analytical solution for constant diffusion and no flows

We derived an analytical description of the evolution of the flux loss. For this, we considered the simplest case, with no flow field acting on the magnetic field ($\boldsymbol{u} = 0$), and with constant diffusivity (D_c). Because diffusion acts independently per dimension, a 1D setup can be used. For the magnetic field, we considered two Gaussian distributions of opposite sign, centered at positions $\pm\Delta x$ from the origin:

$$B_{\pm}(x, \sigma) = \frac{1}{\sqrt{2\pi\sigma^2}}\exp\left\{-\frac{(x \pm \Delta x)^2}{2\sigma^2}\right\}. \tag{3.12}$$

For small Δx, the difference between B_+ and B_- can be written as

$$B_+ - B_- = \frac{\Delta x}{\sqrt{2\pi\sigma^2}}\frac{\partial}{\partial x}\left(\exp\left\{-\frac{x^2}{2\sigma^2}\right\}\right). \tag{3.13}$$

From this, the total unsigned flux can be calculated as

$$\Phi = \frac{2\Delta x}{\sqrt{2\pi\sigma^2}}\int_{-\infty}^{0}\frac{\partial}{\partial x}\left(\exp\left\{-\frac{x^2}{2\sigma^2}\right\}\right)\mathrm{d}x \tag{3.14}$$

$$= \frac{2\Delta x}{\sqrt{2\pi\sigma^2}}. \tag{3.15}$$

Diffusion broadens the Gaussian distribution over time as

$$\sigma(t) = \sqrt{2Dt}. \tag{3.16}$$

Therefore,

$$\Phi(t) = \frac{2\Delta x}{\sqrt{2\pi}\sqrt{2Dt}} = \frac{\Delta x}{\sqrt{\pi Dt}}. \tag{3.17}$$

The total flux loss over time can thus be written as

$$\Delta\Phi(t) = \Phi(t_{\text{in}}) - \Phi(t_{\text{in}} + t) = \Phi(t_{\text{in}})\left(1 - \frac{\Delta x}{\sqrt{\pi D(t_{\text{in}} + t)}}\right), \tag{3.18}$$

with a suitable initial condition of $t_{\text{in}} = \frac{\Delta x^2}{\pi D}$.
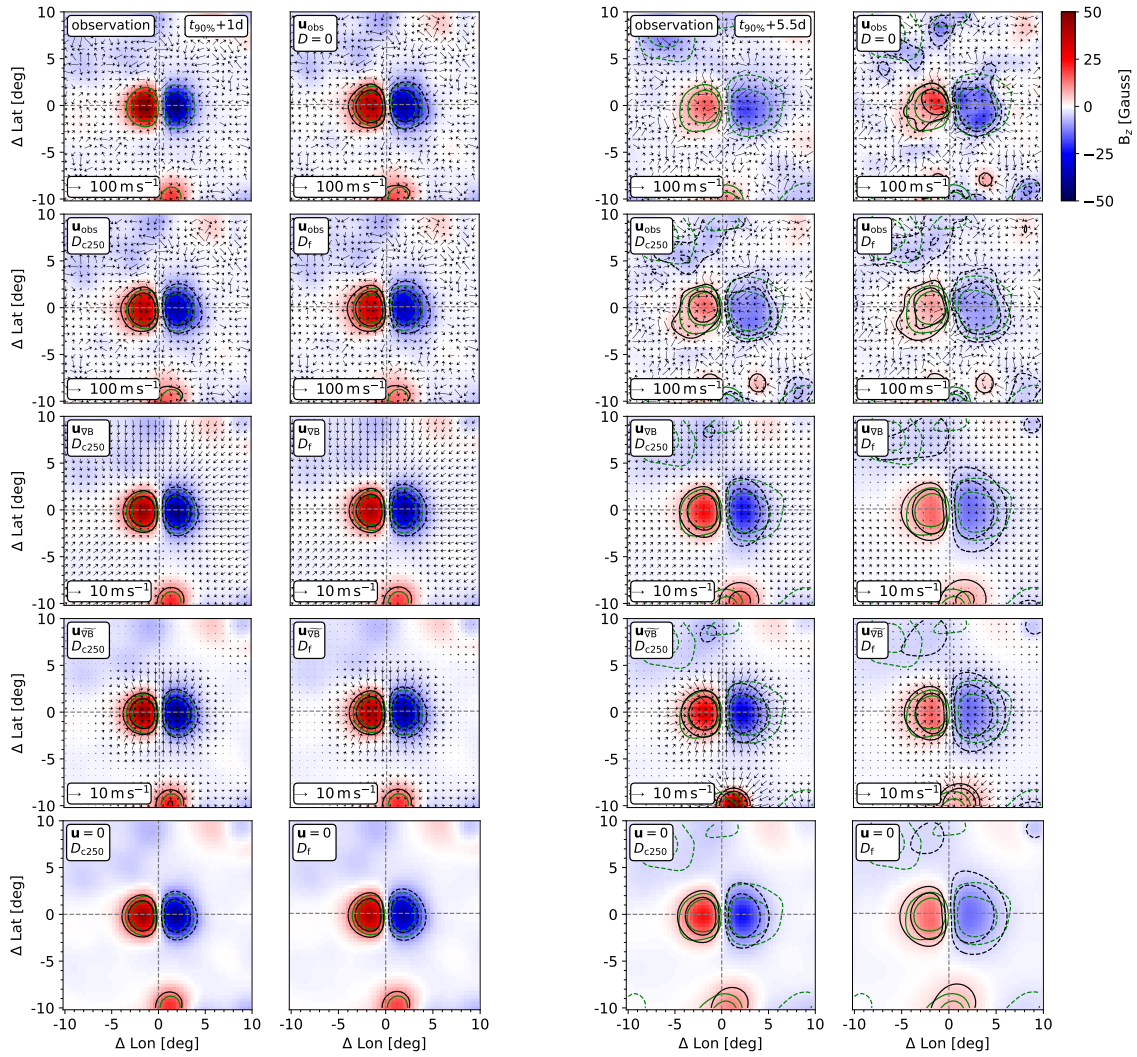
Figure 3.9: Two example time steps of the observations and the simulations, averaged over the individual ARs. *The two columns on the left* show the first time step after simulation start, that is, 0.5 days after $t_{start} = t_{90\%} + 0.5$ days. *The two columns on the right* show the time step at the end of the simulations at $t_{90\%} + 5.5$ days. The times are indicated in the upper right corner of the top left panels. At each of the two time steps, the top row shows the observed magnetic field and flows (*left*) and the simulation using observed flows and no additional diffusion (*right*). For all other rows, the left (right) panels show simulations with constant (flux-dependent) diffusivity D_c (D_f). From the second row to the bottom: observed flows, flows according to the parameterized inflow model, flows according to the modified parameterized inflow model, and no flows. The diffusion in the cases of constant diffusivity is $250\,\mathrm{km^2\,s^{-1}}$. The arrows indicate the observed and the parameterized flows for the respective observations and simulations. Reference arrows are given in the lower left corners of each panel. Red (blue) indicates positive (negative) radial magnetic field. All maps have the same saturation at ± the rounded maximum absolute field strength in the central 10° from all simulation time steps. The green (black) contours indicate levels of half and a quarter of the minimum and maximum magnetic field in the central 10° of the observation (of each simulation) for each time step individually.
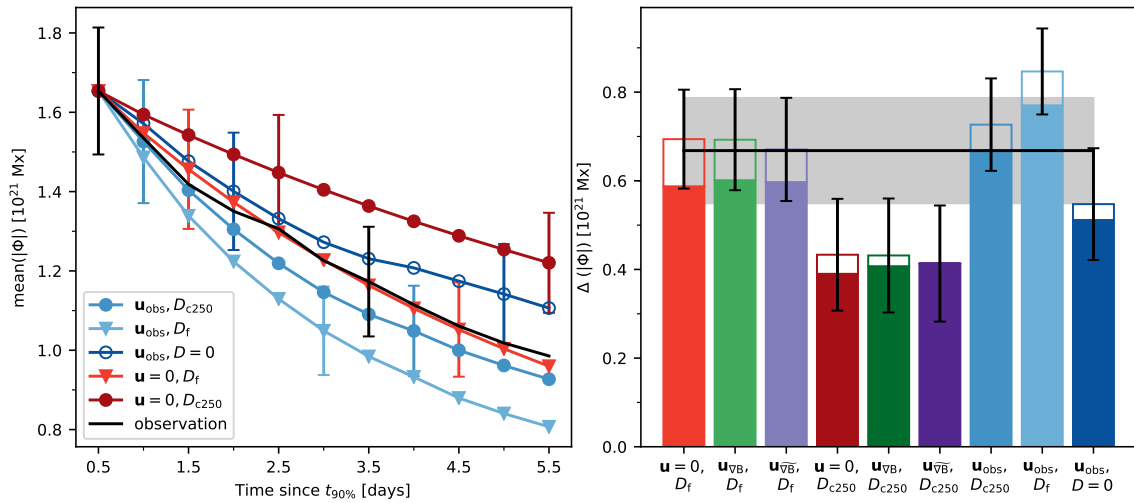
Figure 3.10: Left: Evolution of the total unsigned flux over the central disk with a radius of $5°$, averaged over the sample of ARs, for the observations and some of the simulations. The error bars indicate the standard error over the sample. Only every sixth error bar is plotted for readability. The data point at $t_{90\%} + 0.5$ days is the initial condition of the simulations. The diffusion in the simulation with constant diffusivity and no flows is $250\,\mathrm{km}^2\,\mathrm{s}^{-1}$. Right: Amount of flux loss between the last time step of the simulations, at $t_{90\%} + 5.5$ days, and the time when the simulations were initialized, at $t_{90\%} + 0.5$ days. The black line indicates the flux loss in the observations over the same period, and the gray shaded area indicates the standard error. The solid and contoured bars indicate flux loss due to cancellation and advection, respectively.
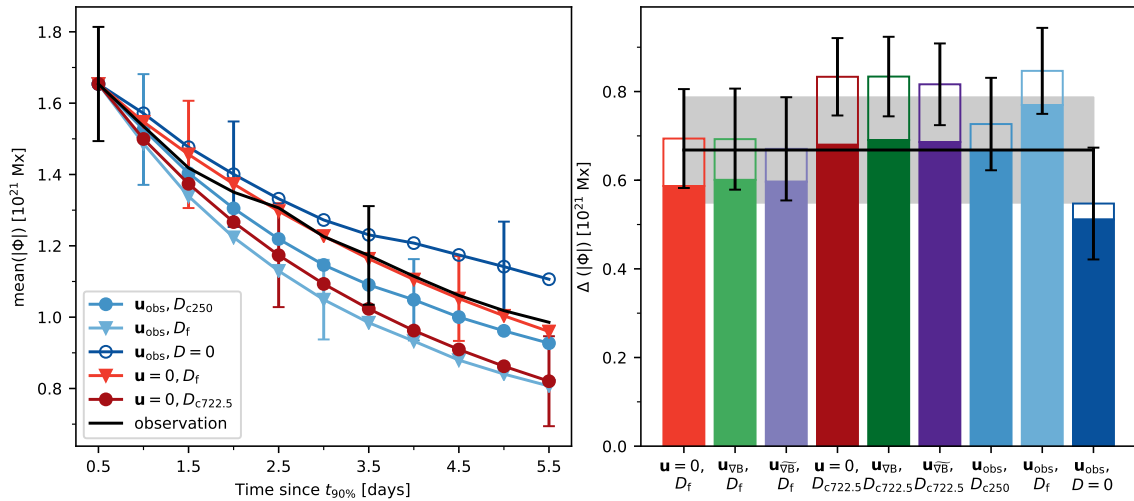

Figure 3.11: Same as Fig. 3.10, but with a diffusion in the cases of constant diffusivity for the parameterized flow models at $722.5\,\mathrm{km}^2\,\mathrm{s}^{-1}$.

To compare this to the simulation results, we considered an average $\Delta x = 1.8°$ (readers can compare this to the distance of the polarities from the center in the x-direction in Fig. 3.9) and a time of 5 days. With a total unsigned flux of 1.65×10^{21} Mx at the start time $t_{\mathrm{in}} = t_{90\%} + 0.5$ days, Eq. (3.18) gives, for the three cases of $D_{\mathrm{c}250} = 250 \, \mathrm{km^2 \, s^{-1}}$, $D_{\mathrm{c}450} = 450 \, \mathrm{km^2 \, s^{-1}}$, and $D_{\mathrm{c}722.5} = 722.5 \, \mathrm{km^2 \, s^{-1}}$, flux losses of 0.39×10^{21} Mx, 0.56×10^{21} Mx, and 0.71×10^{21} Mx, respectively. This is in good agreement with the flux losses due to diffusion (solid bars) in the simulations with the corresponding model of $(\boldsymbol{u} = 0)$, (D_{c}), as shown in Fig. 3.10, Fig. 3.4, and Fig. 3.11, respectively. The total flux loss in the observations over this time is 0.66×10^{21} Mx.

From Eq. (3.18), we calculated the minimum and maximum diffusivities $D_{\min}$, $D_{\max}$ that are consistent with the observed flux loss after 5 days to a 2-σ level. These are $D_{\min} = 280 \, \mathrm{km^2 \, s^{-1}}$ and $D_{\max} = 1350 \, \mathrm{km^2 \, s^{-1}}$, respectively. We note that this does not include flux loss due to transport away from the AR, which explains why $D_{\min}$ is larger than $D_{\mathrm{c}250}$.

4   Discussion

4.1   Radial vorticity of emerging active regions

In this chapter, I expand on the previous analyses by measuring the radial vorticity associated with active region emergence. For this, I use the observations of the magnetic field and surface flows from LCT on the HEAR survey sample of emerging active regions, which were introduced in the previous chapters. Radial vorticity measurements derived from LCT data have previously been used to study supergranulation (Langfellner et al. 2015) as well as swirling motions of EAR polarities (Sangeetha et al. 2020).

As described in Sect. 1.1.1, the structure of a magnetic flux tube can be characterized in terms of twist and writhe (e.g. Liu et al. 2014). Twist describes the winding of magnetic field lines in a tube around its central axis. Writhe describes the deformation of the central axis of the tube. Twist and writhe are important in the context of solar activity, as the activity of an AR is related to the complexity of the magnetic field (e.g. van Driel-Gesztelyi and Green 2015; Yan et al. 2008; Brown and Walker 2021, and references therein).

The twist is related to rotational motions. Observations have shown that some sunspots rotate (e.g. Brown et al. 2003; Zheng et al. 2016, and references therein), with rotation rates typically on the order of 1–$2\,°\,h^{-1}$. Sturrock et al. (2015) carried out simulations of twisted emerging flux tubes, and found that the magnetic field at the surface undergoes rotation, corresponding to rotating sunspots. Along with the rotation, they found vortical surface motions associated with the magnetic field. In a subsequent parameter study, Sturrock and Hood (2016) found that a stronger initial twist of the flux tube leads to stronger vortical motions at the surface.

Here, I inferred vortical motions associated with AR magnetic field polarities, as an indication of the rotation and the winding or unwinding of the magnetic flux. I analysed a sample of 20 ARs and performed ensemble averages to infer the mean evolution of the vortical motions. In the approximation of a 2D geometry, the radial vorticity can be calculated as:

$$\omega_z = (\nabla \times \mathbf{v})_z = \left(\frac{\partial v_y}{\partial x} - \frac{\partial v_x}{\partial y} \right), \qquad (4.1)$$

where ω_z is the radial vorticity, x and y are the directions along the longitudinal and latitudinal axis in Plate Carree projection, and v_x and v_y are the longitudinal and latitudinal velocities, respectively.

4.1.1 Active region sample

To study the evolution of the radial vorticity around active regions, I selected a sample of bipolar active regions which have very little magnetic activity in their immediate surroundings. These regions are from the SDO helioseismic emerging active regions (SDO/HEAR) survey (Schunker et al. 2016). I first selected those regions which do not develop a sunspot with a clear penumbra during the observed period from before emergence to up to seven days after emergence. This selection was done to exclude ARs with moat flows (e.g. Vargas Domínguez et al. 2008), as the moat flow would interfere with the vortical flows investigated in this study. The assessment whether an EAR develops a spot with a clear penumbra in the observed time frame is based on Gottschling et al. (2021), see Sect. 2.6.4. This first selection left 92 ARs in the sample. These were examined by eye to select for regions which do not experience any strong background field or active regions within ±5° in latitude and longitude from the AR center during the observation period. This left 20 EARs that are suitable for the study of the vortical flows in the close surroundings of the AR. For the further analysis, I also considered the 20 corresponding quiet Sun control regions of these regions in the HEAR survey (cf. Sect. 2.2.1).

4.1.2 Observational data

For the flow maps of the active regions and the control regions, I used the same LCT data as in Chapters 2 and 3. For the magnetic field maps, I used the same magnetogram cubes as in Chapter 3. These consist of μ-angle corrected line-of-sight magnetograms with a grid spacing of 0.4°, which is the same as that of the flow maps. The μ-angle correction is described in Appendix A. The data are in Plate Carree projection. Each time step is an average over twelve hours, with no overlap between subsequent time steps. At each time step, the flow maps and magnetograms are centered at the center of the AR at that time. In addition, I created two other data sets by shifting the maps such that the leading polarity and the trailing polarity are at the image center, respectively. Averages over each of these two data sets are thus relative to the leading / the trailing polarity. For all of the following analysis, the data were corrected for Hale's law and Joy's law (see Sect. 2.3.5).

4.1.3 Radial vorticity of active region polarities

Figure 4.1 shows the vorticity maps for all 20 EARs for the first twelve-hour time step after emergence. In some cases, the AR polarity is dominated by a single-sign vortical flow, for example the trailing polarity of AR 11088. In many cases however, the polarity shows a complex structure, with vortical flow contributions of different signs (for example AR 11148).

To study the average vorticity associated with AR polarities, I averaged the magnetograms and the vorticity maps over the 20 individual ARs. This was done in three ways: relative to the trailing polarity, relative to the center of the active region (as shown in Fig. 4.1), and relative to the leading polarity. Only those grid elements in the vorticity maps are considered that correspond to a magnetic field strength above (below) the threshold of $+(-) 50$ Gauss (cf. Fig. 4.1). This threshold was chosen to exclude small-scale field away from the AR polarity complexes. After emergence, the AR polarities move away from the
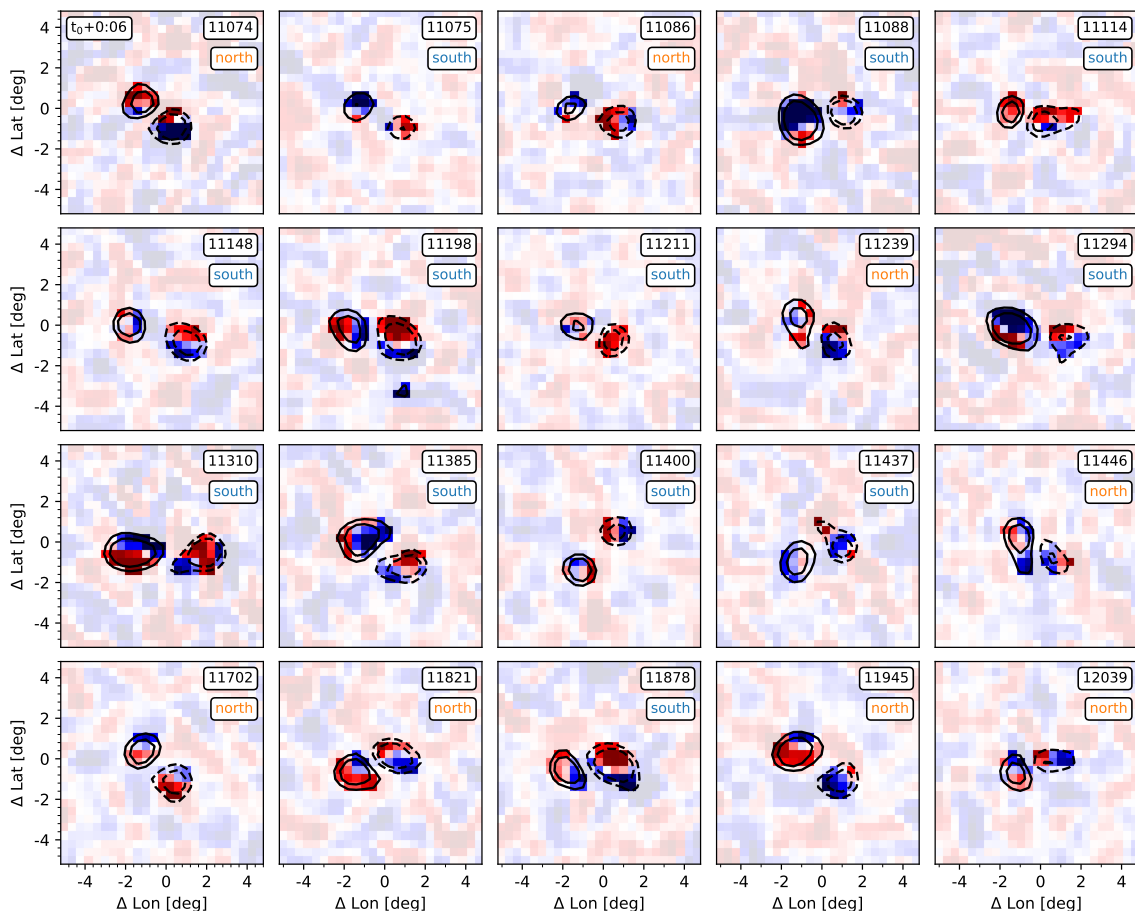
Figure 4.1: Vorticity maps for all 20 EARs in the sample. Each map is an average over the first twelve hours after emergence, and centered to the center of the AR at this time. Red (blue) indicates positive/counterclockwise (negative/clockwise) vorticity, saturated at $\pm 2 \times 10^{-5}\,\mathrm{s}^{-1}$. The solid (dashed) black contours indicate the magnetic field at $+(-)\,50\,\mathrm{Gauss}$ (outer contour) and at $+(-)\,100\,\mathrm{Gauss}$ (inner contour). The vorticity maps are partially transparent outside of these areas, to guide the eye. The AR number and the hemisphere on which each region emerged are indicated in the upper right corner of each panel.

AR center over time, at different angles and distances. Averaging relative to the different positions therefore provides different information, as the field and the flow signatures are more concentrated around e.g. the leading polarity when averaging relative to its position.

Figure 4.2 shows the average vorticity map and flow field, for the three different averaging positions, at the first time step after emergence. In the case of averaging relative to the trailing polarity (left panel), the trailing polarity has a predominantly positive vorticity. When averaging relative to the center (middle panel), an east-west aligned bipolar structure of the vorticity is visible on the leading polarity, which is more clear in the average relative to the leading polarity (right panel). This is also seen for some of the individual ARs in Fig. 4.1. This bipolar structure indicates two swirling motions from the leading side of the polarity towards the trailing side. One possible interpretation of this signature is that it represents the prograde motion of the leading polarity relative to the
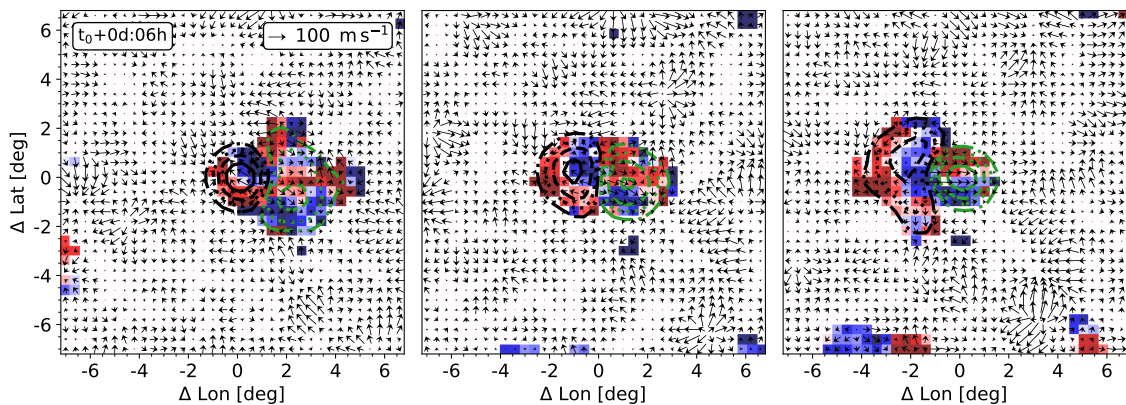
Figure 4.2: Vorticity maps of the average AR. Each map is an average over the first twelve hours after emergence, and centered to the center of the AR at this time. The three panels show (from left to right) the cases of averaging relative to the trailing polarity, the center of the AR, and the leading polarity. Red (blue) indicates positive/counterclockwise (negative/clockwise) vorticity, saturated at $\pm 1 \times 10^{-5}\,\mathrm{s}^{-1}$. The arrows indicate the horizontal flow field. The black (green) contours indicate the positive (negative) magnetic field at ± 10, ± 25 ± 50, and $\pm 100\,\mathrm{Gauss}$ as dashed-dotted lines, dotted lines, dashed lines, and solid lines, respectively.

surrounding plasma, which creates these vortices as it drags the plasma with it. In the map centered on the trailing polarity (left panel), the leading polarity shows a mixed vorticity as well, which is however less structured than in the other two cases.

To study how the vorticity of the individual AR polarities evolves over time, I calculated the average signed vorticity associated with the leading and the trailing magnetic field polarity, for each AR and each time step. I considered the magnetic field in a box of $10° \times 10°$ around the center of the AR and calculated the mean vorticity over all grid elements that have a corresponding magnetic flux density above (below) the threshold value of $+(-)\,50\,\mathrm{Gauss}$, for the trailing (leading) polarity, as above. Figure 4.3 shows the evolution of the average vorticity of the two polarities for each AR. The errors were calculated as the standard error. For several ARs, the leading and the trailing polarity show vorticities of opposite sign shortly after emergence. No clear trend is obvious after a few days after the emergence.

To quantify the occurrence of vorticity shortly after emergence, Table 4.1 lists for all ARs in the sample the sign of the average vorticity of each polarity, measured in the first time step after emergence, at the threshold of $+(-)\,50\,\mathrm{Gauss}$. Only values that are nonzero above the uncertainty were taken into account, which is taken as the standard error. This table shows that a vorticity that deviates from zero by more than the uncertainty is only measured for about half of the polarities (21 out of in total 40). It also shows that the regions in the southern hemisphere have a clear trend towards the leading polarity having positive vorticity, and the trailing polarity having negative vorticity. The regions in the northern hemisphere do not show such a clear distinction. It seems unlikely that there is a fundamental difference between the northern and the southern hemisphere that causes this. Rather, it is presumably a result of the selection of regions and the small sample of regions on which this study is carried out, due to the strict constraints in the selection.
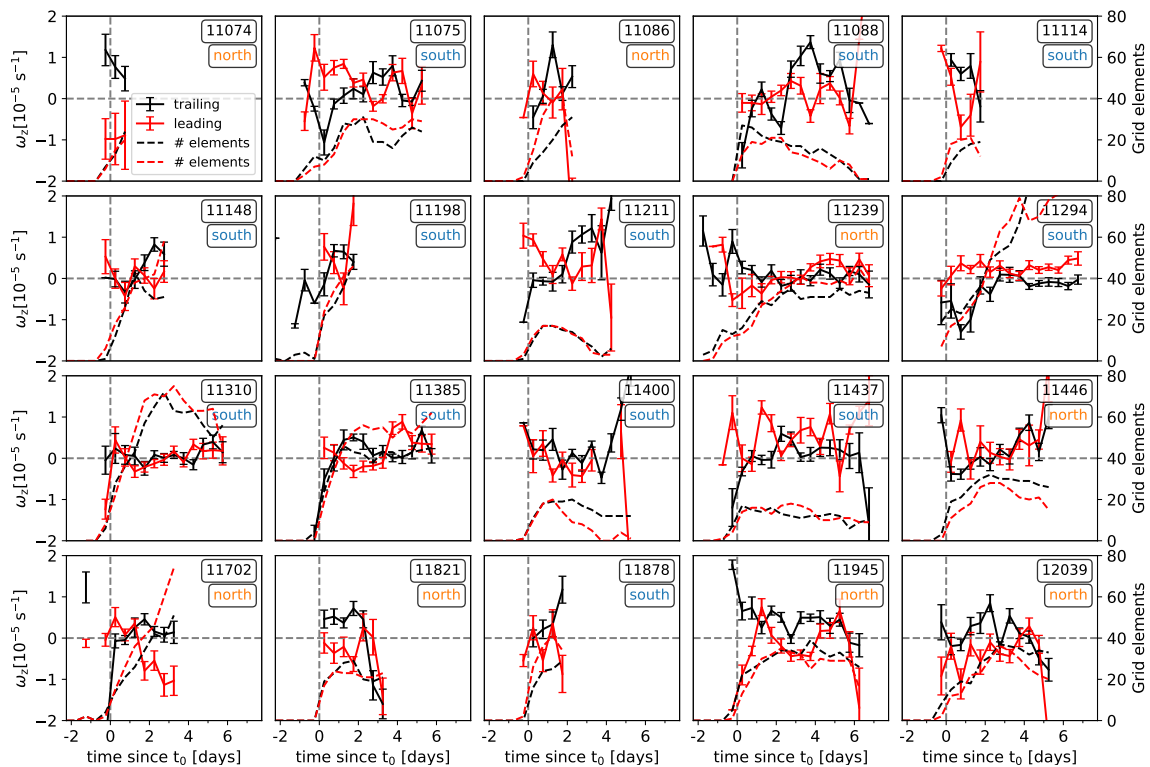
Figure 4.3: Evolution of the average vorticity, for the leading (red) and the trailing (black) polarity, for all individual active regions in the sample. The dashed lines indicate the number of grid elements that contribute to each time step. The AR number and the hemisphere on which each region emerged are indicated in the upper right corner of each panel.

4.1.4   Average radial vorticity

The individual ARs in the sample emerge at different latitudes, have different maximum total unsigned magnetic fluxes, and different shapes. Also, they show complex vorticity structures, cf. Figs. 4.1 and 4.2. With this in mind, I investigate the average evolution of the vorticity associated with the active region polarities. For this, I calculated the ensemble-averaged vorticity of the trailing (leading) polarity from all vorticity grid elements of the different ARs corresponding to a magnetic flux density above (below) the threshold of $+(-)\,50$ Gauss.

The top (bottom) left panel of Fig. 4.4 shows the signed (unsigned) average vorticity, respectively. The top left panel shows that in the first half day after emergence, the leading and the trailing polarity are on average associated with opposite signs of vorticity, with the leading polarity rotating counterclockwise and the trailing polarity rotating clockwise. Afterwards, the two change sign. In the time between 1 and 6 days after emergence, the trailing polarity is associated with a vorticity on the order of $0.2 \times 10^{-5}\,\mathrm{s}^{-1}$. This corresponds to a rotation of about $50°$ of the polarity around its axis over this time.

The bottom left panel shows an increase in the average unsigned vorticity of the leading polarity from before until about 2 days after emergence. No clear trend is visible afterwards, and there is also no clear trend for the trailing polarity over the covered time period. This result differs from the findings of Sangeetha et al. (2020), who in a case study measured

89

Table 4.1: Sign of the average vorticity ω_z of each polarity, at a threshold of $+(-)\,50$ Gauss, in the first half day after emergence. The index '*lead*' ('*trail*') indicates the leading (trailing) polarity, the index $+(-)$ indicates a positive (negative) average vorticity. If the average vorticity is not different from 0 within the uncertainty, a '$-$' is inserted for both signs of vorticity.

AR	hemisphere	$\omega_{lead,+}$	$\omega_{lead,-}$	$\omega_{trail,+}$	$\omega_{trail,-}$
11074	north		1	1	
11075	south	1			1
11086	north	1			1
11088	south	$-$	$-$		1
11114	south	1		1	
11148	south	$-$	$-$	$-$	$-$
11198	south	1		$-$	$-$
11211	south	1		$-$	$-$
11239	north		1	1	
11294	south	$-$	$-$		1
11310	south	$-$	$-$	$-$	$-$
11385	south	$-$	$-$		1
11400	south	$-$	$-$	$-$	$-$
11437	south	$-$	$-$		1
11446	north	$-$	$-$		1
11702	north	1		$-$	$-$
11821	north	$-$	$-$	1	
11878	south	$-$	$-$	$-$	$-$
11945	north		1	1	
12039	north	$-$	$-$	$-$	$-$
sum	north	2	3	4	2
sum	south	4	0	1	5
sum	all	6	3	5	7

the vorticity of AR 11211 and found an increase of the unsigned vorticity over time from before to about 2 days after emergence, for both polarities. This trend is also not visible in the unsigned vorticity of AR 11211 from the data presented here. On the other hand, the opposite signs of the average signed vorticity for the leading and the trailing polarity of AR 11211 around the time of emergence (cf. Fig 4.3) match those of Sangeetha et al. (2020). Note that the signs of vorticity for AR 11211 in Fig 4.3 are opposite to those of Sangeetha et al. (2020), because of the corrections for Hale's law and Joy's law for southern hemisphere regions, see Sect. 2.3.5.

To better assess the noise in the observed vorticity maps on the average vorticity measurement above, I repeated the above analysis for the control regions. For this, I used the vorticity maps of the quiet Sun control regions together with the magnetogram masks of the active regions. The right panels of Fig. 4.4 show the signed (top) and the unsigned (bottom) vorticity maps of this measurement. In the time between emergence (vertical gray dotted line) and about five days after emergence (that is, the time interval during which the
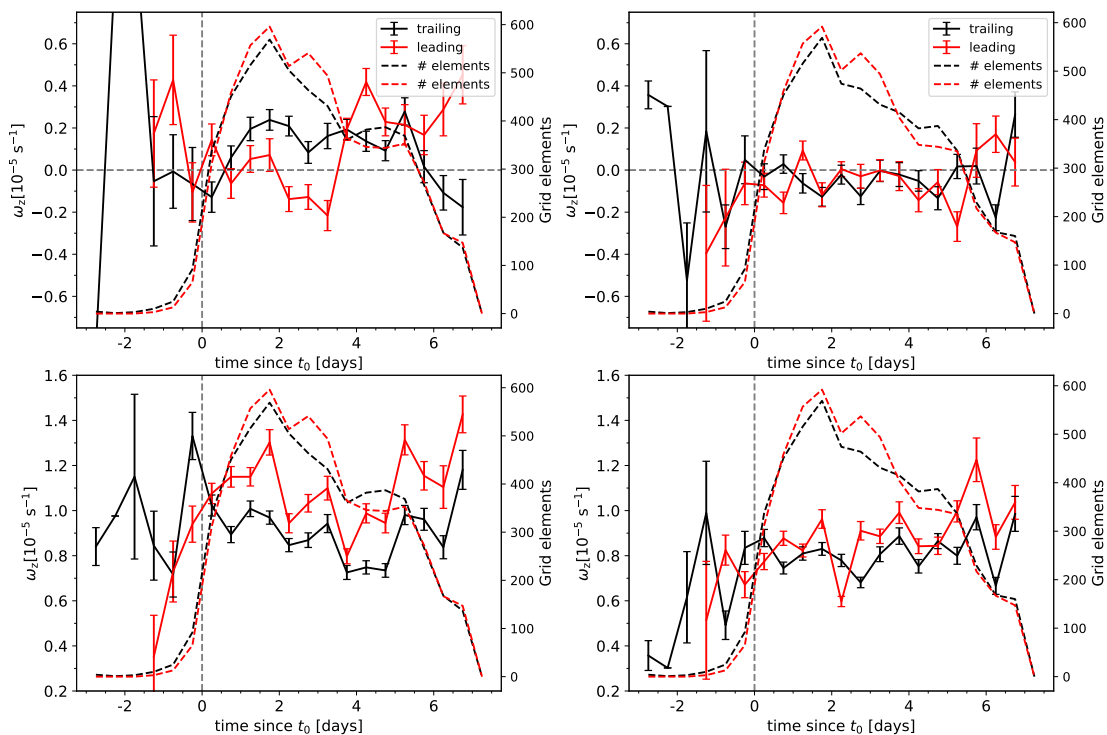
Figure 4.4: Evolution of the average vorticity, for the leading (red) and the trailing (black) polarity. Calculated from all grid elements corresponding to a magnetic flux density above (below) $+(-)$ 50 Gauss from the individual active regions. The left and right panels show the average vorticities from the vorticity maps of the active regions and control regions, respectively. The dashed lines indicate the number of grid elements that contribute to each time step. Top panels: average signed vorticity, bottom panels: average unsigned vorticity.

average is computed from more than about 300 grid elements), the average vorticity of the control region sample shows no systematic evolution for either of the polarities, and varies between about $\pm 0.15 \times 10^{-5} \, \mathrm{s}^{-1}$. Considering this as a more robust noise estimate, in the case of the average AR polarities only the opposite-rotating signature between 2 and 3.5 days is significant. The symmetric part of this indicates a solid-body rotation of the flux concentration.

The above analysis shows that different ways of measuring the average vorticity associated with the emergence of active region polarities are possible. No concise conclusions can be made with the present data. A restriction to a shorter time window after emergence would increase the number of suitable ARs, and thus decrease the noise in the average vorticity measurements. An important test would be to infer the surface flows from independent measurements, for example by tracking magnetic features instead of the granulation pattern.

For a more complete interpretation of the observations, a model would be needed. This could test for instance whether a rising flux tube that has a horizontal velocity relative to the surrounding plasma is able to create the observed vortical motions. Another test would be to simulate a flux tube with rotating polarities and investigate its effect on the plasma. The observed signatures could then be used to constrain the properties of the modelled flux tubes.

5   Conclusion and Outlook

This work presents new results on the flows associated with the emergence of active regions. By using measurements of solar surface flows from local correlation tracking on a sample of 182 emerging active regions, I found that:

- Starting one day before the emergence, there is a converging flow towards the center of active regions. This flow has velocities on the order of 20–$30\,\mathrm{m\,s^{-1}}$, and was observed also by Birch et al. (2016). Here I found that this converging flow terminates around the time of emergence.

- During emergence, there is a prograde flow at the position of the leading polarity (Birch et al. 2016). I found that this flow is not present for ARs with low magnetic flux (that is, in the subsample of regions with lowest flux, which has a mean flux of $1.5 \times 10^{21}\,\mathrm{Mx}$).

- After emergence, inflows form. I found that these inflows set in at later times (relative to emergence) for ARs with higher peak flux. This ranges from 1 to 4 days for the sample of ARs used here, where the mean flux in the subsample with lowest (highest) flux is $1.5 \times 10^{21}\,\mathrm{Mx}$ ($1.5 \times 10^{22}\,\mathrm{Mx}$). The inflows have higher velocities (about $50\,\mathrm{m\,s^{-1}}$) and larger extents (about $7°$) than the converging flows before emergence. On the other hand, they are somewhat smaller than the inflows around evolved ARs reported in the literature.

Studying the evolution of the surface magnetic flux of 17 active regions in the first five days after the bulk of their flux has emerged, and comparing it to the evolution of their magnetic flux in a local surface flux transport model that includes diffusion and advection by a flow field, I could infer that:

- Surface flux transport models can be applied after $90\,\%$ of the AR total unsigned magnetic flux have emerged. ARs that host a sunspot with moat flows were not considered in this, because of the relatively coarse grid scale in the simulations.

- The models using flow fields from observations can reproduce the evolution of the active region magnetic flux. The dominant scale in these flow maps is supergranulation, which buffets the magnetic field.

- The inflows around ARs, included in the simulations in parameterized form, do not play a role in the evolution of the AR magnetic flux in these first days after emergence. The increase of flux cancellation due to these inflows is balanced by a decrease of diffusive transport away from the AR.

For a better understanding of the effect that ARs and the flows associated with them have on the global magnetic field, surface flux transport models on ARs with sunspots would test the applicability of SFTMs in this state of AR evolution. For this, a higher resolution of the observed flows is needed, such that the magnetic field and the moat flow around the spots have little overlap. This would enable local SFTM studies on all young ARs, which in turn would help to assess the impact of the early evolution of ARs on the global field, in global simulations. SFTMs can also be used to study the formation of the tilt angle, by prescribing the observed flows on artificial emergences, and by including the action of the Coriolis force on parameterized inflows.

Another way to extend this work is to connect to the measurements of a cyclonic component of the inflows by Hindman et al. (2009). These are not readily visible in the ensemble-averaged flow maps presented in this work (Sect. 2.4). One reason for this might be that the signal Hindman et al. (2009) measured is on the order of $5\,\mathrm{m\,s^{-1}}$, which is below the noise level in the ensemble-averaged flow maps (see Sect. 2.3.5). Another possibility is that the retrograde flow reported by Braun (2019), which is also seen in this work, contributes to this average cyclonic motion. Measuring the flow components parallel and orthogonal to closed contours around the AR magnetic field in a temporal sequence might give some insight to where and when such a cyclonic motion forms.

It is not yet understood how the different flows associated with ARs form. To get a more complete picture of their formation and evolution, flow measurements at different depths in the solar interior, with local helioseismology, should be carried out. This would constrain the subsurface evolution, which is important for understanding the formation depth and rise speed of the magnetic field. Subsurface measurements of vortical flows would help to answer the question at what point twist and tilt are introduced to emerging flux tubes.

An important open question is the relation between the converging flows around active regions before emergence, the inflows around active regions that set in during the first days after emergence, and the inflows around large, established active regions. The differences in velocities and extents of the former two suggest that they might be driven by different processes. To understand the relation between the inflows shortly after emergence and the inflows in the late evolution of ARs, observations of ARs throughout their evolution are needed. From the vantage point of the Earth however, active regions for which the emergence time is observed can only be tracked for less than 10 days (taking into account foreshortening at the limb).

One way to overcome this limitation is to use far-side imaging from helioseismic holography to detect the emergence of ARs over the whole solar surface. With such age determinations of ARs, the flows associated with ARs can be observed from the vantage point of the Earth throughout AR evolution, by studying samples of ARs that emerge at all solar longitudes, as well as by unambiguously tracking ARs over multiple rotations.

Further progress will be possible with recent and future satellite missions. The Solar Orbiter (SO) was launched in February 2020 into an eccentric orbit around the Sun, such that its vantage point of the Sun constantly changes relative to that of the Earth. This will make dual-perspective observations of the magnetic field and the flows possible, which on the one hand increases data coverage of the solar sphere, and on the other hand improves vector field measurements, as the degeneracy in field disambiguation is lifted. This facilitates measurements that relate the evolution of the magnetic field to the flows,

which could help understand the underlying processes of the flows. Robust measurements of the radial field also help to calculate accurate positions of AR polarities, which is important for tilt angle measurements as well as ensemble averaging. In addition, SO can be used to calibrate far-side imaging with helioseismic holography, for the emergence of active regions.

Other than SO, it has been in discussion for several years to send a satellite for solar observations to the Lagrange point L5, trailing behind the Earth on its orbit at 60° with respect to the Sun-Earth line. In addition to the advantages from SO, continuous full-disk observations from L5 would, because of the fixed vantage point (relative to the Earth), increase the time over which continuous observations can be carried out, for all solar features, including active regions. For the same reason, it would reduce noise in far-side imaging.

Aside from observations, it is necessary to consider simulations of rising magnetic flux, and to understand under which conditions simulations produce properties of the surface magnetic field and the flows that are consistent with observations. Properties of the observed magnetic field that are important are the evolution of the tilt angle, the evolution of the total flux, the polarity separation, as well as magnetic tongues. Studying the sensitivity of the outcome of the simulations to changes in simulated properties, such as the rise speed, flux geometry, convection, or the twist of the rising flux, will further our understanding of the underlying processes.

Bibliography

Abbett, W. P., Fisher, G. H., Fan, Y., 2001, The Effects of Rotation on the Evolution of Rising Omega Loops in a Stratified Model Convection Zone, ApJ, 546, 1194–1203, `astro-ph/0008501`

Arlt, R., Vaquero, J. M., 2020, Historical sunspot records, Living Reviews in Solar Physics, 17, 1

Astropy Collaboration, Robitaille, T. P., Tollerud, E. J., Greenfield, P., Droettboom, M., Bray, E., Aldcroft, T., Davis, M., Ginsburg, A., Price-Whelan, A. M., Kerzendorf, W. E., Conley, A., Crighton, N., Barbary, K., Muna, D., Ferguson, H., Grollier, F., Parikh, M. M., Nair, P. H., Unther, H. M., Deil, C., Woillez, J., Conseil, S., Kramer, R., Turner, J. E. H., Singer, L., Fox, R., Weaver, B. A., Zabalza, V., Edwards, Z. I., Azalee Bostroem, K., Burke, D. J., Casey, A. R., Crawford, S. M., Dencheva, N., Ely, J., Jenness, T., Labrie, K., Lim, P. L., Pierfederici, F., Pontzen, A., Ptak, A., Refsdal, B., Servillat, M., Streicher, O., 2013, Astropy: A community Python package for astronomy, A&A, 558, A33, `1307.6212`

Astropy Collaboration, Price-Whelan, A. M., Sipőcz, B. M., Günther, H. M., Lim, P. L., Crawford, S. M., Conseil, S., Shupe, D. L., Craig, M. W., Dencheva, N., Ginsburg, A., VanderPlas, J. T., Bradley, L. D., Pérez-Suárez, D., de Val-Borro, M., Paper Contributors, P., Aldcroft, T. L., Cruz, K. L., Robitaille, T. P., Tollerud, E. J., Coordination Committee, A., Ardelean, C., Babej, T., Bach, Y. P., Bachetti, M., Bakanov, A. V., Bamford, S. P., Barentsen, G., Barmby, P., Baumbach, A., Berry, K. L., Biscani, F., Boquien, M., Bostroem, K. A., Bouma, L. G., Brammer, G. B., Bray, E. M., Breytenbach, H., Buddelmeijer, H., Burke, D. J., Calderone, G., Cano Rodríguez, J. L., Cara, M., Cardoso, J. V. M., Cheedella, S., Copin, Y., Corrales, L., Crichton, D., D'Avella, D., Deil, C., Depagne, É., Dietrich, J. P., Donath, A., Droettboom, M., Earl, N., Erben, T., Fabbro, S., Ferreira, L. A., Finethy, T., Fox, R. T., Garrison, L. H., Gibbons, S. L. J., Goldstein, D. A., Gommers, R., Greco, J. P., Greenfield, P., Groener, A. M., Grollier, F., Hagen, A., Hirst, P., Homeier, D., Horton, A. J., Hosseinzadeh, G., Hu, L., Hunkeler, J. S., Ivezić, Ž., Jain, A., Jenness, T., Kanarek, G., Kendrew, S., Kern, N. S., Kerzendorf, W. E., Khvalko, A., King, J., Kirkby, D., Kulkarni, A. M., Kumar, A., Lee, A., Lenz, D., Littlefair, S. P., Ma, Z., Macleod, D. M., Mastropietro, M., McCully, C., Montagnac, S., Morris, B. M., Mueller, M., Mumford, S. J., Muna, D., Murphy, N. A., Nelson, S., Nguyen, G. H., Ninan, J. P., Nöthe, M., Ogaz, S., Oh, S., Parejko, J. K., Parley, N., Pascual, S., Patil, R., Patil, A. A., Plunkett, A. L., Prochaska, J. X., Rastogi, T., Reddy Janga, V., Sabater, J., Sakurikar, P., Seifert, M., Sherbert, L. E., Sherwood-Taylor, H., Shih, A. Y., Sick, J., Silbiger, M. T., Singanamalla, S., Singer, L. P., Sladen, P. H.,

Sooley, K. A., Sornarajah, S., Streicher, O., Teuben, P., Thomas, S. W., Tremblay, G. R., Turner, J. E. H., Terrón, V., van Kerkwijk, M. H., de la Vega, A., Watkins, L. L., Weaver, B. A., Whitmore, J. B., Woillez, J., Zabalza, V., Contributors, A., 2018, The Astropy Project: Building an Open-science Project and Status of the v2.0 Core Package, AJ, 156, 123

Barnes, G., Birch, A. C., Leka, K. D., Braun, D. C., 2014, Helioseismology of Pre-emerging Active Regions. III. Statistical Analysis, ApJ, 786, 19, `1307.1938`

Bellot Rubio, L. R., Balthasar, H., Collados, M., Schlichenmaier, R., 2003, Field-aligned Evershed flows in the photosphere of a sunspot penumbra, A&A, 403, L47–L50

Berghmans, D., Auchère, F., Long, D. M., Soubrié, E., Zhukov, A. N., Mierla, M., Schühle, U., Antolin, P., Parenti, S., Harra, L., Podladchikova, O., Aznar Cuadrado, R., Buchlin, É., Dolla, L., Verbeeck, C., Gissot, S., Teriaca, L., Haberreiter, M., Katsiyannis, A. C., Rodriguez, L., Kraaikamp, E., Smith, P. J., Stegen, K., Rochus, P., Halain, J. P., Jacques, L., Thompson, W. T., Inhester, B., 2021, Extreme UV quiet Sun brightenings observed by Solar Orbiter/EUI, arXiv e-prints, arXiv:2104.03382, `2104.03382`

Birch, A. C., Braun, D. C., Leka, K. D., Barnes, G., Javornik, B., 2013, Helioseismology of Pre-emerging Active Regions. II. Average Emergence Properties, ApJ, 762, 131, `1303.1391`

Birch, A. C., Schunker, H., Braun, D. C., Cameron, R., Gizon, L., Lo ptien, B., Rempel, M., 2016, A low upper limit on the subsurface rise speed of solar active regions, Science Advances, 2, e1600 557–e1600 557, `1607.05250`

Birch, A. C., Schunker, H., Braun, D. C., Gizon, L., 2019, Average surface flows before the formation of solar active regions and their relationship to the supergranulation pattern, A&A, 628, A37

Bobra, M. G., Sun, X., Hoeksema, J. T., Turmon, M., Liu, Y., Hayashi, K., Barnes, G., Leka, K. D., 2014, The Helioseismic and Magnetic Imager (HMI) Vector Magnetic Field Pipeline: SHARPs - Space-Weather HMI Active Region Patches, Sol. Phys., 289, 3549–3578, `1404.1879`

Bogart, R. S., Baldner, C., Basu, S., Haber, D. A., Rabello-Soares, M. C., 2011a, HMI ring diagram analysis I. The processing pipeline, in GONG-SoHO 24: A New Era of Seismology of the Sun and Solar-Like Stars, vol. 271 of Journal of Physics Conference Series, p. 012008

Bogart, R. S., Baldner, C., Basu, S., Haber, D. A., Rabello-Soares, M. C., 2011b, HMI ring diagram analysis II. Data products, in GONG-SoHO 24: A New Era of Seismology of the Sun and Solar-Like Stars, vol. 271 of Journal of Physics Conference Series, p. 012009

Brandenburg, A., 2005, The Case for a Distributed Solar Dynamo Shaped by Near-Surface Shear, ApJ, 625, 539–547, `astro-ph/0502275`

Brandenburg, A., Rogachevskii, I., Kleeorin, N., 2016, Magnetic concentrations in stratified turbulence: the negative effective magnetic pressure instability, New Journal of Physics, 18, 125011, `1610.03459`

Braun, D. C., 2019, Flows around Averaged Solar Active Regions, ApJ, 873, 94, `1902.02298`

Bray, R. J., Loughhead, R. E., 1979, Sunspots.

Brown, D., Walker, A., 2021, A Semi-Automatic Method to Measure the Rotation of Sunspots, Sol. Phys., 296, 48

Brown, D. S., Nightingale, R. W., Alexander, D., Schrijver, C. J., Metcalf, T. R., Shine, R. A., Title, A. M., Wolfson, C. J., 2003, Observations of Rotating Sunspots from TRACE, Sol. Phys., 216, 79–108

Caligari, P., Moreno-Insertis, F., Schussler, M., 1995, Emerging Flux Tubes in the Solar Convection Zone. I. Asymmetry, Tilt, and Emergence Latitude, ApJ, 441, 886

Cameron, R. H., Schüssler, M., 2012, Are the strengths of solar cycles determined by converging flows towards the activity belts?, A&A, 548, A57, `1210.7644`

Cameron, R. H., Jiang, J., Schmitt, D., Schüssler, M., 2010, Surface Flux Transport Modeling for Solar Cycles 15-21: Effects of Cycle-Dependent Tilt Angles of Sunspot Groups, ApJ, 719, 264–270, `1006.3061`

Cameron, R. H., Jiang, J., Schüssler, M., 2016, Solar Cycle 25: Another Moderate Cycle?, ApJ, 823, L22, `1604.05405`

Chae, J., Moon, Y.-J., Park, Y.-D., 2004, Determination of magnetic helicity content of solar active regions from SOHO/MDI magnetograms, Sol. Phys., 223, 39–55

Charbonneau, P., 2013, Solar and Stellar Dynamos, Saas-Fee Advanced Course

Charbonneau, P., 2020, Dynamo models of the solar cycle, Living Reviews in Solar Physics, 17, 4

Chen, F., Rempel, M., Fan, Y., 2017, Emergence of Magnetic Flux Generated in a Solar Convective Dynamo. I. The Formation of Sunspots and Active Regions, and The Origin of Their Asymmetries, ApJ, 846, 149, `1704.05999`

Choudhuri, A. R., 1989, The Evolution of Loop Structures in Flux Rings Within the Solar Convection Zone, Sol. Phys., 123, 217–239

Choudhuri, A. R., Schussler, M., Dikpati, M., 1995, The solar dynamo with meridional circulation., A&A, 303, L29

Christensen-Dalsgaard, J., 2003, Lecture Notes on Stellar Oscillations, 5th edition, lecture notes, University of Aarhus, Available online at `http://users-phys.au.dk/jcd/oscilnotes/` on May 12, 2021

De Rosa, M. L., Schrijver, C. J., 2006, Consequences of large-scale flows around active regions on the dispersal of magnetic field across the solar surface, in Proceedings of SOHO 18/GONG 2006/HELAS I, Beyond the spherical Sun, vol. 624 of ESA Special Publication, p. 12

D'Silva, S., Choudhuri, A. R., 1993, A theoretical model for tilts of bipolar magnetic regions, A&A, 272, 621

Duvall, T. L., J., 1979, Large-scale solar velocity fields., Sol. Phys., 63, 3–15

Duvall, T. L., J., Birch, A. C., 2010, The Vertical Component of the Supergranular Motion, ApJ, 725, L47–L51

Duvall, T. L., J., Jefferies, S. M., Harvey, J. W., Pomerantz, M. A., 1993, Time-distance helioseismology, Nature, 362, 430–432

Eddy, J. A., 1976, The maunder minimum, Science, 192, 1189–1202, ISSN 0036-8075, https://science.sciencemag.org/content/192/4245/1189.full.pdf

Evershed, J., 1909, Radial movement in sun-spots, MNRAS, 69, 454

Fan, Y., 2001, Nonlinear Growth of the Three-dimensional Undular Instability of a Horizontal Magnetic Layer and the Formation of Arching Flux Tubes, ApJ, 546, 509–527

Fan, Y., 2009, Magnetic Fields in the Solar Convection Zone, Living Reviews in Solar Physics, 6, 4

Fan, Y., Fang, F., 2014, A Simulation of Convective Dynamo in the Solar Convective Envelope: Maintenance of the Solar-like Differential Rotation and Emerging Flux, ApJ, 789, 35, 1405.3926

Fan, Y., Fisher, G. H., Deluca, E. E., 1993, The Origin of Morphological Asymmetries in Bipolar Active Regions, ApJ, 405, 390

Fan, Y., Zweibel, E. G., Linton, M. G., Fisher, G. H., 1998, The Rise of Kink-Unstable Magnetic Flux Tubes in the Solar Convection Zone, ApJ, 505, L59–L63

Featherstone, N. A., Miesch, M. S., 2015, Meridional Circulation in Solar and Stellar Convection Zones, ApJ, 804, 67, 1501.06501

Fisher, G. H., Welsch, B. T., 2008, FLCT: A Fast, Efficient Method for Performing Local Correlation Tracking, in Subsurface and Atmospheric Influences on Solar Activity, (Eds.) R. Howe, R. W. Komm, K. S. Balasubramaniam, G. J. D. Petrie, vol. 383 of Astronomical Society of the Pacific Conference Series, p. 373, 0712.4289

Fisher, G. H., Fan, Y., Howard, R. F., 1995, Comparisons between Theory and Observation of Active Region Tilts, ApJ, 438, 463

Fisher, G. H., Fan, Y., Longcope, D. W., Linton, M. G., Pevtsov, A. A., 2000, The Solar Dynamo and Emerging Flux - (Invited Review), Sol. Phys., 192, 119–139

Gary, G. A., Hagyard, M. J., 1990, Transformation of vector magnetograms and the problems associated with the effects of perspective and the azimuthal ambiguity, Sol. Phys., 126, 21–36

Giles, P. M., 2000, Time-distance measurements of large-scale flows in the solar convection zone, Ph.D. thesis, STANFORD UNIVERSITY

Giovanelli, R. G., 1980, The Supergranule Velocity Field, Sol. Phys., 67, 211–228

Gizon, L., Birch, A. C., 2005, Local Helioseismology, Living Reviews in Solar Physics, 2, 6

Gizon, L., Duvall, T. L., J., Larsen, R. M., 2000, Seismic Tomography of the Near Solar Surface, Journal of Astrophysics and Astronomy, 21, 339

Gizon, L., Duvall, Jr., T. L., Larsen, R. M., 2001, Probing Surface Flows and Magnetic Activity with Time-Distance Helioseismology, in Recent Insights into the Physics of the Sun and Heliosphere: Highlights from SOHO and Other Space Missions, (Eds.) P. Brekke, B. Fleck, J. B. Gurman, vol. 203 of IAU Symposium, p. 189

Gizon, L., Birch, A. C., Spruit, H. C., 2010, Local Helioseismology: Three-Dimensional Imaging of the Solar Interior, ARA&A, 48, 289–338, `1001.0930`

Gizon, L., Cameron, R. H., Pourabdian, M., Liang, Z.-C., Fournier, D., Birch, A. C., Hanson, C. S., 2020, Meridional flow in the Sun's convection zone is a single cell in each hemisphere, Science, 368, 1469–1472

Gottschling, N., Schunker, H., Birch, A. C., Löptien, B., Gizon, L., 2021, Evolution of solar surface inflows around emerging active regions, A&A, 652, A148

Haber, D. A., Hindman, B. W., Toomre, J., Bogart, R. S., Hill, F., 2001, Daily variations of large-scale subsurface flows and global synoptic flow maps from dense-pack ring-diagram analyses, in SOHO 10/GONG 2000 Workshop: Helio- and Asteroseismology at the Dawn of the Millennium, (Eds.) A. Wilson, P. L. Pallé, vol. 464 of ESA Special Publication, pp. 209–212

Haber, D. A., Hindman, B. W., Toomre, J., Thompson, M. J., 2004, Organized Subsurface Flows near Active Regions, Sol. Phys., 220, 371–380

Hale, G. E., 1908, On the Probable Existence of a Magnetic Field in Sun-Spots, ApJ, 28, 315

Hale, G. E., Ellerman, F., Nicholson, S. B., Joy, A. H., 1919, The Magnetic Polarity of Sun-Spots, ApJ, 49, 153

Hanasoge, S., Gizon, L., Sreenivasan, K. R., 2016, Seismic Sounding of Convection in the Sun, Annual Review of Fluid Mechanics, 48, 191–217, `1503.07961`

Hart, A. B., 1956, Motions in the Sun at the photospheric level. VI. Large-scale motions in the equatorial region, MNRAS, 116, 38

Harvey, K., Harvey, J., 1973, Observations of Moving Magnetic Features near Sunspots, Sol. Phys., 28, 61–71

Hathaway, D. H., Beck, J. G., Bogart, R. S., Bachmann, K. T., Khatri, G., Petitto, J. M., Han, S., Raymond, J., 2000, The Photospheric Convection Spectrum, Sol. Phys., 193, 299–312

Hathaway, D. H., Beck, J. G., Han, S., Raymond, J., 2002, Radial Flows in Supergranules, Sol. Phys., 205, 25–38

Hathaway, D. H., Teil, T., Norton, A. A., Kitiashvili, I., 2015, The Sun's Photospheric Convection Spectrum, ApJ, 811, 105, `1508.03022`

Herschel, W., 1801, Observations Tending to Investigate the Nature of the Sun, in Order to Find the Causes or Symptoms of Its Variable Emission of Light and Heat; With Remarks on the Use That May Possibly Be Drawn from Solar Observations, Philosophical Transactions of the Royal Society of London Series I, 91, 265–318

Hindman, B. W., Haber, D. A., Toomre, J., 2009, Subsurface Circulations within Active Regions, ApJ, 698, 1749–1760, `0904.1575`

Hirzberger, J., Bonet, J. A., Vázquez, M., Hanslmeier, A., 1999, Time Series of Solar Granulation Images. II. Evolution of Individual Granules, ApJ, 515, 441–454

Hirzberger, J., Gizon, L., Solanki, S. K., Duvall, T. L., 2008, Structure and Evolution of Supergranulation from Local Helioseismology, Sol. Phys., 251, 417–437

Hoeksema, J. T., Liu, Y., Hayashi, K., Sun, X., Schou, J., Couvidat, S., Norton, A., Bobra, M., Centeno, R., Leka, K. D., Barnes, G., Turmon, M., 2014, The Helioseismic and Magnetic Imager (HMI) Vector Magnetic Field Pipeline: Overview and Performance, Sol. Phys., 289, 3483–3530, `1404.1881`

Hotta, H., Iijima, H., 2020, On rising magnetic flux tube and formation of sunspots in a deep domain, MNRAS, 494, 2523–2537, `2003.10583`

Howe, R., 2009, Solar Interior Rotation and its Variation, Living Reviews in Solar Physics, 6, 1, `0902.2406`

Hunter, J. D., 2007, Matplotlib: A 2d graphics environment, Computing in Science & Engineering, 9, 90–95

Iijima, H., Hotta, H., Imada, S., Kusano, K., Shiota, D., 2017, Improvement of solar-cycle prediction: Plateau of solar axial dipole moment, A&A, 607, L2, `1710.06528`

Jackiewicz, J., Gizon, L., Birch, A. C., 2008, High-Resolution Mapping of Flows in the Solar Interior: Fully Consistent OLA Inversion of Helioseismic Travel Times, Sol. Phys., 251, 381–415, `0802.3810`

Jafarzadeh, S., Cameron, R. H., Solanki, S. K., Pietarila, A., Feller, A., Lagg, A., Gandorfer, A., 2014, Migration of Ca II H bright points in the internetwork, A&A, 563, A101, `1401.7522`

Jiang, J., Iṣik, E., Cameron, R. H., Schmitt, D., Schüssler, M., 2010, The Effect of Activity-related Meridional Flow Modulation on the Strength of the Solar Polar Magnetic Field, ApJ, 717, 597–602, `1005.5317`

Jiang, J., Cameron, R. H., Schüssler, M., 2014, Effects of the Scatter in Sunspot Group Tilt Angles on the Large-scale Magnetic Field at the Solar Surface, ApJ, 791, 5, `1406.5564`

Kitchatinov, L. L., 2013, Theory of differential rotation and meridional circulation, in Solar and Astrophysical Dynamos and Magnetic Activity, (Eds.) A. G. Kosovichev, E. de Gouveia Dal Pino, Y. Yan, vol. 294 of IAU Symposium, pp. 399–410, `1210.7041`

Knizhnik, K. J., Leake, J. E., Linton, M. G., Dacie, S., 2021, The Rise and Emergence of Untwisted Toroidal Flux Ropes on the Sun, ApJ, 907, 19, `2101.01020`

Komm, R., Howe, R., Hill, F., 2011, Subsurface Velocity of Emerging and Decaying Active Regions, Sol. Phys., 268, 407–428

Komm, R., Howe, R., Hill, F., 2012, Vorticity of Subsurface Flows of Emerging and Decaying Active Regions, Sol. Phys., 277, 205–226

Komm, R. W., Howard, R. F., Harvey, J. W., 1993, Meridional Flow of Small Photospheric Magnetic Features, Sol. Phys., 147, 207–223

Kosovichev, A. G., Stenflo, J. O., 2008, Tilt of Emerging Bipolar Magnetic Regions on the Sun, ApJ, 688, L115

Labonte, B. J., Howard, R., 1982, Solar Rotation Measurements at Mount-Wilson - Part Three - Meridional Flow and Limbshift, Sol. Phys., 80, 361–372

Langfellner, J., Gizon, L., Birch, A. C., 2015, Spatially resolved vertical vorticity in solar supergranulation using helioseismology and local correlation tracking, A&A, 581, A67, `1504.00223`

Langfellner, J., Birch, A. C., Gizon, L., 2018, Evolution and wave-like properties of the average solar supergranule, A&A, 617, A97, `1805.12522`

Leighton, R. B., 1964, Transport of Magnetic Fields on the Sun., ApJ, 140, 1547

Leighton, R. B., Noyes, R. W., Simon, G. W., 1962, Velocity Fields in the Solar Atmosphere. I. Preliminary Report., ApJ, 135, 474

Leka, K. D., Barnes, G., Birch, A. C., Gonzalez-Hernandez, I., Dunn, T., Javornik, B., Braun, D. C., 2013, Helioseismology of Pre-emerging Active Regions. I. Overview, Data, and Target Selection Criteria, ApJ, 762, 130, `1303.1433`

Leka, K. D., Barnes, G., Wagner, E. L., 2017, Evaluating (and Improving) Estimates of the Solar Radial Magnetic Field Component from Line-of-Sight Magnetograms, Sol. Phys., 292, 36, `1701.04836`

Liang, Z.-C., Gizon, L., Birch, A. C., Duvall, T. L., Rajaguru, S. P., 2018, Solar meridional circulation from twenty-one years of SOHO/MDI and SDO/HMI observations. Helio-seismic travel times and forward modeling in the ray approximation, A&A, 619, A99, 1808.08874

Lindsey, C., Braun, D. C., 2000, Basic Principles of Solar Acoustic Holography - (Invited Review), Sol. Phys., 192, 261–284

Linton, M. G., Longcope, D. W., Fisher, G. H., 1996, The Helical Kink Instability of Isolated, Twisted Magnetic Flux Tubes, ApJ, 469, 954

Lisle, J., Toomre, J., 2004, Cause of Shrinking Sun Effect in Local Correlation Tracking and Impacts on the Mapping of Ssw Flows, in SOHO 14 Helio- and Asteroseismology: Towards a Golden Future, (Ed.) D. Danesy, vol. 559 of ESA Special Publication, p. 556

Liu, Y., Hoeksema, J. T., Scherrer, P. H., Schou, J., Couvidat, S., Bush, R. I., Duvall, T. L., Hayashi, K., Sun, X., Zhao, X., 2012, Comparison of Line-of-Sight Magnetograms Taken by the Solar Dynamics Observatory/Helioseismic and Magnetic Imager and Solar and Heliospheric Observatory/Michelson Doppler Imager, Sol. Phys., 279, 295–316

Liu, Y., Hoeksema, J. T., Sun, X., 2014, Test of the Hemispheric Rule of Magnetic Helicity in the Sun Using the Helioseismic and Magnetic Imager (HMI) Data, ApJ, 783, L1

Löhner-Böttcher, J., Schlichenmaier, R., 2013, Correlations between sunspots and their moat flows, A&A, 551, A105, 1301.2434

Longcope, D. W., Fisher, G. H., Pevtsov, A. A., 1998, Flux-Tube Twist Resulting from Helical Turbulence: The Σ-Effect, ApJ, 507, 417–432

Löptien, B., Birch, A. C., Duvall, T. L., Gizon, L., Schou, J., 2016a, Data compression for local correlation tracking of solar granulation, A&A, 587, A9, 1512.03243

Löptien, B., Birch, A. C., Duvall, T. L., Gizon, L., Schou, J., 2016b, The shrinking Sun: A systematic error in local correlation tracking of solar granulation, A&A, 590, A130, 1604.04469

Löptien, B., Birch, A. C., Duvall, T. L., Gizon, L., Proxauf, B., Schou, J., 2017, Measuring solar active region inflows with local correlation tracking of granulation, A&A, 606, A28, 1705.08833

Löptien, B., Gizon, L., Birch, A. C., Schou, J., Proxauf, B., Duvall, T. L., Bogart, R. S., Christensen, U. R., 2018, Global-scale equatorial Rossby waves as an essential compo-nent of solar internal dynamics, Nature Astronomy, 2, 568–573, 1805.07244

Manek, B., Brummell, N., 2021, On the Origin of Solar Hemispherical Helicity Rules: Simulations of the Rise of Magnetic Flux Concentrations in a Background Field, ApJ, 909, 72, 2101.03472

Martin-Belda, D., Cameron, R. H., 2016, Surface flux transport simulations: Effect of inflows toward active regions and random velocities on the evolution of the Sun's large-scale magnetic field, A&A, 586, A73, 1512.02541

Martin-Belda, D., Cameron, R. H., 2017a, Evolution of the Sun's non-axisymmetric toroidal field, A&A, 603, A53, `1703.10075`

Martin-Belda, D., Cameron, R. H., 2017b, Inflows towards active regions and the modulation of the solar cycle: A parameter study, A&A, 597, A21, `1609.01199`

McKinney, W., 2010, Data Structures for Statistical Computing in Python, in Proceedings of the 9th Python in Science Conference, (Eds.) Stéfan van der Walt, Jarrod Millman, pp. 56 – 61

Meyer, F., Schmidt, H. U., 1968, A Model for the Evershed Flaw in Sunspots, Mitteilungen der Astronomischen Gesellschaft Hamburg, 25, 194

Meyer, F., Schmidt, H. U., Weiss, N. O., Wilson, P. R., 1974, The growth and decay of sunspots., MNRAS, 169, 35–57

Miesch, M. S., 2005, Large-Scale Dynamics of the Convection Zone and Tachocline, Living Reviews in Solar Physics, 2, 1

Miesch, M. S., 2012, The solar dynamo, Philosophical Transactions of the Royal Society of London Series A, 370, 3049–3069

Nelson, N. J., Brown, B. P., Brun, A. S., Miesch, M. S., Toomre, J., 2013, Magnetic Wreaths and Cycles in Convective Dynamos, ApJ, 762, 73, `1211.3129`

Nordlund, Å., Stein, R. F., Asplund, M., 2009, Solar Surface Convection, Living Reviews in Solar Physics, 6, 2

November, L. J., Simon, G. W., 1988, Precise proper-motion measurement of solar granulation, ApJ, 333, 427–442

Oba, T., Iida, Y., Shimizu, T., 2020, Average Radial Structures of Gas Convection in the Solar Granulation, ApJ, 890, 141, `2001.03575`

Oliphant, T. E., 2006, A guide to NumPy, vol. 1, Trelgol Publishing USA

Ossendrijver, M., 2003, The solar dynamo, A&A Rev., 11, 287–367

Parker, E. N., 1955, The Formation of Sunspots from the Solar Toroidal Field., ApJ, 121, 491

Parker, E. N., 1975, The generation of magnetic fields in astrophysical bodies. X. Magnetic buoyancy and the solar dynamo., ApJ, 198, 205–209

Pesnell, W. D., Thompson, B. J., Chamberlin, P. C., 2012, The Solar Dynamics Observatory (SDO), Sol. Phys., 275, 3–15

Petrovay, K., 2020, Solar cycle prediction, Living Reviews in Solar Physics, 17, 2, `1907.02107`

Pevtsov, A. A., Maleev, V. M., Longcope, D. W., 2003, Helicity Evolution in Emerging Active Regions, ApJ, 593, 1217–1225

Pevtsov, A. A., Berger, M. A., Nindos, A., Norton, A. A., van Driel-Gesztelyi, L., 2014, Magnetic Helicity, Tilt, and Twist, Space Sci. Rev., 186, 285–324

Pipin, V. V., 2018, Nonkinematic solar dynamo models with double-cell meridional circulation, Journal of Atmospheric and Solar-Terrestrial Physics, 179, 185–201, `1803.09459`

Rast, M. P., 2003, The Scales of Granulation, Mesogranulation, and Supergranulation, ApJ, 597, 1200–1210

Rempel, M., Cheung, M. C. M., 2014, Numerical Simulations of Active Region Scale Flux Emergence: From Spot Formation to Decay, ApJ, 785, 90, `1402.4703`

Rieutord, M., Rincon, F., 2010, The Sun's Supergranulation, Living Reviews in Solar Physics, 7, 2, `1005.5376`

Rincon, F., 2019, Dynamo theories, Journal of Plasma Physics, 85, 205850401, `1903.07829`

Rincon, F., Rieutord, M., 2018, The Sun's supergranulation, Living Reviews in Solar Physics, 15, 6

Roudier, T., Rieutord, M., Prat, V., Malherbe, J. M., Renon, N., Frank, Z., Švanda, M., Berger, T., Burston, R., Gizon, L., 2013, Comparison of solar horizontal velocity fields from SDO/HMI and Hinode data, A&A, 552, A113, `1303.4271`

Sangeetha, C. R., Tripathi, D., Rajaguru, S. P., 2020, Signatures of Untwisting Magnetic Field in a Small Emerging Bipole in the Solar Photosphere, ApJ, 895, 67, `2004.05615`

Scharmer, G. B., Nordlund, Å., Heinemann, T., 2008, Convection and the Origin of Evershed Flows in Sunspot Penumbrae, ApJ, 677, L149, `0802.1927`

Schmidt, H. U., 1968, Magnetohydrodynamics of an Active Region, pp. 95–107, Springer Netherlands, Dordrecht, ISBN 978-94-011-6815-1

Schou, J., Scherrer, P. H., Bush, R. I., Wachter, R., Couvidat, S., Rabello-Soares, M. C., Bogart, R. S., Hoeksema, J. T., Liu, Y., Duvall, T. L., Akin, D. J., Allard, B. A., Miles, J. W., Rairden, R., Shine, R. A., Tarbell, T. D., Title, A. M., Wolfson, C. J., Elmore, D. F., Norton, A. A., Tomczyk, S., 2012, Design and Ground Calibration of the Helioseismic and Magnetic Imager (HMI) Instrument on the Solar Dynamics Observatory (SDO), Sol. Phys., 275, 229–259

Schrijver, C. J., 2001, Simulations of the Photospheric Magnetic Activity and Outer Atmospheric Radiative Losses of Cool Stars Based on Characteristics of the Solar Magnetic Field, ApJ, 547, 475–490

Schuessler, M., 1979, Magnetic buoyancy revisited: analytical and numerical results for rising flux tubes., A&A, 71, 79–91

Schunker, H., Braun, D. C., Birch, A. C., Burston, R. B., Gizon, L., 2016, SDO/HMI survey of emerging active regions for helioseismology, A&A, 595, A107, `1608.08005`

Schunker, H., Birch, A. C., Cameron, R. H., Braun, D. C., Gizon, L., Burston, R. B., 2019, Average motion of emerging solar active region polarities. I. Two phases of emergence, A&A, 625, A53, `1903.11839`

Schunker, H., Baumgartner, C., Birch, A. C., Cameron, R. H., Braun, D. C., Gizon, L., 2020, Average motion of emerging solar active region polarities. II. Joy's law, A&A, 640, A116, `2006.05565`

Schwabe, H., 1844, Sonnenbeobachtungen im Jahre 1843. Von Herrn Hofrath Schwabe in Dessau, Astronomische Nachrichten, 21, 233

Seehafer, N., 1990, Electric Current Helicity in the Solar Atmosphere, Sol. Phys., 125, 219–232

Sheeley, N. R., J., 1969, The Evolution of the Photospheric Network, Sol. Phys., 9, 347–357

Sheeley, N. R., J., 1972, Observations of the Horizontal Velocity Field Surrounding Sunspots, Sol. Phys., 25, 98–103

Shine, R. A., Title, A. M., Tarbell, T. D., Smith, K., Frank, Z. A., Scharmer, G., 1994, High-Resolution Observations of the Evershed Effect in Sunspots, ApJ, 430, 413

Siu-Tapia, A. L., Rempel, M., Lagg, A., Solanki, S. K., 2018, Evershed and Counter-Evershed Flows in Sunspot MHD Simulations, ApJ, 852, 66, `1712.01202`

Snodgrass, H. B., 1983, Magnetic rotation of the solar photosphere, ApJ, 270, 288–299

Sobotka, M., Roudier, T., 2007, Properties of sunspot moats derived from horizontal motions, A&A, 472, 277–282

Solanki, S. K., 2003, Sunspots: An overview, A&A Rev., 11, 153–286

Spruit, H. C., 1981, Motion of magnetic flux tubes in the solar convection zone and chromosphere., A&A, 98, 155–160

Spruit, H. C., 2003, Origin of the torsional oscillation pattern of solar rotation, Sol. Phys., 213, 1–21, `astro-ph/0209146`

Stix, M., 2002, The Sun, Springer, 2nd edn., corrected second printing 2004

Sturrock, Z., Hood, A. W., 2016, Sunspot rotation. II. Effects of varying the field strength and twist of an emerging flux tube, A&A, 593, A63, `1605.07378`

Sturrock, Z., Hood, A. W., Archontis, V., McNeill, C. M., 2015, Sunspot rotation. I. A consequence of flux emergence, A&A, 582, A76, `1508.02437`

Temmer, M., 2021, Space weather: the solar perspective – an update to Schwenn (2006), arXiv e-prints, arXiv:2104.04261, `2104.04261`

Thompson, W. T., 2006, Coordinate systems for solar image data, A&A, 449, 791–803

Unsöld, A., 1930, Konvektion in der Sonnenatmosphäre (nebst einer Bemerkung zur Deutung der Novae). (Eingegangen am 28. Juni 1930), ZAp, 1, 138

Upton, L. A., Hathaway, D. H., 2018, An Updated Solar Cycle 25 Prediction With AFT: The Modern Minimum, Geophys. Res. Lett., 45, 8091–8095, `1808.04868`

van Driel-Gesztelyi, L., Green, L. M., 2015, Evolution of Active Regions, Living Reviews in Solar Physics, 12, 1

Vaquero, J. M., Vázquez, M., 2009, The Sun Recorded Through History: Scientific Data Extracted from Historical Documents, vol. 361

Vargas Domínguez, S., Rouppe van der Voort, L., Bonet, J. A., Martínez Pillet, V., Van Noort, M., Katsukawa, Y., 2008, Moat Flow in the Vicinity of Sunspots for Various Penumbral Configurations, ApJ, 679, 900–909, `0802.1457`

Verma, M., Steffen, M., Denker, C., 2013, Evaluating local correlation tracking using CO5BOLD simulations of solar granulation, A&A, 555, A136, `1305.6033`

Verma, M., Kummerow, P., Denker, C., 2018, On the extent of the moat flow in axisymmetric sunspots, Astronomische Nachrichten, 339, 268–276, `1805.04356`

Virtanen, P., Gommers, R., Oliphant, T. E., Haberland, M., Reddy, T., Cournapeau, D., Burovski, E., Peterson, P., Weckesser, W., Bright, J., van der Walt, S. J., Brett, M., Wilson, J., Millman, K. J., Mayorov, N., Nelson, A. R. J., Jones, E., Kern, R., Larson, E., Carey, C. J., Polat, İ., Feng, Y., Moore, E. W., VanderPlas, J., Laxalde, D., Perktold, J., Cimrman, R., Henriksen, I., Quintero, E. A., Harris, C. R., Archibald, A. M., Ribeiro, A. H., Pedregosa, F., van Mulbregt, P., SciPy 1.0 Contributors, 2020, SciPy 1.0: Fundamental Algorithms for Scientific Computing in Python, Nature Methods, 17, 261–272

Švanda, M., Zhao, J., Kosovichev, A. G., 2007, Comparison of Large-Scale Flows on the Sun Measured by Time-Distance Helioseismology and Local Correlation Tracking, Sol. Phys., 241, 27–37, `astro-ph/0701717`

Švanda, M., Roudier, T., Rieutord, M., Burston, R., Gizon, L., 2013, Comparison of Solar Surface Flows Inferred from Time-Distance Helioseismology and Coherent Structure Tracking Using HMI/SDO Observations, ApJ, 771, 32, `1305.0875`

Švanda, M., Sobotka, M., Bárta, T., 2014, Moat Flow System around Sunspots in Shallow Subsurface Layers, ApJ, 790, 135, `1406.2482`

Wang, H., Zirin, H., 1989, Study of Supergranules, Sol. Phys., 120, 1–17

Wang, Y. M., Sheeley, N. R., J., Nash, A. G., 1991, A New Solar Cycle Model Including Meridional Circulation, ApJ, 383, 431

Wang, Y. M., Sheeley, N. R., J., Lean, J., 2002, Meridional Flow and the Solar Cycle Variation of the Sun's Open Magnetic Flux, ApJ, 580, 1188–1196

Warnecke, J., Losada, I. R., Brandenburg, A., Kleeorin, N., Rogachevskii, I., 2016, Bipolar region formation in stratified two-layer turbulence, A&A, 589, A125, `1502.03799`

Welsch, B. T., Fisher, G. H., Abbett, W. P., Regnier, S., 2004, ILCT: Recovering Photospheric Velocities from Magnetograms by Combining the Induction Equation with Local Correlation Tracking, ApJ, 610, 1148–1156

Yan, X. L., Qu, Z. Q., Kong, D. F., 2008, Relationship between rotating sunspots and flare productivity, MNRAS, 391, 1887–1892

Yeates, A. R., 2014, Coronal Magnetic Field Evolution from 1996 to 2012: Continuous Non-potential Simulations, Sol. Phys., 289, 631–648, `1304.0609`

Yeates, A. R., 2020, How Good Is the Bipolar Approximation of Active Regions for Surface Flux Transport?, Sol. Phys., 295, 119, `2008.03203`

Zhao, J., Kosovichev, A. G., 2004, Torsional Oscillation, Meridional Flows, and Vorticity Inferred in the Upper Convection Zone of the Sun by Time-Distance Helioseismology, ApJ, 603, 776–784

Zheng, J., Yang, Z., Guo, K., Wang, H., Wang, S., 2016, On the Rotation of Sunspots and Their Magnetic Polarity, ApJ, 826, 6, `1607.08343`

A   Magnetic flux as a function of central meridian distance in SDO data

The radial component B_z of the vector magnetic field is known to have limitations with respect to large-scale variations. Specifically, the noise is a function of distance from disk center. Analysis of the total unsigned flux $|\Phi|$ calculated from B_z shows an increase of $|\Phi|$ from disk center away towards about 60° (Hoeksema et al. 2014). This makes the usage of B_z difficult in cases where a systematic variation of the magnetic field strength with disk position complicates further analysis, for example when measuring the total flux of the AR over time as compared to the simulated regions, as in Chapter 3. In such cases, instead of B_z, the line-of-sight magnetic field maps B_{los} are used, where the noise is less severe (Liu et al. 2012). However, in B_{los}, the measured magnetic field strength of a feature on the solar disk depends intrinsically on its position, due to projection. This can be approximately corrected for by dividing each map element of a magnetogram by $\mu = \cos(\theta)$, where θ is the angular distance to the center of the disk. This assumes that the field is radial. The calculation of θ is done as

$$\mu = \arccos\left(\sin(\vartheta_1)\sin(\vartheta_2) + \cos(\vartheta_1)\cos(\vartheta_2)\cos(|\varphi_1 - \varphi_2|)\right), \qquad (A.1)$$

where φ_1, ϑ_1 are the Carrington longitude and latitude of the map element and φ_2, ϑ_2 are the Carrington longitude and latitude of the disk center. This takes the B angle into account.

Fig. A.1 shows averages of the unsigned flux in a disk of 5° around the center of the control region patches as a function of central meridian distance (CMD). The black, blue, and orange lines show the different cases of the radial magnetic field component B_z (left), the line-of-sight magnetic field component B_{los} (center), and the μ-angle corrected B_{los}, respectively. In the B_z case, the mean value increases drastically towards the limb, as discussed above. In the B_{los} case, it decreases towards the limb, as expected if the field is mainly radial. This is slightly overcorrected for in the case of the μ-angle corrected B_{los}. While the curve is not perfectly flat, it shows less steep gradients towards disk center, and a much reduced amplitude in the variation as compared to the B_z case. Part of the variation in all three cases can also be attributed to variations in the observed field, as the drop at 40° shows.

Another approximation to the radial field component can be done by computing a potential field that retrieves the observed B_{los}, from which the radial component can be calculated. Leka et al. (2017) find that the commonly used μ-correction of B_{los} manages to recover the true field if the inclination of the field as well as the viewing angle do not
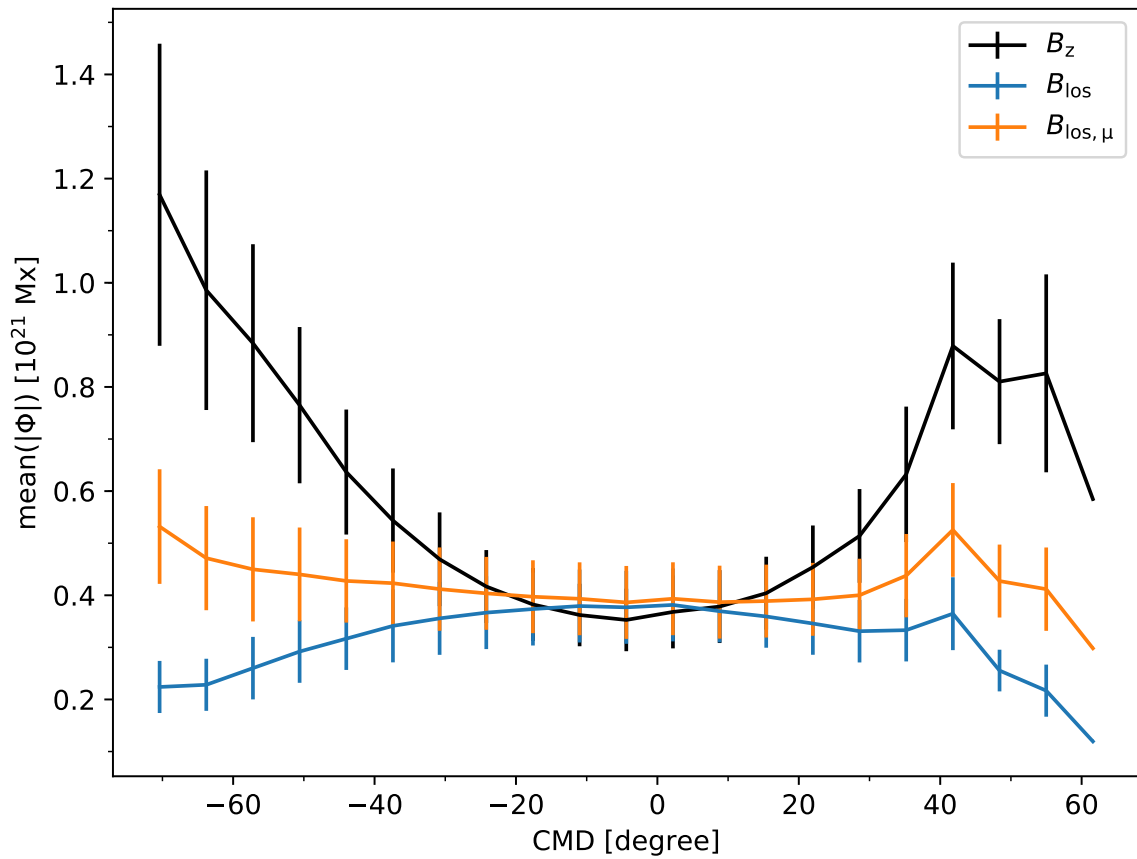
Figure A.1: Mean of the unsigned flux in a disk of 5° around the center of the control region patches, as a function of central meridian distance (CMD). The plot shows the radial component of the vector magnetic field B_z (black line), the line-of-sight magnetic field B_{los} (blue line), and the μ-corrected line-of-sight magnetic field $B_{los,\mu}$ (orange line).

deviate more than a few tens of degrees from the radial direction and the line of sight, respectively. This is the case in the analysis in Sects. 3 and 4.1, where B_z is not used directly. The ARs considered there are relatively close to disk center and have not formed sunspots with systematically horizontal field. This warrants the use of the μ-angle corrected B_{los} data in Sects. 3 and 4.1.

Scientific contributions

Refereed publications

- **N. Gottschling**, H. Schunker, A.C. Birch, B. Löptien, and L. Gizon: *Evolution of solar surface inflows around emerging active regions*, Astronomy & Astrophysics, 652, A148 (2021)

- **N. Gottschling**, H. Schunker, A.C. Birch, R. Cameron, and L. Gizon: *Testing solar surface flux transport models in the first days after active region emergence*, Astronomy & Astrophysics, 660, A6 (2022)

Conference contributions

- 2nd Max Planck Partner Group Workshop on Solar Physics, Mumbai, India, 17-21 March 2019
  Talk: *Active region flows*

- 234th Meeting of the American Astronomical Society, St. Louis, USA, 9-13 June 2019
  Talk: *Evolution of Flows around Emerging Active Regions*

Acknowledgements